UNIVERSITY OF
LEICESTER

Effect of Indenter Size on Damage of Carbon Fibre-Reinforced Polymer Composites under Impact Loads

By

Mazin Yaseen Alisawi

Department of Engineering, University of Leicester, UK

Submitted for the degree of

Doctor of philosophy

July 2017

I would dedicate this work to my brother Hamid.

Abstract

Effect of indenter size on damage of Carbone Fibre-Reinforced Polymer composites under impact loads

By

Mazin Yaseen Alisawi

The applications of composite materials have been increasing significantly in recent decades. The major effect limiting the use composite materials is the lack of understanding of their response and their structural integrity under dynamic loads. Delamination under dynamic load is particularly recognised as the most critical damage process in laminated composites. The objective of this thesis is to experimentally and numerically investigate the fundamental phenomena associated with delamination. This is important develop a further knowledge of the response and damage mechanisms of composite materials under low-velocity impact and static load.

Various parameters that affect the delamination of composite material have been studied in this work, including the diameter of the hemi-spherical indenter and the type of load at the same energy level. The difference between the shape and size of delamination area between different plies has been examined using x-ray commutated tomography.

Cohesive elements have been used in the ABAQUS finite element modelling to determine failure criteria that correspond with the experimental work. It is found that the main delamination area occurs on the tension side of laminates subjected to bending, and that it also depends on the difference in angle between adjacent plies.

The effect of the indenter radius to thickness of plate ratio on the relation between force and damage evolution have been studied numerically for different thickness of plate. This analytical study was repeated for both isotropic and anisotropic materials to show the effect of material type on the previous relation. It is found that the initiation of the delamination can be assessed from the existence of a delamination threshold load in a force-displacement curve under quasi-static load or in a displacement-time curve under dynamic load.

Acknowledgment

I would like to express my sincere gratitude to my supervisors Dr. Simon Gill and Dr. Hugo William for their dedicated guidance and support throughout the project. It would have been impossible to bring the project to a success without their professional help, encouragement and practice.

Also, I would like to thank the ministry of higher education of Iraq for supporting me financially to finish this work.

I also would like to thank the technical support team at the department of Engineering at Leicester University. In particular to Mr. Graham Clark, Mr. Paul Williams, Mr. Vinay Patel, Mr. Keith Stanley, and Mr. Raj for their excellent technical support.

Many Thanks also to all my friends in the fourth floor in Engineering tower for sharing many problems and happiness with me.

I would like to thank my wife, without her it would have been difficult to finish this work

Finally, I would like to thank my parents, my brothers and my sisters, and all my friends.

Symbols

τ_{12}	In-plane shearing stress
τ_{13}	Out of plane shearing stress in X-Z plane
τ_{23}	Out of plane shearing stress in Y-Z plane
a	Contact radius
B_{ij}, D_{ij}	Matrices constants
d	Damage variable for stiffness reduction
d_i	Damage variable for each failure mode i
E_0	Young modulus in 0 angle direction
ε_0	Reference plane strain
E_{11}	In-plane longitudinal Young's modulus
E_{22}	In-plane transverse Young's modulus
E_{33}	Out of plane Young's modulus
E_{90}	Young modulus in 90 angle direction
E_f	Young modulus of fibres
e_f, e_m, e_c, e_d	Damage variables of fibre, matrix in tension and compression respectively
E_m	Young modulus of matrix
F	Applied load
F_i, F_{ij}	Material strength parameters
G_{12}	In-plane shearing modulus
G_1-G_7	Fracture energy for each failure mode
G_{23}	Shearing modulus in 2-3 plane
G_{31}	Shearing modulus in 1-3 plane
G_c	Fracture toughness
G_s	Work done by shear component
G_T	Work done by interfacial traction
G_{xc}	Longitudinal compression fracture energy

G_{xt}	Longitudinal tensile fracture energy
G_{yc}	Transverse compression fracture energy
G_{yt}	Transverse tensile fracture energy
h	Lamina thickness
K	Contact stiffness
K_s	Curvature in transvers direction
k_x	Curvature in x direction
K_y	Curvature in y direction
l_{cz}	Cohesive element length
l_e	Mesh size
m	Projectile mass
P_0	Maximum contact pressure
P_c	The load at elastic limit
Q	Stiffness of Laminate
r	Radius of fibre
R	Indenter radius
S_0	Slope of load-displacement curve
s_{11}	In-plane longitude stress
S_{12}	Shear failure strength in 1-2 plane
s_{22}	In-plane transverse stress
S_{23}	Shear failure strength in 2-3 plane
S_{31}	Shear failure strength in 1-3 plane
s_{33}	Out of plane normal stress
V_f	Fibre volume fraction
V_i	Impact velocity of a projectile
V_m	Matrix volume fraction
V_r	Residual velocity
X_c	In-plane longitudinal compression strength

X_t	In-plane longitude tensile strength
Y_c	In-plane transverse compressive strength
Y_t	In-plane transverse tensile strength
Z_c	Out of plane compressive strength
Z_k	Distance from neutral axis to ply (k)
Z_t	Out of plane tensile strength
α	Constant
δ	Relative displacement
δ_f	Separation at decohesion stage
δ_0	Separation at Elastic limit
ε_{11}	In-plane longitudinal strain
ε_{12}	In-plane shearing strain
ε_{22}	In-plane transverse strain
ε_{33}	Out of plane strain
η	Material mode-mixity exponent
ν_{12}	Poison's ratio in 1-2 plane
ν_{13}	poison ratio in $1x10^3$ plane
ν_{23}	Poison's ratio in 2-3 plane
σ_{11}	Normal stress in x plane
σ_{12}	Shear stress in x-y plane
σ_{13}	Shear stress in x-z plane
σ_{22}	Normal stress in y plane
σ_{23}	Shear stress in y-z plane
σ_{33}	Normal stress in z plane
σ_{I}	Cohesive strength in mode I
σ_{II0}	Cohesive strength in mode II
σ_{III0}	Cohesive strength in mode III

Table of contents

Table of figures

Table of tables

Table of abbreviations

B-K	Benzeggagh and Kenane
BVID	Barely visible impact damage
CDM	Continuum damage mechanics
CFRP	Carbon fibre reinforced polymer
C-T	Computed Tomography
CZMS	Cohesive zone model
DCB	Double cantilever beam
DTL	Damage threshold load
ENF	End notched flexure
FEM	Finite element method
LVI	Low-velocity impact
MADM	Macro-damage mechanics
MIDM	Micro-damage mechanics
QSI	Quasi-static impact
QUADS	Quadratic nominal stress
UD	Unidirectional laminate
UMAT	User-defined material routine
VCCT	Virtual crack closure technique

Chapter 1 Introduction

This chapter includes five sections. In the first section, a brief introduction of the applications and the relevance of this project to industry is given. In the second section, the novel aspect and main application of this aspect is presented. In the following chapter, the aims and the objectives of this thesis are defined. The fourth section showed the methodology that used in this study. Finally, the outline of this work is discussed in the third section.

1.1 Background

Composite materials have been used extensively in many high-performance structural applications such as aeronautical, automotive and marine industries since 1970 [1]. This is due to their better specific strength and stiffness, excellent fatigue strength, good corrosion resistance, and low thermal conductivity. Advanced research in characterising and modelling the mechanical behaviour of composite materials and developing tools and methodologies for predicting their damage tolerance in various applications have been conducted [2]. In most recent aircraft, such as Airbus A350 and the Boeing B787, the composite content has exceeded more than 50 percent of the structural weight [3]. However, the potential weight saving and all the good properties offered by the advanced material is still restricted by current conservative design philosophy. This conservative approach is mainly associated with underestimated allowable design strength due to the concern about the effect of low-velocity impact (LVI) damage on the performance of composite materials. Out-of-plane impact by foreign objects, such as runway debris and dropped tools, is expected to occur during the operation, manufacturing, maintenance, and service of composite structures. The serious effect of this type of damage comes from the fact that it leaves damage that is hardly detectable by visual inspection; this type of damage is called barely visible impact damage (BVID). This type of damage has generally reduced the performance of the composite structures [4].

Due to the inherent brittleness of both entities of the composite laminate, which are the fibre and the epoxy resin, composite laminates structures are more susceptible to impact damage compared with conventional metallic structures. Composite materials fail under a complicated damage mechanism resulting from the interaction between different types of damage modes including matrix cracking, delamination, and fibre breakage. Among all the types of damage, delamination is the dominant failure mode and may cause severe degradation of the structural strength when the structure is under a compressive load. Generally, delamination initiates when two adjacent plies debond. This occurs when the propagation tip of the matrix crack reaches the brittle interface which causes a stress concertation in this region.

Extensive research has been made to understand the mechanism of delamination and the effect of delamination on the performance of composite laminates [5-7]. It has been reported that there is a damage threshold load (DTL) for composite laminates [5, 8, 9]. After the DTL, the area of delamination will increase significantly and thus cause a large reduction in the strength of the composite near the delaminated area. This is clear from the force-displacement curve because the slope changes as the structure becomes more compliant. This force, where the slope changes, is called the knee point load. However, because of the complexity of the failure mechanisms found within composite laminates, a reliable assessment of damage resistance and damage tolerance of composite laminates remains a challenge to the aerospace industry. For this reason, further research is needed to understand the effect of DTL on composite behaviour under quasi-static load and low-velocity impact to improve the design philosophy of composite laminates.

The initiation and propagation of delamination due to quasi-static and low-velocity loads will be studied through the investigation of the contact behaviour of composite laminates. This work will also investigate the difference between quasi-static and low-velocity impact at the same energy level, and its effect on the size and shape of the delamination area between adjacent plies with different orientations i.e. (0/45, 45/90, 90/-45, and -45/-45). The stress field in the vicinity of the contact point is expected to depend on the size of the spherical impactor radius proportional to the thickness of the laminate. Therefore, another important aspect of this work is to investigate the effect of impactor size when it is comparable to the laminate thickness.

This project also focuses on using the Finite Element Method (FEM), through the commercial ABAQUS software package, to model the area of delamination between all adjacent plies. These predictions are compared with the experimental observations which are obtained using micro-computed tomography micro-CT scanning and reconstructed in three-dimensions using VG Studio software.

1.2 Novel aspect and its applications

The novel aspect of this thesis is to study the effect of impactor radius on the damage of composite laminate under static and dynamic loads the size of the indenter is comparable to the thickness of the composite laminates. Due to wide use of composite material, many types of damages may occur in composite structures. When the size of the indenter is comparable to the plate thickness, damage can be expected during manufacturing, service, and maintenance operations. An example of in-service impact occurs during aircraft take offs and landing, when small stones and small debris from the runway are propelled at low velocities by the tires. During the manufacturing or maintenance processes, tools can be dropped on the structure. This can be classified depending on the mass and the velocity of the dropped mass or the velocity of the stones. This work focuses on the case of low velocity impacts [10].

1.3 Aims and objectives

This project has three main aims, which are to determine:

1. The original contribution of this work is the effect of the impactor tip radius on a laminate failure when it is in the range of the laminate thickness.
2. The macroscopic force and displacement response of composite laminates taken to failure under quasi-static impact (QSI) and low-velocity impact (LVI).

3. The detailed microscopic damage mechanisms that occur under quasi-static and low-velocity loads, and the shape and size of the delamination regions when loaded up to the same energy level.

To achieve the above aims, the work has been done through experimental and numerical studies to investigate the contact behaviour of composite laminates under LVI and QSI with the following objectives:

1. To conduct experiments to characterise the force and deflection history curves for composite laminates taken to failure.
2. To undertake microstructural examination of the materials for damage identification using techniques such as micro-computed tomography (micro-CT)
3. To simulate the contact force history and the initiation of delamination of composite laminates under quasi-static loads using FEM software.
4. To simulate the relation between the contact force and the deflection of the contact point and the initiation of delamination of composite laminates under low-velocity loads.

1.4 Methodology

This study is carried out experimentally and theoretically. This allows the researcher to validate simulation with experimental work to give reliable results. In terms of the simulation part, ABAQUS 14 software has been used to simulate all the details of this work. This includes the composite plate, indenters, and the support, which includes different types of materials and mesh. This leads to different types of damage behaviour. A Hounsfield 10kN universal test machine was used to conduct the experimental work under quasi static load. In the low speed loading case, a drop test rig in the same lab was used to conduct the dynamic load testing. Microstructural examination of the tested materials is carried out using optical microscopy and X-ray Micro-CT techniques. The lay-up orientation and the thickness of the specimens are observed by microscopy, whereas the Micro-CT provides the internal damage picture of the specimens.

Damage between plies or delamination during both types of loading is formulated by using cohesive-zone model rather the traditional continuum damage mechanics (CDM) approach.

1.5 Thesis structure

This thesis presents the research work carried out between January 2013 and July 2017 for the project titled "Impact of Carbon Fibre Reinforced Polymers". The thesis consists of eight main chapters: Introduction; Elastic laminate theory; Contact mechanics; Modelling of failure in plies and laminates; Experimental method; Quasi-static results; Low-velocity impact results; and Conclusions and future work. This chapter has given a short introduction of the background and relevance of the project and explained the project aims and objectives. The basic equations that control the behaviour of the laminates are introduced in the second chapter on elastic laminate theory. In the third chapter, a definition of the static contact on a half space and the effect of contact on samples of finite thickness of isotropic and composite materials is introduced. This also presents a validation of the contact modelling part with experimental results for the composite finite thickness plate. Chapter Four gives the constitutive laws that describe the evolution of damage in composite materials under contact load, presenting a range of damage modes for fibre, matrix, and interfacial failure. The fifth chapter provides details about the experimental work for the quasi-static and low-velocity impact tests. This chapter also explains the preparation of the specimens. Chapter six summarises all the results of the static testing, for both experiment and simulation, and provides a summary of observations between similarities and discrepancies to access the validity of the numerical model. Chapter Seven gives a similar overview of the dynamic tests and simulations. Chapter Eight then draws together the collection of QSI and LVI results and discusses relations between the results. The final chapter gives the key results achieved in the project and the areas where further work is required.

Chapter 2 Elastic laminate theory

2.1 Introduction

Materials are the basic element upon which the performance of any structure depends. Their properties can lead to dramatic improvements in modern life, especially in the field of industrial and technological advancements. This requires materials with specific properties, such as high strength low-weight materials optimised to carry loads in a specific direction. A new generation of composite materials has been created to fulfill this industry requirement.

Materials can be classified into two categories: isotropic and anisotropic materials. Isotropic materials have the same properties in all directions, while in anisotropic materials the properties vary in different directions at any point within the material e.g. $E_{0}° \neq E_{90}° \neq E_{45}°$ (where E is the Young modulus of the material and the subscript is an angle indicating the orientation of the major axis of the anisotropy). When material properties are the same with respect to a plane, this plane is called a material symmetry plane. Isotropic materials have an infinite number of symmetry planes. Orthotropic materials are a special case of anisotropic materials that have three planes of symmetry and this thesis will focus on this type of materials [11].

The basic definition of composite materials is a combination of two or more materials to form another one with better properties than the individual components. In recent years, use of composite materials is increasing dramatically because they have unique properties compared with monolithic materials. These properties include high strength and stiffness, long fatigue life and low density. Composites can also work in severe conditions as they can have good corrosion and wear resistance. Moreover, they are environmentally stable and are good thermal and acoustic insulators. Although the cost of raw composite materials is generally high, metals can be more expensive than composites if they require complex processes of tooling, machining, and assembly [12].

2.2 Types of composite materials

Composites consist of two parts: reinforcement and matrix. In most cases, reinforcements are stiffer and harder than the matrix and carry most of the applied load, while the matrix fixes the fibres in a proper orientation, protects them from environmental circumstances and transfers load between reinforcements. Depending on the matrix, composites can be classified into three types; organic-matrix composites, which include polymers and carbon; metal-matrix composites; and ceramic-matrix composites. The second level of classification depends on the reinforcement shape, either particle reinforcements, whisker reinforcements, continuous fibre laminated composites and woven composites, as illustrated in Figure 2.1. Reinforcements are commonly formed in two shapes: fibres and particles. Fibres have small diameters and high aspect ratios (length to diameter ratio). Very small diameters (≤ 10μm) are preferred as they provide more strength than larger diameter fibres because the probability of crack presence is reduced. In this thesis, the laminate formed from unidirectional continuous fibre composite will be considered.

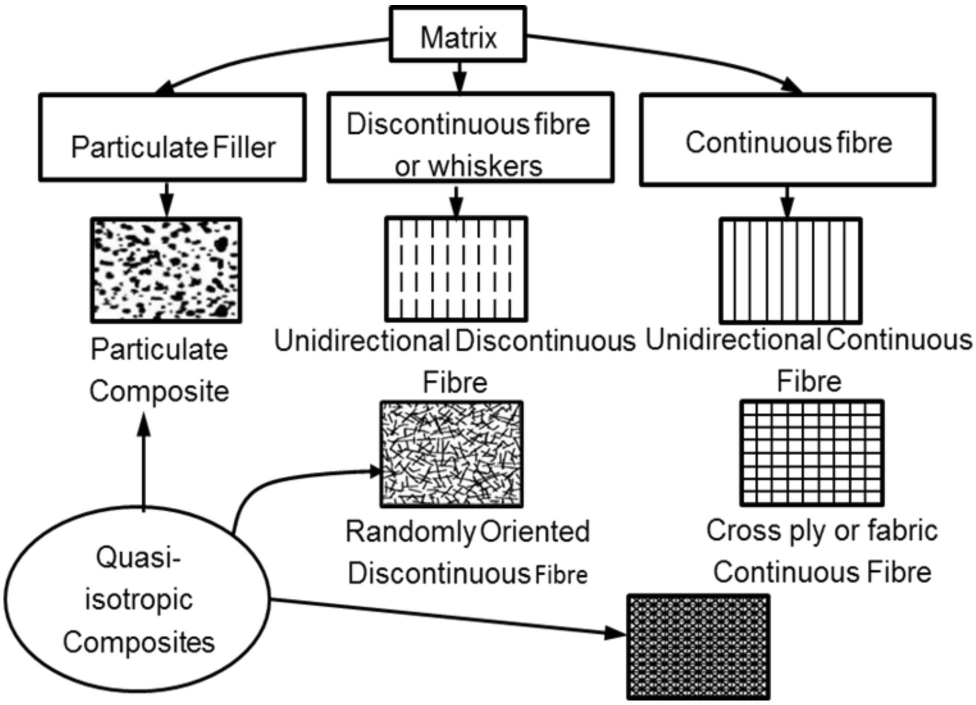

Figure 2.1: Types of composite material [2].

In practice, laminates are designed to be symmetric. A symmetric laminate is a laminate which has two similar layers at the same distance from the reference plane (above and below) as shown in Figure 2.2.

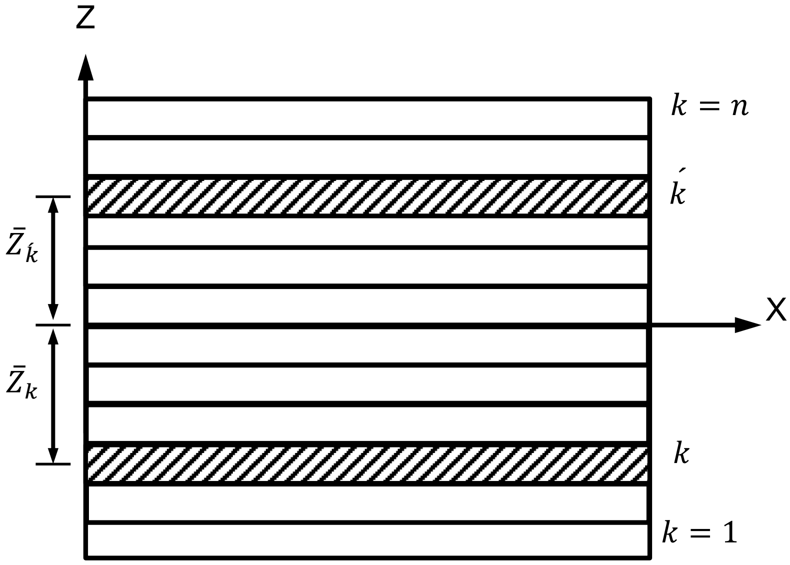

Figure 2.2: Symmetric laminate with identical layers [13].

Most laminates are symmetric as this means that there is no coupling between extensions and bending. A laminate is also commonly balanced. This means that the laminate pairs uplayers with equal but opposite orientations, i.e. angles of $+\theta\ and - \theta$ in a pair.

2.3 Elastic theory of composite materials

The final properties of a composite are highly dependent on the quality and quantity of the fibres [14].The quantity of fibres is commonly defined in terms of the fibre volume fraction,V_f, which is the ratio of the volume of fibres to the volume of the composite. The overall properties of the composite can be found in different methods such as mechanics of materials, numerical, self-consistent field, and bounding, semi-empirical and experimental way [13].

2.4 Elasticity of continuous fibre plies

The general stress state in an elastically deformed body in three-dimensional coordinates can be represented by nine stress components σ_{ij} (where i, j =1,2,3) acting on all sides of cube that are parallel to the 1, 2 and 3 axes coordinate system but only six are unique as the matrix is symmetric, i.e. $\sigma_{23} = \sigma_{32}$ etc., as shown in Figure 2.3.

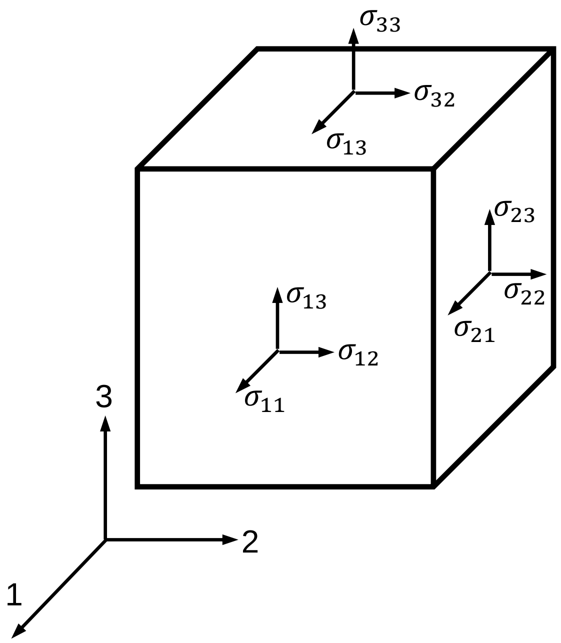

Figure 2.3: State of stress at a point in three dimensions [3].

2.4.1 In-plane loading

For a thin unidirectional lamina or ply, the loading condition is assumed to be plane stress. Thus the relationship between stress and strain for a symmetry, thin plate as shown in Appendix A, becomes

$$\begin{bmatrix}\varepsilon_1\\ \varepsilon_2\\ \gamma_6\end{bmatrix} = \begin{bmatrix}\frac{1}{E_1} & -\frac{\upsilon_{21}}{E_2} & 0\\ -\frac{\upsilon_{12}}{E_1} & \frac{1}{E_2} & 0\\ 0 & 0 & \frac{1}{G_{12}}\end{bmatrix}\begin{bmatrix}\sigma_1\\ \sigma_2\\ \tau_6\end{bmatrix} \tag{2.1}$$

or when reversed

$$\begin{bmatrix} \sigma_1 \\ \sigma_2 \\ \tau_6 \end{bmatrix} = \begin{bmatrix} Q_{11} & Q_{12} & 0 \\ Q_{21} & Q_{22} & 0 \\ 0 & 0 & Q_{66} \end{bmatrix} \begin{bmatrix} \varepsilon_1 \\ \varepsilon_2 \\ \gamma_6 \end{bmatrix} \tag{2.2}$$

where the Q_{ij} are the reduced stiffness matrix coefficients, given in equation (A.6) in Appendix A.

If the applied load plane (x, y) is not coincident with the material reference axes (1, 2), as shown in Figure 2.4, we have to transform the stress and strain components from the load direction to the reference direction using a transfer matrix $[T]$ such that

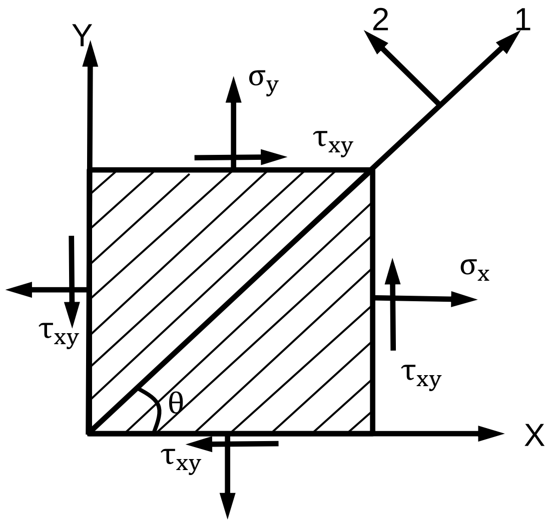

Figure 2.4: Stress component in unidirectional ply [12].

$$\begin{bmatrix} \sigma_x \\ \sigma_y \\ \tau_{xy} \end{bmatrix} = [T^{-1}] \begin{bmatrix} \sigma_1 \\ \sigma_2 \\ \tau_6 \end{bmatrix} = [T^{-1}] \begin{bmatrix} Q_{11} & Q_{12} & 0 \\ Q_{21} & Q_{22} & 0 \\ 0 & 0 & Q_{66} \end{bmatrix} \begin{bmatrix} \epsilon_1 \\ \epsilon_2 \\ \gamma_6 \end{bmatrix} \tag{2.3}$$

and

$$\begin{bmatrix} \epsilon_1 \\ \epsilon_2 \\ \frac{1}{2}\gamma_6 \end{bmatrix} = [T] \begin{bmatrix} \varepsilon_x \\ \varepsilon_y \\ \frac{1}{2}\gamma_{xy} \end{bmatrix} \tag{2.4}$$

where

$$[\mathrm{T}(\theta)] = \begin{bmatrix} \mathrm{m}^2 & \mathrm{n}^2 & 2\mathrm{mn} \\ \mathrm{n}^2 & \mathrm{m}^2 & -2\mathrm{mn} \\ -\mathrm{mn} & \mathrm{mn} & \mathrm{m}^2-\mathrm{n}^2 \end{bmatrix} \tag{2.5}$$

and $\mathrm{m} = \cos\theta$ and $\mathrm{n} = \sin\theta$.

$$[\mathrm{T}]^{-1} = [T(-\theta)] = \begin{bmatrix} \mathrm{m}^2 & \mathrm{n}^2 & -2\mathrm{mn} \\ \mathrm{n}^2 & \mathrm{m}^2 & 2\mathrm{mn} \\ \mathrm{mn} & -\mathrm{mn} & \mathrm{m}^2-\mathrm{n}^2 \end{bmatrix} \tag{2.6}$$

When a lamina is loaded in any direction, the relationship between stress and strain in global coordinates (x,y) will be:

$$\begin{bmatrix} \sigma_x \\ \sigma_y \\ \tau_{xy} \end{bmatrix} = \begin{bmatrix} Q_{xx} & Q_{xy} & Q_{xs} \\ Q_{yx} & Q_{yy} & Q_{ys} \\ Q_{sx} & Q_{sy} & Q_{ss} \end{bmatrix} \begin{bmatrix} \varepsilon_x \\ \varepsilon_y \\ \gamma_{xy} \end{bmatrix} \tag{2.7}$$

where

$$\begin{bmatrix} Q_{xx} & Q_{xy} & Q_{xs} \\ Q_{yx} & Q_{yy} & Q_{ys} \\ Q_{sx} & Q_{sy} & Q_{ss} \end{bmatrix} = [\mathrm{T}^{-1}] \begin{bmatrix} Q_{11} & Q_{12} & 0 \\ Q_{21} & Q_{22} & 0 \\ 0 & 0 & 2Q_{66} \end{bmatrix} [T] \tag{2.8}$$

2.4.2 Bending due to out-of- plane loading

Consider a single layer K in a multidirectional laminate whose mid-plane is at a distance z_k from the laminate reference plane lying in the in the x-y plane, as shown in Figure 2.5. We assume that the thickness of the laminate does not change during loading. In reality, the thickness will change but it is small and negligible. This assumption allows us to assume that the strain in the z-direction is zero [13]. The strain state can then be written as the sum of contributions from in-plane loading and out-of-plane (bending) such that

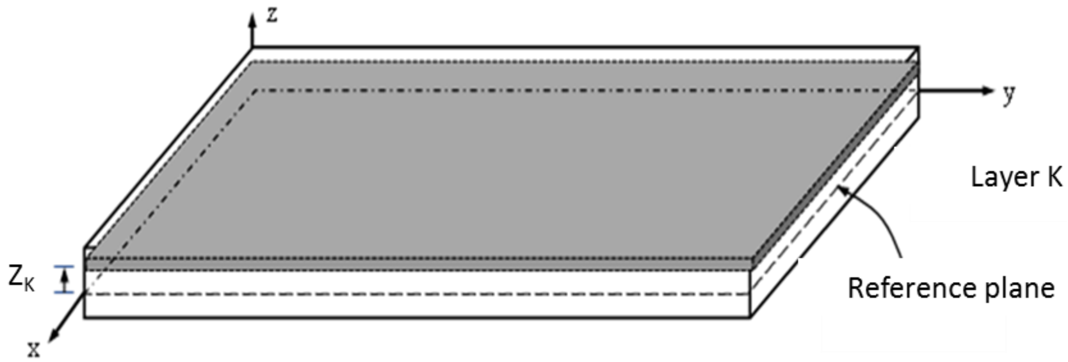

Figure 2.5: A layer K within a laminate [13].

$$\begin{bmatrix} \epsilon_x \\ \epsilon_y \\ \gamma_s \end{bmatrix} = \begin{bmatrix} \epsilon_x^0 \\ \epsilon_y^0 \\ \gamma_s^0 \end{bmatrix} + z \begin{bmatrix} k_x \\ k_y \\ k_s \end{bmatrix} \tag{2.9}$$

where $\epsilon_x^0, \epsilon_y^0$ and γ_s^0 are the reference plane strains in x and y directions and the shear strain of the reference plane or mid-span plane due to in-plane loading respectively, and k_x, k_y and k_s are the curvatures of the laminate, and z is the distance from the neutral axis (centre of the laminate if it is balanced and symmetric).

The stress state in the load coordinate system in the k^{th} ply is given by (2.7**)** such that

$$\begin{bmatrix} \sigma_x \\ \sigma_y \\ \tau_s \end{bmatrix}_k = \begin{bmatrix} Q_{xx} & Q_{xy} & Q_{xs} \\ Q_{yx} & Q_{yy} & Q_{ys} \\ Q_{sx} & Q_{sy} & Q_{ss} \end{bmatrix}_k \begin{bmatrix} \epsilon_x \\ \epsilon_y \\ \gamma_s \end{bmatrix}_k \tag{2.10}$$

From equations (2.9**)** and (2.10) we have:

$$\begin{bmatrix} \sigma_x \\ \sigma_y \\ \tau_s \end{bmatrix}_k = \begin{bmatrix} Q_{xx} & Q_{xy} & Q_{xs} \\ Q_{yx} & Q_{yy} & Q_{ys} \\ Q_{sx} & Q_{sy} & Q_{ss} \end{bmatrix}_k \begin{bmatrix} \epsilon_x^0 \\ \epsilon_y^0 \\ \gamma_s^0 \end{bmatrix}_k + z \begin{bmatrix} Q_{xx} & Q_{xy} & Q_{xs} \\ Q_{yx} & Q_{yy} & Q_{ys} \\ Q_{sx} & Q_{sy} & Q_{ss} \end{bmatrix}_k \begin{bmatrix} k_x \\ k_y \\ k_s \end{bmatrix} \tag{2.11}$$

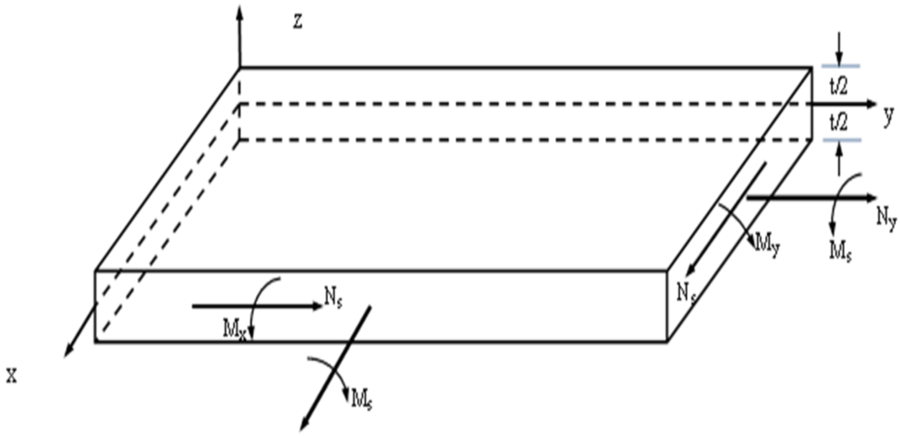

Figure 2.6: Loads and couples applied to the reference plane of the layer [13].

2.4.3 Elasticity of Laminates

In composite materials, the distribution of stresses within a laminate varies from layer to layer discontinuously. For this reason, we need to know the relation between the applied forces and moments and the laminate deformations. In the case of the multilayer laminate, the total force and moment resultants are determined by summing the effect of all layers. Thus, for an n-ply laminate, as shown in Figure 2.6, the forces and moments are given by

$$\begin{bmatrix} N_x \\ N_y \\ N_s \end{bmatrix} = \sum_{k=1}^{n} \left[\begin{bmatrix} Q_{xx} & Q_{xy} & Q_{xs} \\ Q_{yx} & Q_{yy} & Q_{ys} \\ Q_{sx} & Q_{sy} & Q_{ss} \end{bmatrix}_k \begin{bmatrix} \epsilon_x^0 \\ \epsilon_y^0 \\ \gamma_{xy}^0 \end{bmatrix}_k \int_{z_{k-1}}^{z_k} dz + \right. \tag{2.12}$$

$$\left. \begin{bmatrix} Q_{xx} & Q_{xy} & Q_{xs} \\ Q_{yx} & Q_{yy} & Q_{ys} \\ Q_{sx} & Q_{sy} & Q_{ss} \end{bmatrix}_k \begin{bmatrix} k_x \\ k_y \\ k_{xy} \end{bmatrix} \right] \int_{z_{k-1}}^{z_k} zdz$$

and

$$\begin{bmatrix} M_x \\ M_y \\ M_s \end{bmatrix} = \sum_{k=1}^{n} \left[\begin{bmatrix} Q_{xx} & Q_{xy} & Q_{xs} \\ Q_{yx} & Q_{yy} & Q_{ys} \\ Q_{sx} & Q_{sy} & Q_{ss} \end{bmatrix}_k \begin{bmatrix} \epsilon_x^0 \\ \epsilon_y^0 \\ \gamma_{xy}^0 \end{bmatrix}_k \int_{z_{k-1}}^{z_k} zdz \right. \tag{2.13}$$

$$+\begin{bmatrix} Q_{xx} & Q_{xy} & Q_{xs} \\ Q_{yx} & Q_{yy} & Q_{ys} \\ Q_{sx} & Q_{sy} & Q_{ss} \end{bmatrix}_k \begin{bmatrix} k_x \\ k_y \\ k_{xy} \end{bmatrix} \Bigg] \int_{z_{k-1}}^{z_k} z^2 dz$$

or

$$\begin{bmatrix} N_x \\ N_y \\ N_s \end{bmatrix} = \begin{bmatrix} A_{xx} & A_{xy} & A_{xs} \\ A_{yx} & A_{yy} & A_{ys} \\ A_{sx} & A_{sy} & A_{ss} \end{bmatrix} \begin{bmatrix} \epsilon_x^0 \\ \epsilon_y^0 \\ \gamma_{xy}^0 \end{bmatrix} + \begin{bmatrix} B_{xx} & B_{xy} & B_{xs} \\ B_{yx} & B_{yy} & B_{ys} \\ B_{sx} & B_{sy} & B_{ss} \end{bmatrix} \begin{bmatrix} k_x \\ k_y \\ k_{xy} \end{bmatrix} \tag{2.14}$$

$$\begin{bmatrix} M_x \\ M_y \\ M_s \end{bmatrix} = \begin{bmatrix} B_{xx} & B_{xy} & B_{xs} \\ B_{yx} & B_{yy} & B_{ys} \\ B_{sx} & B_{sy} & B_{ss} \end{bmatrix} \begin{bmatrix} \epsilon_x^0 \\ \epsilon_y^0 \\ \gamma_{xy}^0 \end{bmatrix} + \begin{bmatrix} D_{xx} & D_{xy} & D_{xs} \\ D_{yx} & D_{yy} & D_{ys} \\ D_{sx} & D_{sy} & D_{ss} \end{bmatrix} \begin{bmatrix} k_x \\ k_y \\ k_{xy} \end{bmatrix} \tag{2.15}$$

where:

$$\begin{aligned} A_{ij} &= \left[\sum_{k=1}^{n} [Q]_{ij}^{k} (z_k - z_{k-1}) \right] \\ B_{ij} &= \left[\frac{1}{2} \sum_{k=1}^{n} [Q]_{ij}^{k} (z_k^2 - z_{k-1}^2) \right] \\ D_{ij} &= \left[\frac{1}{3} \sum_{k=1}^{n} [Q]_{ij}^{k} (z_k^3 - z_{k-1}^3) \right] \end{aligned} \tag{2.16}$$

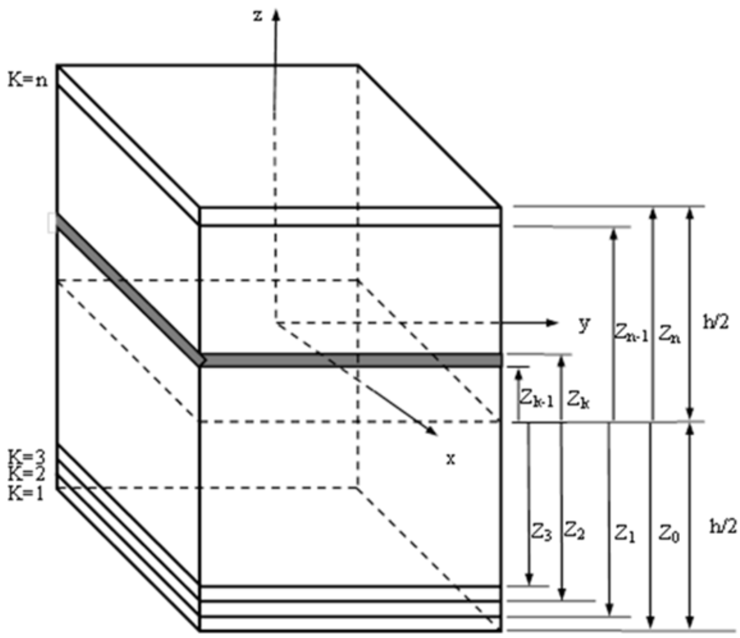

Figure 2.7: Multidirectional plies in a laminate [12].

The relationship between the applied loads and moments and the induced strains and curvatures is provided in equation (2.11), which combines the contributions from the individual plies to find the overall response of the laminate. Given the loads and moments, the deformation can be determined and the stress state in each individual ply can be determined by equation (2.11).

Chapter 3 Contact mechanics

The impact of composites addressed in this thesis involves static and dynamic normal contact between a spherical impactor and a composite laminate plate. Before attempting to investigate this complex situation, the fundamental relationships of static and dynamic contact between a sphere and thick and thin substrates, of isotropic and anisotropic materials, are introduced and utilized in the benchmarking of the ABAQUS simulation.

3.1 Static contact of isotropic materials

When two bodies contact with another under a pressure load, the energy transfers from the indenter to the target and causes different types of deformations. These deformations depend on many factors such as the type of loading, the shape of the indenter, the shape of the target, dimensions of the target and the indenter and the area of contact. In plates, the energy causes bending, shear, membrane and contact deformation. For a half-space under smooth contact, this energy just causes contact deformation or indentation. Thus, the indentation in finite thickness plates is generally smaller than in the half-space under the same load. In this section, the indentation of isotropic and then anisotropic materials is considered. This is firstly considered in the context of a thick substrate, where the thickness of the material is very much greater than the radius of the indenter, and then a thin plate, where the thickness dimension is comparable to that of the indenter radius.

3.1.1 Indentation of an elastic half-space

Static indentation or contact between two smooth elastic solid pioneered by Hertz has been discussed in many books [15], [16]. Essential results from Hertz contact law between two spherical bodies of radii R_1 and R_2 as shown in Figure 3.1, contact occurs in a circular zone of radius a, under load, F,, and the relative displacement between the centres of the two spheres, δ, are [10]

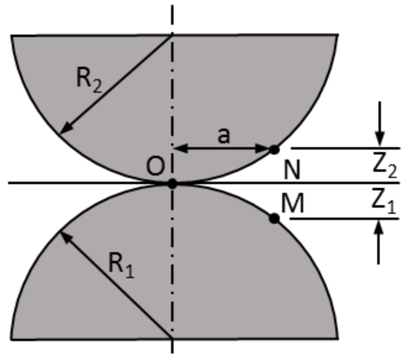

Figure 3.1 Schematic diagram of two spheres in contact [15].

$$a = \left(\frac{3FR}{4E}\right)^{\frac{1}{3}} \qquad \delta = \left(\frac{9F^2}{16RE^2}\right)^{\frac{1}{3}} \qquad p_0 = \left(\frac{6FE^2}{\pi^3 R^2}\right)^{\frac{1}{3}} \tag{3.1}$$

where p_0 is the maximum contact pressure, where R is:

$$\frac{1}{R} = \left(\frac{1}{R_1} + \frac{1}{R_2}\right) \tag{3.2}$$

and E is the equivalent modulus of elasticity :

$$\frac{1}{E} = \left(\frac{1-\upsilon_1^2}{E_1} + \frac{1-\upsilon_2^2}{E_2}\right) \tag{3.3}$$

E is the equivalent modulus of elasticity for both bodies, where E_1 and E_2 are the moduli of elasticity for body 1 and 2 respectively, and ν_1 and ν_2 are the Poisson's ratios for both materials [10].

From equation (3.1) it is simple to show that the contact law in this case is given by:

$$F = K\delta^{\frac{3}{2}} \tag{3.4}$$

where $K = \frac{4}{3}ER^{\frac{1}{2}}$ is the contact stiffness.

These equations are suitable for contact between spheres, and flat surfaces. In case of a flat surface that is considered here, the radius value of the second body is taken to be infinite ($R_2 \to \infty$) so that the effective radius is just the radius of the indenter ($R = R_1$).

As understanding of the contact between two bodies is an essential element of this project, the equations of Hertz in (3.1) are derived in appendix B in some detail. Timoshenko and Goodier [16] show how the equations of contact between any two bodies are derived. When two round bodies contact with each together with zero external loads, they will contact at a point at first and this point represents the initial contact point. As the load increases, the area of contact increases to be a circular area with radius (a). This increasing of contact area due to the deformation of both bodies locally induces a decrease in the separation of the two bodies, known as the indentation displacement (δ).

In this work; we have modeled an elastic Aluminium half-space indented by an elastic steel sphere as shown in Figure 3.2. The dimensions of the Aluminum half-space are (50x40x30 mm). The properties of this model are shown in

Table 1. The contact between indenter and the half-space is surface-to-surface interaction with 0.5 coefficient of friction. The indenter is free to move in the y-direction with 3000 N and fixed in other directions, while the half-space is fixed from its bottom in all directions. The mesh of the half-space is 4-node linear tetrahedron and the total number of elements are 95049 and 7356 for the indenter. To compare our result with the results of equation (3.4). The force-displacement curves from the simulation and the theoretical predictions of (3.4) are shown in Figure 3.3.

Table 1: Properties of half-space model.

	Indenter	**Target**
Part	Diameter of 12.7 mm 3D deformable	3D deformable
Material property	E=210 GPa, v=0.28	E=70GPa, v=0.33
step	$1X10^{-5}$ for total time of 1	
Load	Free in y-direction with 3000 N and fixed in other directions	Totally fixed at its base
Mesh	C3D4: 4-node linear tetrahedron. 7356 elements	C3D4: 4-node linear tetrahedron. 95094 elements

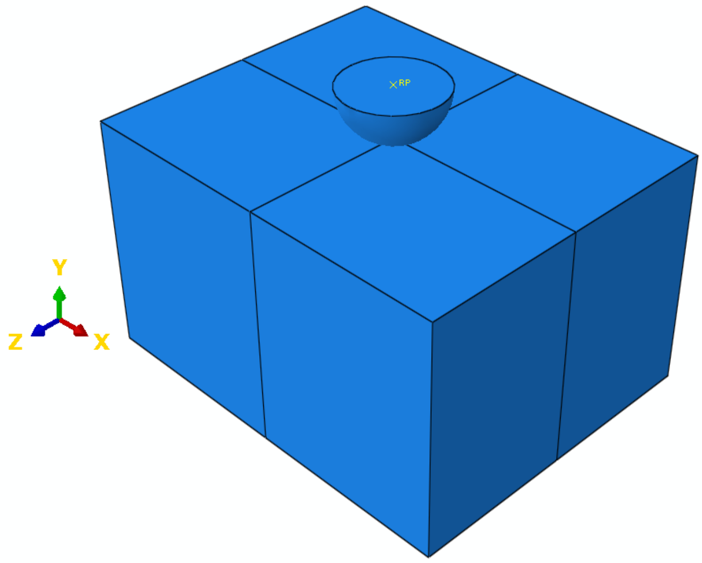

Figure 3.2 : Benchmark model of half space rigid indenter on half-space target.

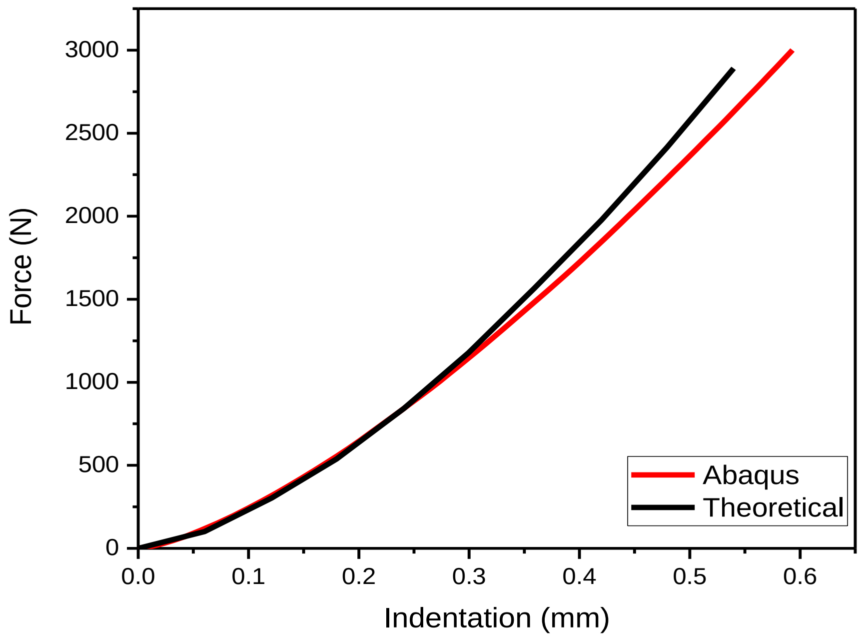

Figure 3.3: Comparison between ABAQUS and theoretical results for an isotropic half-space.

There is an excellent agreement between ABAQUS and equation result in the low load stage as expected. This difference increases as the load increases. This is also expected as the Hertz contact law only applies for low load ranges. The small difference in the higher load range is because the Hertz contact law assumes deformation is small, but this assumption breaks down as the indentation depth becomes a significant fraction of the indenter radius.

3.1.2 Indentation of an elastic isotropic plate

The contact law which was pioneered by Hertz does not take the effect of the substrate thickness into account. For a thick substrate, the total deflection under a rigid indenter is equal to the indentation. This is not the case for loading of plates because the deformation in a plate includes two types of deflection: local deflection (due to indentation) and the overall bending deflection of the plate, which is typically much greater than the local indentation, especially for thin plates. This is illustrated in Figure 3.5. The flexibility of plates reduces the local deformation, and hence for this reason the thinner the plate the smaller the indentation that is induced [17]. The plate deflection is taken to be the displacement of the back-face at the centre of the plate (directly below where the indenter is applied) and the indentation is defined to be the total displacement of the indenter minus this back-face displacement. These definitions are adopted throughout the rest of this thesis.

To clarify the effect of thickness on the elastic indentation of an isotropic plate, this study investigates plates of different thicknesses and compares the results with the half-space model of section 3.1.1. The effect of plate thickness on the force-indentation curve is shown in Figure 3.5 while the stresses in the half-space and in a plate of thickness (12.7, 9.525, 6.35 mm) are compared in Figure 3.5. The detail of this model shown in Table 2

Table 2: Model details of figure 3.4.

	Indenter	**Target**
Part	Diameter of 12.7 mm 3D deformable	3D deformable
Material property	E=210 GPa, v=0.28	E=2Gpa, v=0.33
step	$1x10^{-5}$ for total time of 1	
Load	Free in y-direction with 3000 N and fixed in other directions	Totally fixed at its base
Mesh	C3D4: 4-node linear tetrahedron.7356 elements	C3D4: 4-node linear tetrahedron. 95094 elements

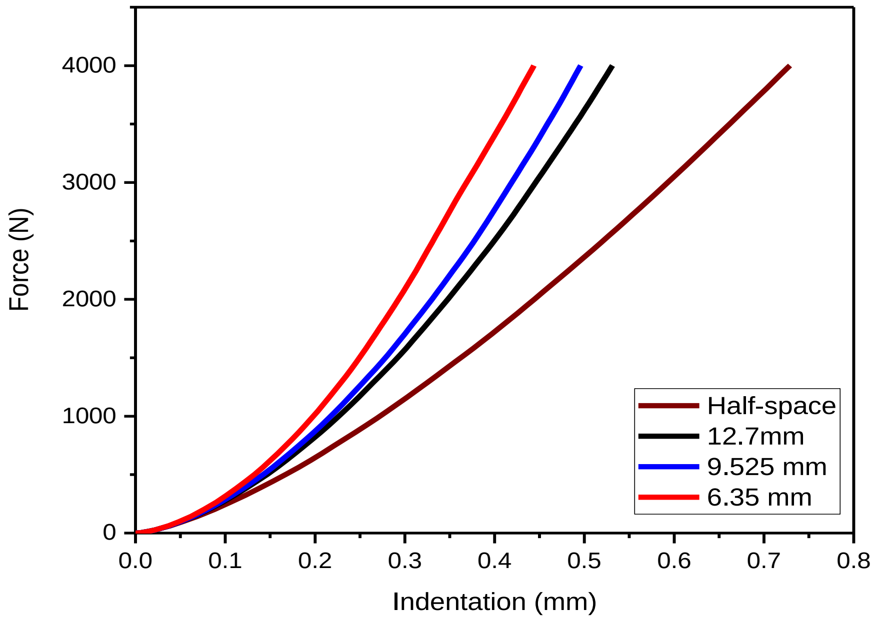

Figure 3.4: The effect of plate thickness on the force–indentation curve for the indentation of an elastic, isotropic plate by a spherical indenter of radius 6.35mm.

As shown in Figure 3.4, the thickness has a significant effect on the results. As the thickness decreases the indentation decreases as expected, as the flexibility of the plate increases, the global deflection of the plate becomes much greater than the local indentation.

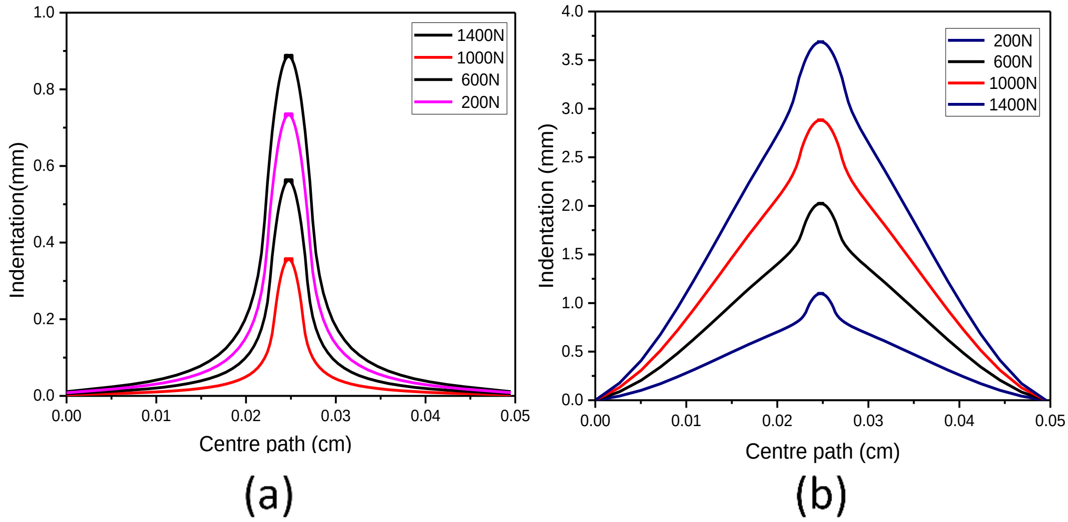

Figure 3.5: Effect of thickness on indentation curve of isotropic model (a) half space (b) 6.35 mm thickness plate.

From Figure 3.4b it can be seen that the displacement far from the centre of the plate is much greater than in the half-space case of Figure 3.4a. The deflection shown in the previous figure is the total deflection of the specimen which is the sum of global deflection and indentaion for the plate case. In the half-space model,there is no global deflection but the total deflection comes from the indentation. This can be considered to be almost entirely due to bending. The displacement due to the indentation can be seen at the centre of the plate and induces a highly localised increase in the deformation.

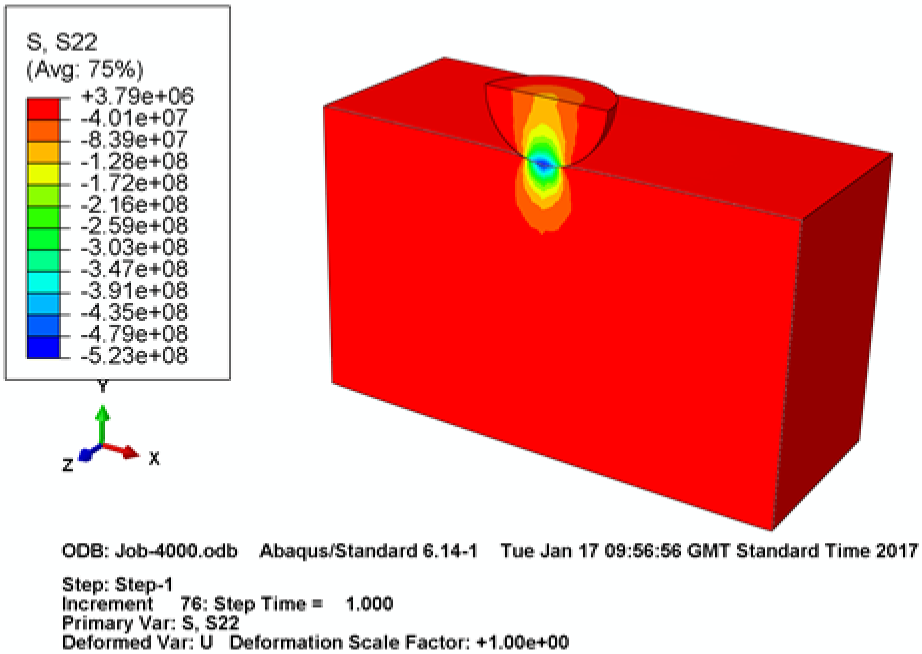

A

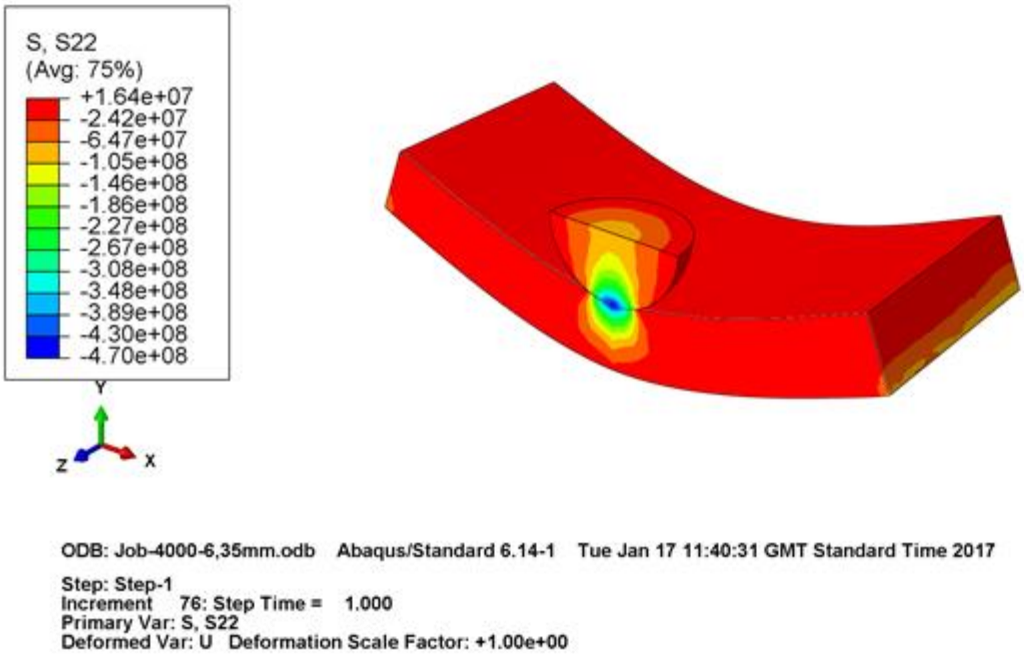

B

Figure 3.6: Comparison between the stress of (a) an elastic, isotropic half-space and (b) an elastic isotropic plate of thickness 6.35 under the action of a spherical indenter of radius 6.35mm.

As shown in Figure 3.6, the stress distribution of the plate is quite similar with the half-space case in term of the shape of the stress but the maximum stress in the plate is larger than the stress in half-space. This because the stress concertation in plate case is bigger than the half-space due to the curvature of the plate around the indenter which results bigger contact area.

3.2 Static contact of anisotropic laminates

3.2.1 Hertz contact law for anisotropic half-space

The basic assumption for the Hertz contact law is that both bodies in contact have infinite dimensions and isotropic properties and it describes the relationship between the force of indentation and indentation displacement as in equation (3.1). For composite materials, the contact force is found to be proportional to the transverse modulus of the composite and independent of the longitudinal modulus, which had been suggested by Yang and Sun [18]. Many researchers tried to use this law in different types of materials [18] in the same form as (3.4) but with a modified contact stiffness constant of

$$K = \frac{4}{3}\sqrt{R}\,E_3 \tag{3.5}$$

where E_3 is the Young modulus for the first ply in the thickness direction.
This form has a good agreement with experimental work, especially for low load range. Swanson [19] and Turner [20] have modified Hertz contact formula for anisotropic materials:

$$F = \frac{4}{3}\sqrt{R}\,E_{T1}^{*}\,\delta^{1.5} \tag{3.6}$$

$$a = \left(\frac{3RF}{4E_{T1}^{*}}\right)^{\frac{1}{3}} \tag{3.7}$$

where a is the radius of the contact area, and the anisotropic modulus E_{T1}^{*} can be found from

$$\alpha_1 = \left(\frac{\frac{E_x}{E_y} - \upsilon_{xz}^2}{1 - \upsilon_{xy}^2} \right) \tag{3.8}$$

$$\alpha_2 = \frac{1 + \left(\frac{E_x}{2G_{xz}} - 1 \right) - \upsilon_{xz}\left(1 + \upsilon_{xy}\right)}{1 - \upsilon_{xy}^2} \tag{3.9}$$

$$\alpha_3 = \left\{ \frac{\alpha_1 + \alpha_2}{2} \right\}^{\frac{1}{2}} \left\{ \frac{1 - \upsilon_{xy}}{2G_{xy}} \right\} \tag{3.10}$$

$$E_{T1}^* = \left(\frac{2}{\alpha_1 \alpha_3} \right) \tag{3.11}$$

Where α_1, α_2, α_3 constant of the material.

3.2.2 Static contact for an anisotropic plate of finite thickness

Plate thickness has no effect on the force-indentation curve for small contact force and the shape of this curve will almost follow the half-space curve. For larger indentation, the contact area increase and significant deviation from Hertzian contact law is observed [10]. Swanson (2005) [19] has proposed an empirical factor to correlate the Hertz contact law for an anisotropic laminate of finite thickness.

$$F_{\mathrm{finite}} = \beta \, F_{\mathrm{Half-space}} \tag{3.12}$$

where β is a force coefficient which depends most critically on the plate thickness to contact area ratio.

The response of the plate depends on many factors such as the plate thickness, contact radius, indenter radius and the mechanical properties of the target material. If the ratio of plate thickness to contact radius was just above 4 we can treat it as a half- space as shown in Figure 3.7 below.

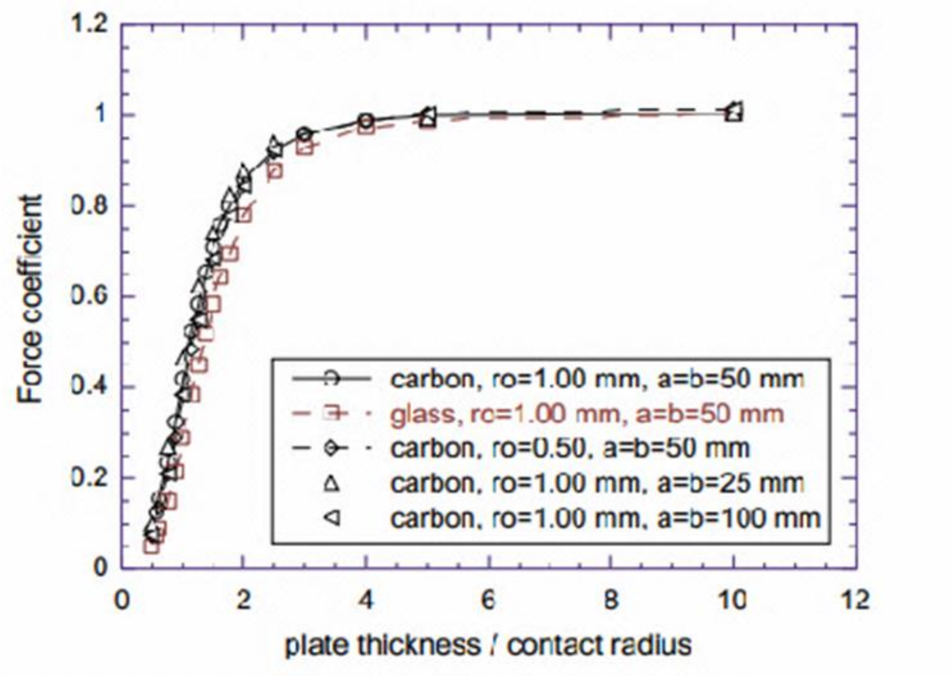

Figure 3.7: The correlation factor of different types of composite [10].

In this project, the ratio of plate thickness to the contact radius is 2, 1, and 0.5. Thus, for all cases, the indentation consider as a finite thickness indentation.

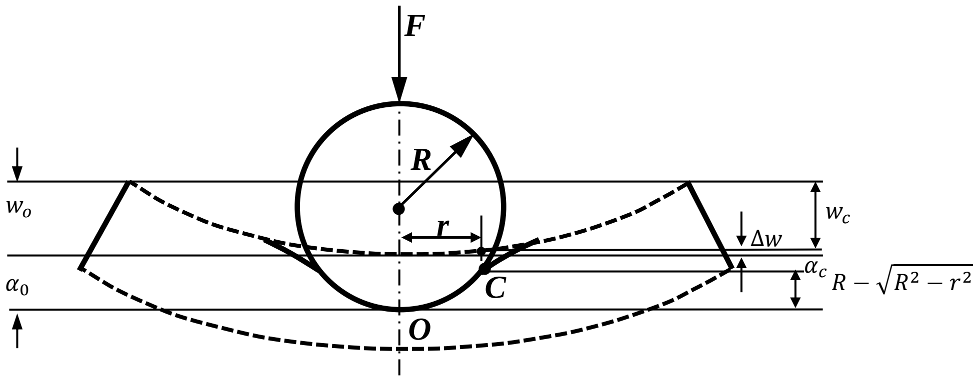

Figure 3.8: A schematic diagram showing contact between a rigid sphere and a plate[14].

Puhui Chen et al [21] have proposed an equation to determine the indentation in plates. If a sphere of radius R contacts with a plate under a contact force F, the relationship of the plate deflection as shown in Figure 3.8 will be:

$$w_0 + \alpha_0 = \ w_c + \alpha_c + R - \sqrt{R^2 - r^2} \tag{3.13}$$

where: w_0 and α_0 the deflection of the points **o** and **c** which has a distance **r** from the centre respectively.

$$\Delta w + \alpha_0 = \ \alpha_c + R - \sqrt{R^2 - r^2} \tag{3.14}$$

$$\text{Where} \quad \Delta w = w_0 - \ w_c$$

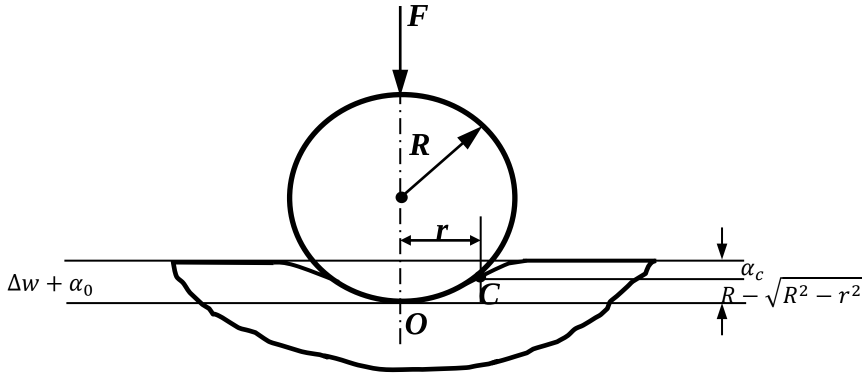

Figure 3.9: Contact between rigid sphere and a half-space [14].

If we assume that the indentation of the half space shown in Figure 3.9 is the same as the deflection and indentation of the plate under the same contact force we have

$$\Delta w + \alpha_0 = \ \alpha_0^*$$

where α_0^* is the indentation of the half-space. Also, if the form of force indentation equation takes the same shape of Hertz law:

$F \ = K\alpha^{\frac{3}{2}}$ For plate

$F \ = K^*(\alpha^*)^{\frac{3}{2}}$ for half space

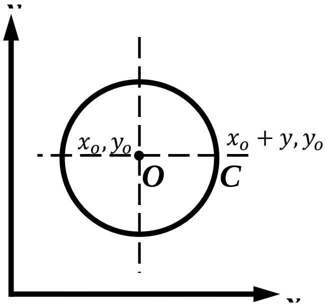

Figure 3.10: Coordinate definition of contact points [14].

Equation (3.13) will be

$$w(x_0, y_0, F) - w(x_0 + r, y_0, F) + \left(\frac{F}{K}\right)^{\frac{2}{3}} = \left(\frac{F}{K^*}\right)^{\frac{2}{3}} \qquad (3.15)$$

From equation (3.15), we can find the indentation of the plate by calculating the indentation of the half-space at the same force and we use this value in the equation above.

The most straightforward way to validate the results from Abaqus and the result from this equation is by comparing both results with an experimental work that was done by Wu and Shyu [14]. The experimental study was carried out on a composite plate with laminate layup $[0/90]_{4s}$, the details of the indenter and the plate are listed in Table 3.

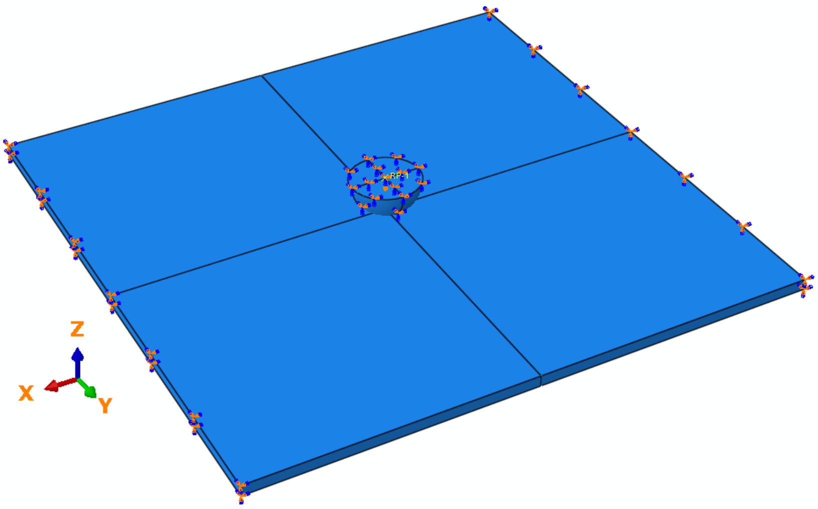

Figure 3.11: Benchmark model of figure 3.12 [14].

Table 3: Model details of figure 3.12.

	Indenter	Target
Part	Diameter of 12.7 mm 3D deformable	100x100x2 mm^3. 3D deformable
Material/ property	E=210GPa, v=0.28	E_1= 148GPa, E_2=E_3=10 GPa, G_{12}= G_{13}= 4.74 GPa and v_{12}= v_{13}=0.31
step	1×10^{-15} for total time of 1sec	
Load	Free in y-direction with 450 N and fixed in other directions	fixed along its two sides and free for the other two
Mesh	C3D4: 4-node linear tetrahedron.7356 elements	SC6R 6-node triangular in-plane continuum shell. 43480 elements

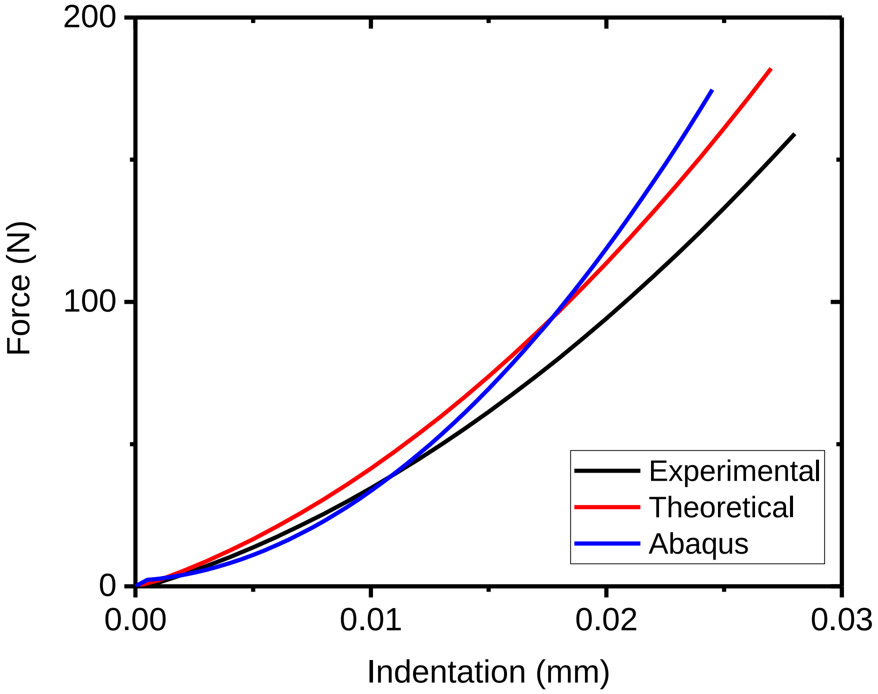

Figure 3.12: Comparison between ABAQUS results, theoretical, and previous experimental results for a composite plate.

Figure 3.12 shows that there is a good agreement between ABAQUS results and the other results .e. experimental and theoretical results under 0.01mm. This is acceptable as the indentation in the experimental work does not exceed this amount of indentation. This indicates that ABAQUS is good enough to capture the indentation of composite laminates under the indenter in this range of force.

3.3 Dynamic loading

The difference between static and dynamic loading is two fold. Firstly, there are two characteristic response times, the contact time between the impactor and the composite, and the inertial response time of the total structure. The ratio of these response times allows impact, or dynamic loading, to be divided into three groups: low, intermediate, and high-velocity impact. In high-speed impact loads, the contact time between objects is generally very short and the impacted structure does not have the time to absorb enough amount of energy. Thus, the damage resulting from such types of impact is localised in a very small area around the contact area. This type of impact is also called ballistic or wave-controlled impact, as it is dominated by stress wave propagation through the thickness of the material. High-velocity impact usually ranges from 50m/s to 100 m/s [10]. The response of this type of impact is shown in Figure 3.13-a Intermediate-velocity impact events lie in the range of 10m/s to 50m/s and the typical response of this type of impact is shown in Figure 3.13-b. the response of this type of impact is also designated as wave-controlled impact. Intermediate-velocity impacts are usually caused by secondary blast debris and runway debris. On the other hand, low-speed impact lays under 10 m/s and the total structure has the time to respond and absorb most of the energy elastically or may exceed initiation and propagation failure stages. The response of this type of impact is shown in Figure 3.13-c. The low-velocity impact will be the focus of this thesis.

The second effect is that stresses are transient and evolving over time. Therefore it is expected that stresses will develop within the composite that are higher than the equilibrium (static) values that are eventually realised. It is the consequence of these fleeting peak stresses on the initiation and propagation of damage within the composite that are of interest.

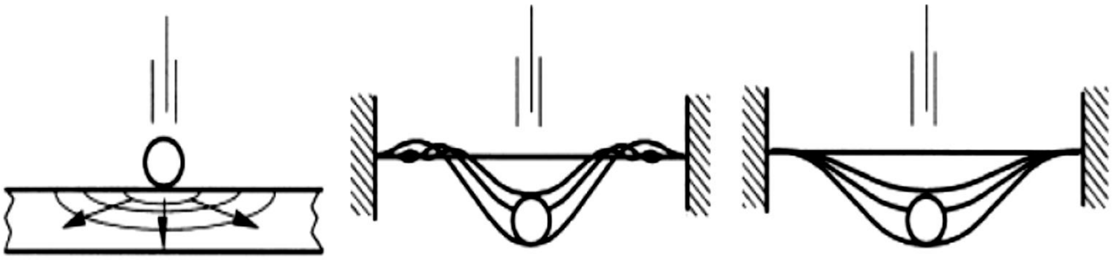

(a) (b) (c)

Figure 3.13: (a) High velocity (b) Intermediate-velocity (c) Low-velocity impact [22].

3.3.1 Low-velocity impact

The limit of this type of impact varies from 1 to 10 m/s depending on many factors such as target stiffness, material properties, and the impactor mass and stiffness as these factors affect the natural time period of the system. One criterion is to compare the time of load application to the natural time period of the system. If the load application time is less than one-half of the natural time period, then an impact phenomenon occurs. If the load application time is more than three times the natural time period of the system, then the loading is quasi-static. In between there is a grey area In the range below 5 m/s, the response is controlled by impactor to target (laminate) mass ratio rather than impact velocity [22]. The energy of a low-speed impactor is absorbed by the laminate resulting in an internal damage that is non-visible. This type of damage is called barely visible impact damage (BVID). The test techniques that are generally used to simulate the impact events also affect the classification of impact events as well as the range of velocity according to Cantwell and Morton [23] for low-velocity impact. These techniques include Charpy, Izod, and drop weight impact tests.

This thesis will consider drop weight impact testing. This type of test is generally used for flat plates placed in a horizontal plane. The plate is subjected to a known weight falling from a specific height. The amount of impact energy can be controlled by the drop height and the mass of the impactor and its holder. This type of test is now increasingly used to study the impact behaviour of composites. The size and type of damage in the laminates is a key factor to measure the damage resistance of the material. In this test, a wide range of sample geometries can be tested with different shapes of the impactor. ASTM D 7136 standard is usually performed this type of impact [23].

To investigate the evolution of stresses inside an elastic composite laminate, a composite laminate with [0,45,90,-45]s layup and 30x30x1 mm3 dimensions have been simulated under low-speed impact resulting from a rigid impactor with 4mm diameter. The main delamination damage under this type of loading will be between plies 7 and 8 (on the back face of the plate) as will be discussed in chapter six and seven. Thus, the stress distribution within these plies is important to understand the effect of these stresses on the shape of delamination in this area. These shapes are shown in the following figures. This analysis was performed on quad-core Intel i5-3470 processor and 32 GB RAM using the MPI based parallel solver available in ABAQUS/ Explicit. A total computing time of approximately 10 h was required for the simulation of a typical impact event. The computing time reduced to about 1 h when damage was not implemented in the model.

Table 4: Mechanical properties of UD/M55J composite laminate.

	Indenter	**Target**
Part	4mm diameter, 3D deformable	30x30x1 mm^3 ,3D deformable
Material/ property	Rigid	E_1= 300GPa, E_2=E_3=12 GPa, G_{12}= G_{13}= 3.6 GPa and v_{12}= v_{13}=0.3, ρ=1650 g/cc X_t=2738 MPa, X_c,= 1459 MPa Y_t=50 MPa, Y_c=250 MPa, G_{xt}=31700 J/m^2, G_{xc}= 15940 J/m^2, G_{yt}= 200 J/m^2, G_{yc}=2000 J/m^2
step	$1x10^{-5}$ for total time of 0.002 sec	
Load	Free in y-direction with velocity of 1.134m/sec and fixed in other directions	Rest free on support which totally fixed at its base.
Mesh	R3D3. 3-node 3-D rigid triangular. 2672 elements	C3D6. 6-node linear triangular. 77904 elements

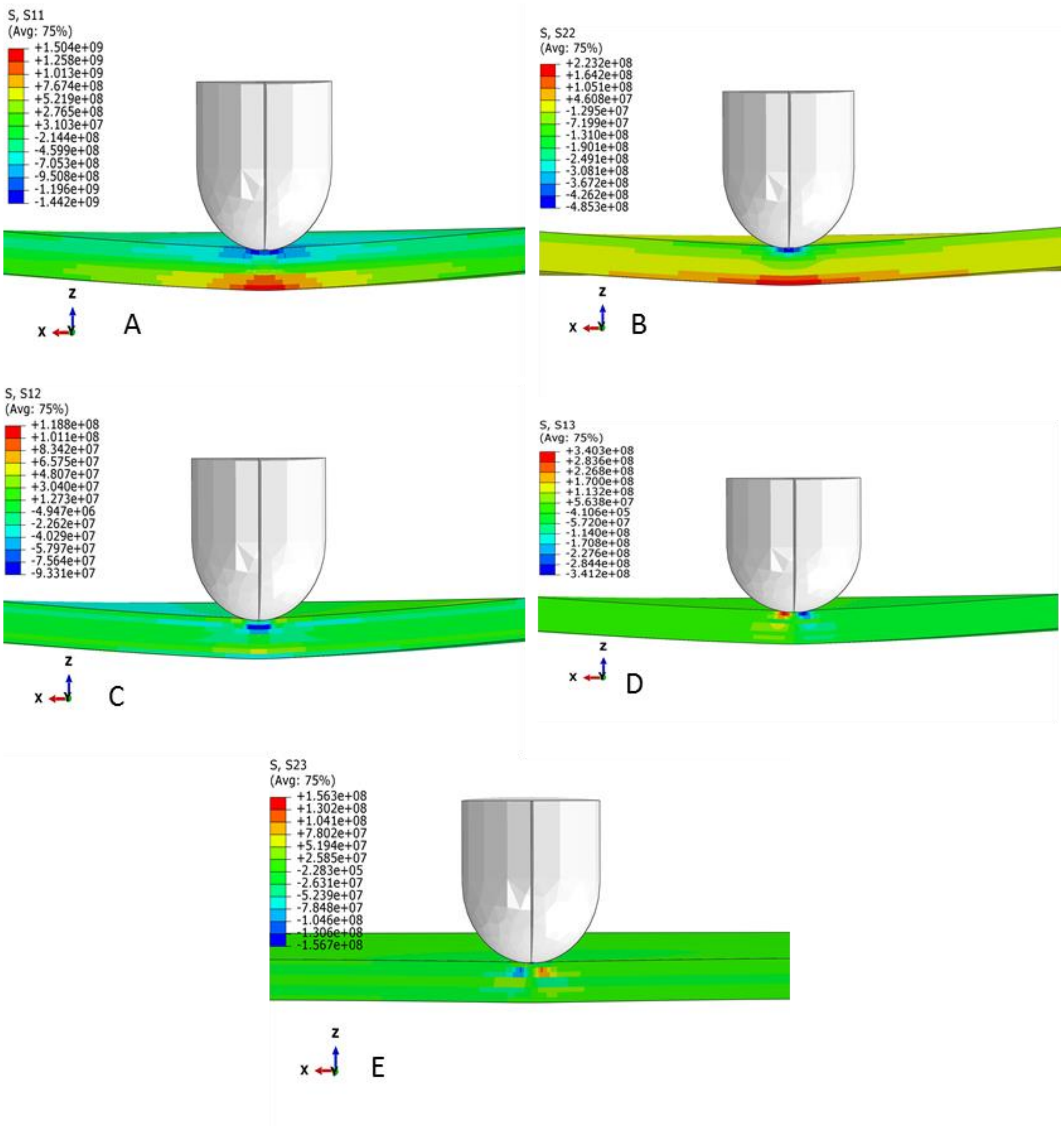

Figure 3.14: Stress distribution along laminate cross section (A) S_{11}. (B) S_{22}. (C) S_{12}. (D) S_{13}. (E) S_{23}.

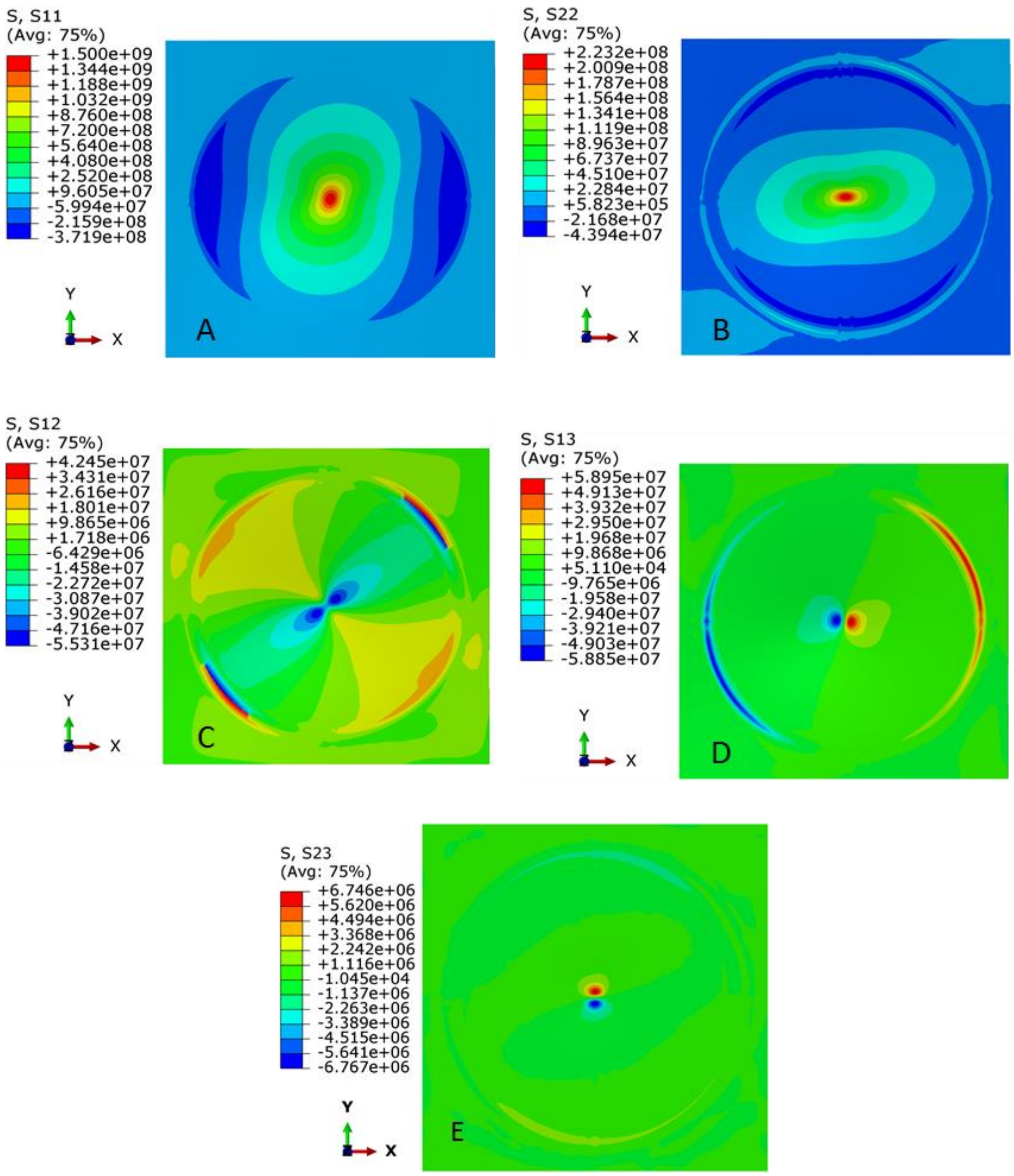

Figure 3.15: Stress distribution in the bottom ply 8 (A) S_{11} (B) S_{22} (C) S_{12} (D) S_{13}. (E) S_{23}.

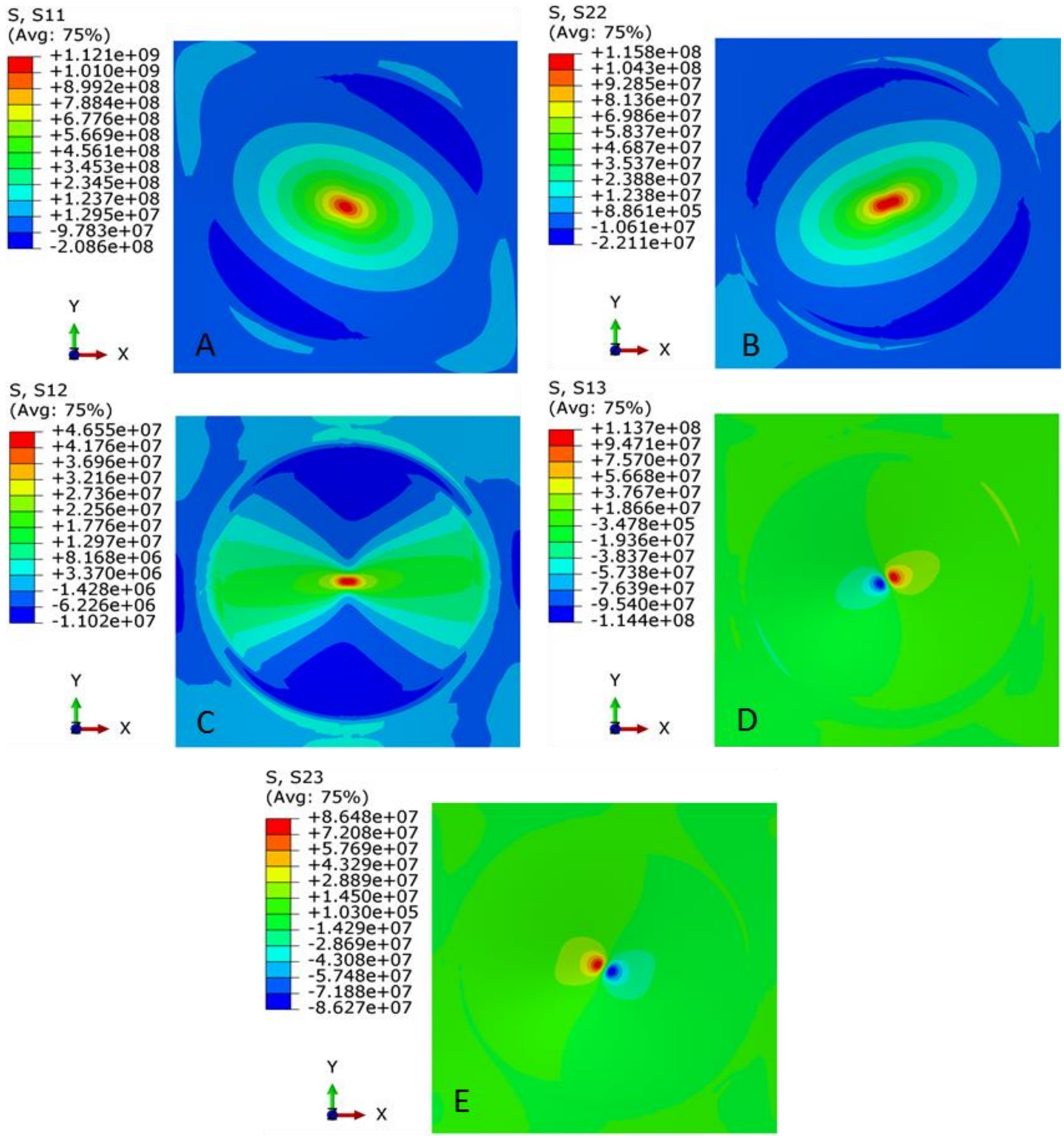

Figure 3.16: Stress distribution in the next to bottom ply 7 (A) S_{11}. (B) S_{22}. (C) S_{12} (D) S_{13} (E) S_{23}.

As shown in Figure 3.14 Figure 3.15, and Figure 3.16, the outer ring is seen in Figure 3.15 and above is where the plate makes contact with the cylindrical support. The stresses along fibres (S_{11}) and across fibres (S_{22}) are in compression at the top of the laminate and in tension at the bottom of the laminate due to bending. The dominant stress in the bottom plies (7 and 8) is the stress along the fibres, S_{11}. The shape of the out of plane shear stresses in these plies as shown in Figure 3.15 (C, D, and E) looks like a number 8. So out-of-plane shear stresses drive delamination between these plies as it considers the important factor for matrix cracking as it will be discussed in Hashin criterion in section1.1.1.5.

This section has considered the theoretical elastic response of thick and thin, isotropic and anisotropic structures to static and dynamic contact loads. To understand and investigate the evolution of these structures beyond the elastic limit it is necessary to introduce the relevant failure processes into the model. This is the subject of the next chapter.

Chapter 4 Modelling of failure in plies and laminates

Accurate prediction of composite structure failure depends on modelling the progressive development of all damage modes, such as matrix cracking and delamination and the interaction between them. The combined effect of different damage modes acting on the complex shaped composite structure under arbitrary loading conditions cannot be handled properly with analytical models because of the complexity of composite material behaviour. Therefore, numerical techniques such as the finite-element method are important to predict the damage behaviour of composite structures accurately.

In this chapter, the modelling composite material at different length scales will be discussed in section 4.1 followed by mesoscopic and failure mechanisms in composite materials in sections 4.2 and 4.3. The following section will discuss two types of damage in composite materials e.g. intra-ply and inter-ply damage in terms of initiation and propagation. In final sections, discussion of modelling the impactor, mesh sensitivity and contact interaction will be presented.

4.1 Modelling of composite materials at various length scales

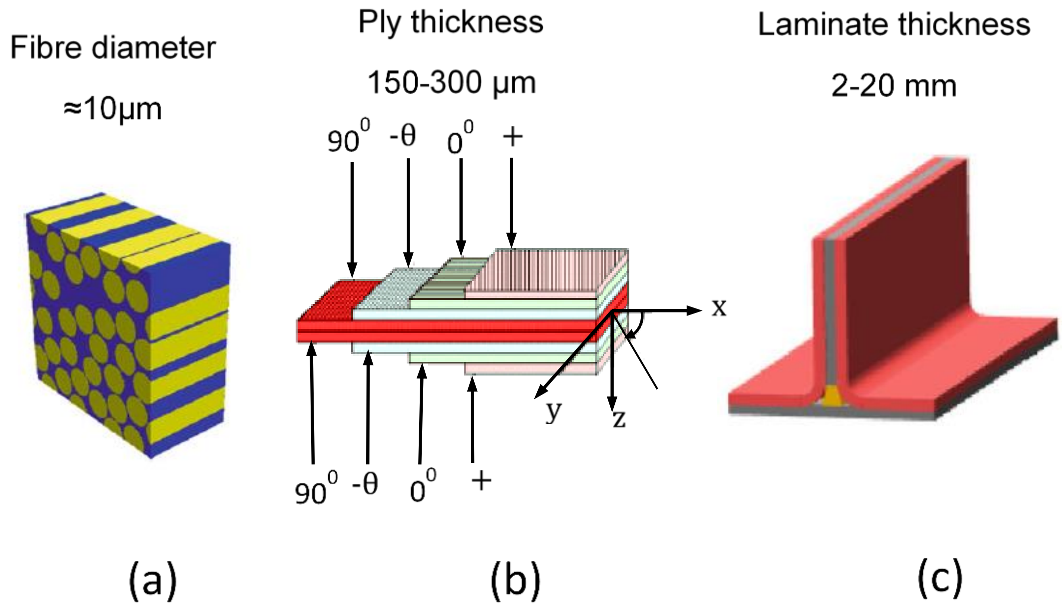

Figure 4.1: Hierarchical structure of composite materials, the three entities and their length scale (a) Individual fibres and matrix (microscopic) (b) Inidividual plies and laminate (mesoscopic) (c) Complete component (macroscopic) [24].

One of the main advantages of composite materials is that they are tailor-made for a specific application. This feature makes the overall macroscopic properties of composite structures depend on the microscopic properties of individual composite components. Therefore, it is essential to deal with the damage of composite materials at different levels or scales [2]. Studying composite structures at different scales occurs through a multi-scale approach which deals with three different scales of composite structures: microscopic, mesoscopic, and macroscopic, as shown in Figure 4.1.

The aim of this technique is to determine the relationships between the response of the structure at different scales through building a micro-model which is easy and simple [25]. The properties at various scales are predicted by the multi-scale material model and correlate them with a continuum mechanics approach.

Generally, there are three types of approaches to deal with composite structure damage: micro-damage mechanics (MIDM), mesoscopic and macro-damage mechanics (MADM).

1. Micro-scale: This scale looks at the individual fibre scale for the formation of cracks and voids. This is the lowest observation scale. The main concern on this scale is the interaction between fibre, matrix, and the interface and the resulting behaviour of the composite [2].
2. Meso-scale: individual plies are considered as the basic element of this scale to analyse and predict failure of the entire laminate. Each ply should be modelled separately taking into account the orientation of fibres, but there is no direct modelling of the interaction between matrix and fibres. The mechanical properties of these plies are calculated experimentally. Modelling in this scale is much less computationally intensive than a similar structure simulated at a micro-scale. In a CFRP, modelling is carried out by building each ply with a specific orientation and adjacent plies are connected by a cohesive layer to capture the delamination between plies. The overall response of composite structures strongly depends on the properties of individual plies and the connection between them. In this study, meso-scale has been used to simulate the response of the composite plates, as discussed in the next section 4.3
3. Macro-scale: In this scale, the model is defined at the level of an entire composite component, which considers it as a perfectly homogenous continuum with an anisotropic material. The response of the whole component will be an average response as it is investigated using effective material properties. This type of modelling is simple which saves time and reduces the total computational cost. On the other hand, the model is not necessarily accurate because the detail of the damage is not captured which leads to a lack of physical representativeness [26].

4.2 Mesoscopic modelling of damage mechanisms

Prediction of composite material failure is complicated due to the connection between the different damages types within the composite structure. This section discusses the different methodologies adopted for modelling intra-ply and inter-ply failure at a mesoscopic scale. Using a semi-empirical approach is a good way to design most composite structures because it is difficult to predict a complete damage process. Various failure modes result from the complexity of the damage in composite materials and their unique pattern of interaction. Damage initiation and evolution due to the failure of the first ply does not lead to ultimate failure of the entire structure. Therefore, it is essential to find an accurate model capable of simulating all damage processes starting with damage initiation through to damage evolution and the final failure stage. This requires validated constitutive laws calibrated using experimental and theoretical studies for the same case of the damage mechanism. The challenge of creating such a model also requires the understanding of the sequence of different damage modes and defining the materials parameters which specify the dominant failure modes. A more serious challenge to creating an accurate model is to categorise many mechanisms of damage and represent them in the reliable and physical model.

According to [27], the requirements of damage initiation and evolution analysis in composite materials are the ability to: (a) Evaluate the stress and strain within individual plies. (b) Define single lamina failure criteria. (c) Evaluate the effect of damage on ply stiffness degradation. (d) Continue to evolve the damage within the structure to account for the interaction between mechanisms. The approach of simulating crack initiation and damage evolution are discussed below.

4.3 Failure mechanisms

The strength of a material can be defined as the materials capability to resist failure. For orthotropic materials, there are three principal directions and the laminate has a different strength in each direction. For this reason, the maximum strength of a laminate may not indicate the critical loading condition. Thus, the failure criterion of composite structures should be calculated based on the specific direction of the load compared to the allowable stress in this direction. The microstructural heterogeneity of composites arises from the differences between the components material properties, and the interface between them, in addition to the multi-directional anisotropy introduced by the fibres themselves. Moreover, the presence of an interface between plies introduces the potential for multiple cracking when stress is transferred between plies [2]. This all makes the process of studying damage in composite materials extremely complex.

These many different types of failure in fibre-composite laminates can be classified into two categories [28]:

- Intra-ply failure that includes fibre damage, matrix damage and fibre-matrix interface damage.
- Inter-ply failure, which includes delamination between adjacent plies.

4.4 Intra-ply failure mechanisms

The various types of intra-ply damage are illustrated in Figure 4.2 and are related to either the initial failure of the fibres, the matrix or the interface between them. The type of failure of fibres depends on the loading type: fibre rupture occurs in tensile loads (Mechanism 4) while fibre micro-buckling occurs under compressive loads (not shown). On the other hand, matrix failure depends on the nature of the matrix, whether it be ductile or brittle. A ductile matrix will fail by the nucleation and growth of voids in areas of high tensile stress (Mechanism 5), whereas a brittle material will fail by propagation of a dominant crack in the matrix. The path of the crack depends on the properties of the fibre-matrix interface. Interfacial strength depends on the type of matrix and fibre and the bonding between them, if any. When the interface is weak, fibre debonding occurs (Mechanism 3), and a crack will prefer to progress through the matrix but around the fibres, leaving the fibres largely intact at first (Mechanism 2) in a mechanism known as fibre bridging [39]. Eventually, fibre pull-out failure occurs

(Mechanism 1) as the load on the exposed fibres behind the crack tip exceeds their tensile strength.

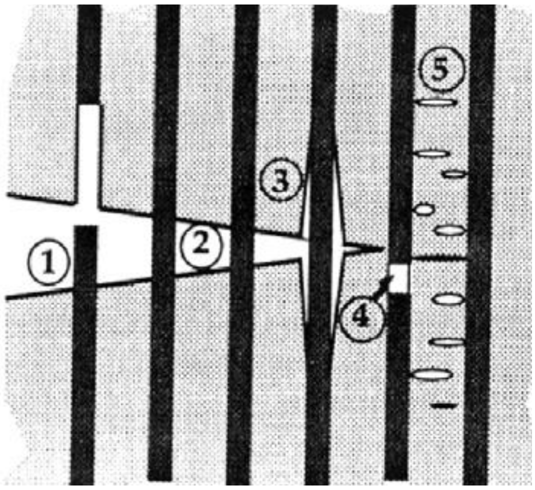

Figure 4.2: Intra-ply failure of composite lamina [27].

The role of the fibres, the matrix and the interface are discussed in more detail in the following.

4.4.1 Fibre failure

Fibres are generally made from materials which have higher strength than the matrix, and due to the structure of composite laminates, the fibres carry most of the external loads. When any fibre fails, the remaining fibres carry an additional load and this increases the probability of failure for intact fibres. This may then lead to catastrophic failure of the whole laminate. The type of fibre damage depends on the type of loading, i.e. tensile or compressive load. In tension, the load causes fibre breaking or rupture which can lead to fibre pull-out. In compression, the main type of fibre damage is micro-buckling or crushing [29]. Many researchers have produced different formulas to describe the conditions for the onset of failure. In this work, we have used the finite element (FE) program ABAQUS which includes the Hashin damage model [30]. Hashin assumes that fibres can be treated as a homogenous and isotropic material and defines that fibres can fail by different mechanisms under the three load cases shown in Figure 4.3. Failure in fibres depends on the type of loading. In a unidirectional composite loaded in tension along the fibres the failure occurs at fibre weak points and stress redistribution between fibres and matrix occurs (Case a). This will affect other fibres in the local vicinity of the broken fibres adding an extra load on the fibres around the broken fibre. If the lamina is loaded in compression, the micro buckling failure of the failure occurs (Case b). The third type of fibre failure occurs when the laminate is loaded in compression in the out of plane direction [2]. The fibre fails under crushing stress under this type of loading [31] (Case c).

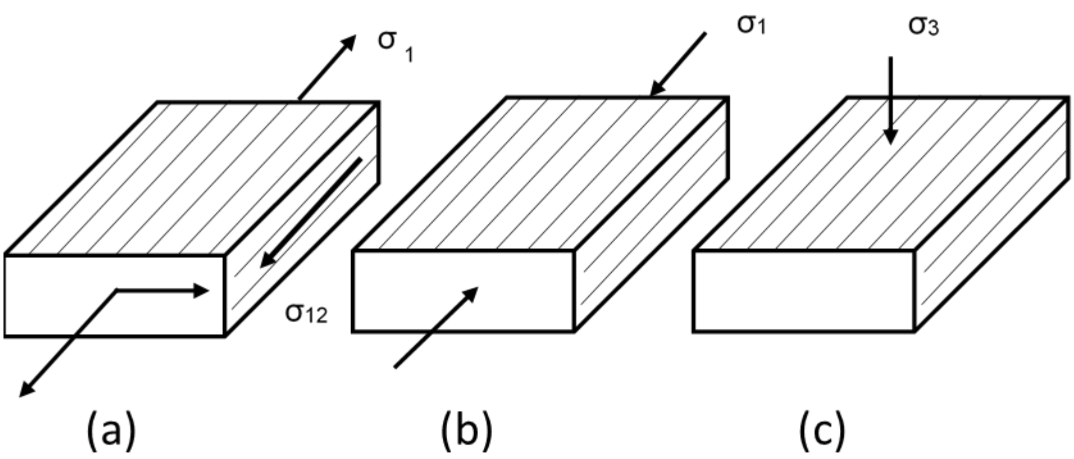

Figure 4.3: Stresses inducing failure in fibres.

4.4.2 Matrix failure

In composite materials, the matrix provides protection for the fibres and tries to distribute the external loads between them. This increases the performance of the whole composite structure [12]. Failure of the matrix within a laminate depends on many factors such as the nature of the matrix itself, whether it is brittle or ductile, the type of loading and the in-service temperature. Generally, the two main types of failure in a matrix are matrix cracking and matrix crushing. This depends also on load type i.e. tension or compression. In tension load, all criteria of the matrix failure under tension assume that the critical fracture plane is in the transverse tension direction, and generally involve the interaction between the tensile normal and in-plane and out-of-plane shear stresses (Case (a) in Figure 4.3). Under compression loading, the matrix fails by crushing with the same interaction between stresses as in tension. The fracture plane is also assumed to be in transverse tension direction [32] (Case b). These two types of failure typically happen under impact loading. Usually, the opposite side of the impacted laminate fails first due to the tensile load which arises because of bending [33]. The initiation of damage on this side begins with voids in a ductile matrix or cracks in a brittle matrix. The defects grow and eventually cause delamination. For the impact face, the matrix fails usually by crushing due to compression. Hashin assumed that the failure mechanism of the matrix in a laminate depends the type of stress e.g. (tension or compression) as shown in Figure 4.4 .

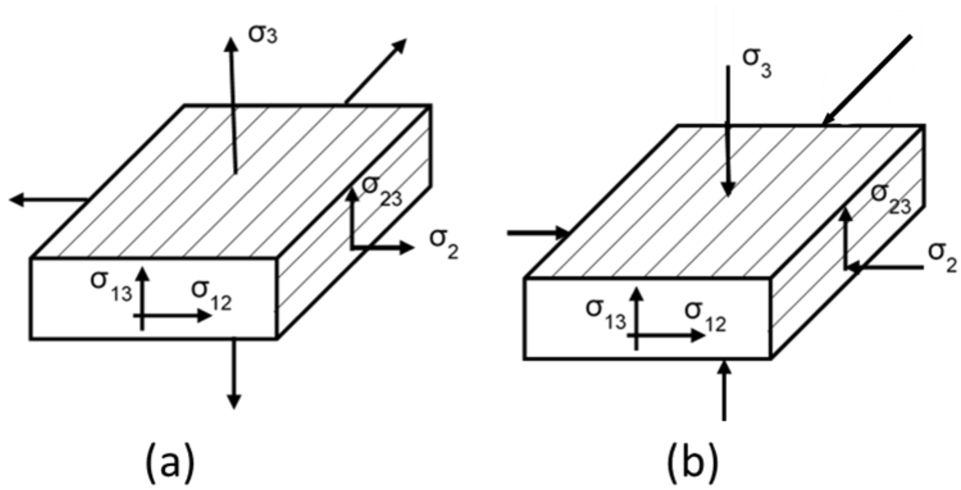

Figure 4.4: Stresses inducing failure in matrices.

4.4.3 Fibre–matrix interface

The third and last type of intra-ply failure is a failure of the interface between the fibres and the matrix.The type of bond between the fibre and the matrix plays an important role in the transfer of stress between these entities. The strength of the interface determines the type of failure of the ply. For instance, if the bond is highly strong, the composite fails catastrophically because all entities fail together. On the other hand, weak bonds fail at lower stress. Generally, the interface is the weakest entity within a laminate. Its failure occurs when some voids form allowing the fibre and matrix to separate. This may then lead to fibre bridging and fibre pull-out [28]. The properties of the interface can be tailored in many ways such as by increasing the roughness of fibres, or by chemical action, or by choosing matrices and fibres which adhere together. Interfacial failure happens when the shear stress around fibres equals or exceeds the shear strength of the interface. This essential composite property can be found by using a push- in test methodology as shown in Figure 4.5

$$\tau_c^{sl} = \frac{S_0 P_c}{2\pi^2 r^3 E_1^f} \tag{4.1}$$

where S_0 is the slope of linear stage of load –displacement curve (as shown in Figure 4.5b), P_c is the end of a linear stage of the same figure, r is the radius of the fibre, and E_1^f is the elastic modulus of the fibre in the longitudinal direction.

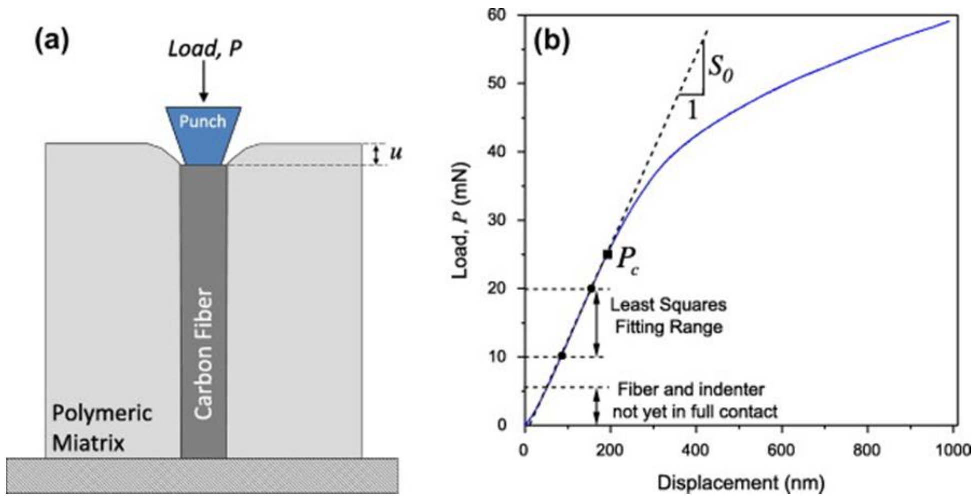

Figure 4.5: (a) Schematic of the fibre push- in test (b) Load displacement curve [34, 35].

4.5 Initiation of intra-ply damage:

4.5.1 Strength-based criteria for intra-ply failure

Damage in materials consists of two stages; initiation and propagation. The first stage happens when the local stress equals or exceeds the tensile strength of the material. Strength-based failure criteria can estimate the failure onset in composites. This criterion can also predict the propagation stage depending on many factors such as; type of material, the shape of the component, and type of loading. Microcracks occur when the transverse shear stress reaches the critical transverse tensile stress of the ply. For specimens that have different ply thicknesses, this criterion cannot predict crack initiation and propagation properly. Furthermore, the main weakness of this criteria is that it does not fit with experimental results, e.g. Hinton and Soden [36]. Thus strength-based criteria can only be used to predict damage initiation and not for failure propagation such as delamination between plies. Strength-based criteria consist of many models that have been derived to predict the onset of damage. First ply failure has been used to predict microcracking which assumed that microcracks happen when the strain in any ply reaches the failure strain within that ply. Other approximated models did not agree with experimental results as they neglect different stresses. Highsmith and Reifsnider [77] neglected the stress variation through the ply thickness to construct a shear lag model. This "ply discount model" neglects the transverse stiffness of the cracked plies. Hashin [37] and Niran [38] developed a model to overcome all previous limitations to account for stress transfer within a cracked laminate. This model has generally been shown to give better predictions than other models. Many other models have been derived in the last five decades for strength and failure analysis such as; Hashin, Hoffman, Yamada-sun, Puck, Tsai-Hill, Chang-Chang, and Tsai-Wu. Hashin, Puck, and Tsai-Wu [27, 39-42]are widely used for the separate type of damage in composite materials.

Many of these models have been used in commercial FE analysis such as ABAQUS, ANSYS, and Ls-Dyna to find the failure of the composite structure, e.g.

J. Phou et.al [80] used the Chang-Chang model with the Brewer and Lagace delamination criteria to predict damage of T300/914 unidirectional CFRP under impact load.

Many failure criteria of plies have been suggested. The earliest and simplest criteria are the maximum stress and maximum strain criteria.

1.1.1.1 Maximum stress criterion

Maximum stress criterion was proposed by Erdogan et al. [43]. It is assumed that failure occurs when the applied load in any direction is equal to or exceeds the strength of the composite laminate in this direction. The condition of failure according this criterion is:

Under tension

$$\begin{aligned} \sigma_1 &\geq X_t \\ \sigma_2 &\geq Y_t \\ |\tau_{12}| &\geq S \end{aligned} \tag{4.2}$$

Under compression

$$\begin{aligned} |\sigma_1| &\geq X_c \\ |\sigma_2| &\geq Y_c \end{aligned} \tag{4.3}$$

where X_T, X_C, Y_T, Y_C, and S are the tensile and compressive strength along the x-axis and y-axis shear strength respectively. A similar criterion exists using strain rather than stress. Due to their simplicity, both maximum stress and maximum strain criteria are mostly used in practice. However, the failure prediction results by these criteria are not reliable and differ from experimental results due to their simplicity and the lack of consideration of the interaction between failure modes. Thus, some modifications of these failure criteria are required for composite laminates

1.1.1.2 Tsai-Hill Failure criterion

The Von Mises criterion for isotropic plasticity in metals had been extended and used for the composite materials by Hill [44]. He assumed that the plastic deformation was dominated by incompressibility, and that both tensile and compressive strength are equal (X_t = Xc =X and Y_t = Yc = Y). This criterion can be expressed for the orthotropic unidirectional plate as:

$$\frac{\sigma_1^2}{X^2}+\frac{\sigma_1\sigma_2}{X^2}+\frac{\sigma_2^2}{Y^2}+\frac{\tau_{12}^2}{S_{12}^2}=1 \quad (4.4)$$

The laminate will fail if the left-hand side is equal one. The weakness of this criteria is that the failure criteria in compression is the same as that in tension, although the processes involve different mechanisms.

1.1.1.3 Hoffman Failure criterion

Another modification had been made on the von Mises criterion by assuming that the tensile and compressive strength are not equal. This modification was made by Hofman [40] and his criterion can be expressed as:

$$\frac{\sigma_1^2-\sigma_1\sigma_2}{X_tX_c}+\frac{\sigma_2^2}{Y_tY_c}+\frac{X_\mathrm{c}-X_\mathrm{t}}{X_tX_c}\sigma_1+\frac{Y_\mathrm{c}-Y_\mathrm{t}}{Y_tY_c}\sigma_2+\frac{\tau_{12}^2}{S_{12}^2}=1 \quad (4.5)$$

The laminate will fail if the left hand side equal right hand side.

1.1.1.4 Tsai-Wu Failure criterion

For anisotropic materials, Tsai and Wu [41] proposed a failure criterion based on the following equation:

$$\mathrm{F}_i\sigma_i+\mathrm{F}_{ij}\sigma_i\sigma_j+\mathrm{F}_{ijk}\sigma_i\sigma_j\sigma_k+\cdots=1$$

where i, j, k =1, 2, 6, …., and F_i, F_{ij}, and F_{ijk} are the corresponding material strength parameters. The laminate will fail if the left hand side is greater than or equal to one.Due to symmetry, the shear strength parameters should be zero. This gives

$$F_6 = F_{16} = F_{26} = 0$$

Equation (4.5) can then be simplified to

$$\mathrm{F}_1\sigma_1 + \mathrm{F}_2\sigma_2 + \mathrm{F}_{11}\sigma_1^2 + \mathrm{F}_{22}\sigma_2^2 + \mathrm{F}_{66}\sigma_6^2 + 2\mathrm{F}_{12}\sigma_1\sigma_2 = 1 \qquad (4.6)$$

Supposing purely bi-axial in-plane loading

$$\sigma_1 = \sigma_2 = \sigma_0 \ \text{and}\ \sigma_6 = 0$$

The strength parameters are expressed as:

$$\mathrm{F}_1 = \frac{1}{X_t} - \frac{1}{X_c} \qquad \mathrm{F}_2 = \frac{1}{Y_t} - \frac{1}{Y_c} \qquad (4.7)$$

$$\mathrm{F}_{11} = \frac{1}{X_t X_c} \quad \mathrm{F}_{22} = \frac{1}{Y_t Y_c} \quad \mathrm{F}_{66} = \frac{1}{S^2} \qquad (4.8)$$

$$\mathrm{F}_{11} = \frac{1}{2\sigma_0^2}\left[1 - \left(\frac{1}{X_t} - \frac{1}{X_c} + \frac{1}{Y_t} - \frac{1}{Y_c}\right)\sigma_0 - \left(\frac{1}{X_t X_c} + \frac{1}{Y_t Y_c}\right)\sigma_0^2\right] \qquad (4.9)$$

This criterion had been validated with experimental test by Pipes and Cole [45] and they had a good agreement when they applied it on boron/epoxy composites.

1.1.1.5 Hashin's Failure criterion

Hashin [39] proposed a criterion for unidirectional composite laminates for different failure modes and it can be expressed as:

Tensile fibre failure for $\sigma_1 \geq 0$

$$\left(\frac{\sigma_1}{X_t}\right)^2 + \frac{\tau_{12}^2 + \tau_{13}^2}{S_{12}^2} = 1 \tag{4.10}$$

Compressive fibre failure for $\sigma_1 < 0$

$$\left(\frac{\sigma_1}{X_c}\right)^2 = 1 \tag{4.11}$$

Tensile matrix failure for $\sigma_2 + \sigma_3 \geq 0$

$$\left(\frac{\sigma_2 + \sigma_3}{Y_t^2}\right)^2 + \frac{\tau_{23}^2 + \sigma_2\sigma_3}{S_{23}^2} + \frac{\tau_{12}^2 + \tau_{13}^2}{S_{12}^2} = 1 \tag{4.12}$$

Compressive matrix failure for $\sigma_2 + \sigma_3 < 0$

$$\left[\left(\frac{Y_c}{2S_{23}}\right)\right] - \left(\frac{\sigma_2 + \sigma_3}{Y_c^2}\right) + \left(\frac{(\sigma_2 + \sigma_3)^2}{4S_{23}^2}\right) + \frac{\tau_{23}^2 - \sigma_2\sigma_3}{S_{23}^2} + \frac{\tau_{12}^2 + \tau_{13}^2}{S_{12}^2} = 1 \tag{4.13}$$

Hashin criterion has been widely used in many FEM software. In this thesis, this criterion is used to define all four of these failure modes.

1.1.1.6 Chang-Chang Failure criterion

This criterion which proposed by Chang-Chang [42] is capable of predicting damage in a laminate with arbitrary fibre orientation and it is based on a progressive damage model. It can be expressed as

Tensile fibre failure for $\sigma_1 \geq 0$

$$e_f^2 = \left(\frac{\sigma_1}{X_t}\right)^2 + \left(\frac{\tau_{12}}{S_{12}}\right)^2 = 1 \tag{4.14}$$

Compressive fibre failure for $\sigma_1 < 0$

$$e_c^2 = \left(\frac{\sigma_1}{X_c}\right)^2 = 1 \qquad (4.15)$$

Tensile matrix failure for $\sigma_2 \geq 0$

$$e_m^2 = \left(\frac{\sigma_2}{Y_t^2}\right)^2 + \left(\frac{\tau_{12}}{S_{12}}\right)^2 = 1 \qquad (4.16)$$

Compressive matrix failure for $\sigma_2 + \sigma_3 < 0$

$$e_d^2 = \left(\frac{\sigma_2}{2S_{12}}\right)^2 + \left(\frac{\tau_{12}}{S_{12}}\right)^2 + \left[\left(\left(\frac{Y_c}{2S_{12}}\right)^2\right) - 1\right]\frac{\sigma_2}{Y_c} = 1 \qquad (4.17)$$

where e_f, e_c, e_m, and e_d are the variables of fibre and matrix in tension and compression respectively.

4.6 Propagation of intra-ply damage

Strength-based approaches are generally used to predict different types of damage initiation within composite structures but they alone cannot simulate the progression of damage through the body to final failure. Kachanov [46] proposed a simple way to predict the ultimate damage of such types of structures known as continuum damage mechanics (CDM).

4.6.1 Damage mechanics approach

This approach incorporates the effect of micro-voids and cracks on the stiffness and damage evolution within a specific material and allows the simulation of damage growth and load redistribution. Talreja and Singh [2] defined damage mechanics as a study of microstructural events based on the mechanical analysis of solids that changes its material response under the action of external loading. This approach uses a phenomenological damage variable D in a material constitutive model to represent the two-stage damage process: initiation and propagation. A single damage factor D can be used to capture all types of damage within the composite, or multiple damage fields can be used to represent each separate damage type. For a uniaxial loaded isotropic homogeneous structure the damage factor is incorporated into the standard stress and strain relationship as follows:

$$\sigma = (1 - D)E\epsilon \tag{4.18}$$

Where D is scalar damage variable $0 \leq D \leq 1$ (D = 0 undamaged structure, D=1 full damaged structure), σ applied stress, ε strain, and E is the material stiffness matrix. In the damage mechanics approach, the mechanical properties of the composite structure will decrease gradually according to equation (4.18) After damage initiation within a ply, the load resistance of this structure will decrease because just the undamaged part will carry this load (which is generally the fibres). Thus, the stress within the undamaged part will increase to reach the ultimate strength. Damage will then progress through the structure until complete failure occurs when the applied load can no longer be transmitted through the structure.

Many researchers have developed various continuum damage models, e.g. [2], [47], and [48]. In their models, many relationships between the damage factors, conjugate forces and internal stress/strain have been proposed to predict stiffness degradation and the progressive damage in composite structures based on many damage modes.

CDM–based modelling has been used in different applications in the analysis of damage and fracture of different composite types, both woven composites and unidirectional composites. Many researchers [49] [50] [28] have used a user-defined material routine (UMAT) within Abaqus to validate experimental results to predict failure of CFRP based on CDM and non-local ply scale criteria.

However, recent studies [51, 52] showed that the models that are based on CDM are insufficient to capture the interaction between plies because. These models are incapable to represent complex matrix failure behaviour because of homogenization that is inherent in continuum models, irrespective of the applied failure criteria and material degradation laws. Such process leads to the loss of key information on multiple-mode damage coupling at the macroscopic scale and, thus, may result in an inaccurate prediction of a crack path. To overcome this problem, an approach based on cohesive zone models (CZMs) has been adapted to model both types of damage e.g. intra-ply and inter-ply damage.

4.7 Inter-ply failure

The second type of failure is the intra-ply failure, or delamination, which occurs between plies and usually happens after the initiation of damage by intra-ply failure. This type of failure depends strongly on matrix cracking within plies. When cracks in two adjacent plies of different orientation propagate and join together, the interlaminar shear stress increases significantly and causes the delamination between these plies [28]. Delamination is common in impact loads and the position of the delamination depends on the velocity of the impactor and the thickness of the laminates. Delamination can reduce the strength and the stiffness of the composite structure significantly and could cause up to a 60% reduction in the composite structure strength [53]. On the other hand, it can cause stress relief of the structure and this may reduce the possibility of the final failure. For all these reasons, it is essential to analyse and create an accurate and reliable model to predict all types of damage and the connection between them to know the performance of composite structures and improve the final design [54].

One of the most common failures in composite materials under low-velocity impact is delamination, which correlates strongly with matrix cracking. De Moura et al. [55] have conducted an experimental and theoretical work to show the relation between matrix cracking and delamination. Their work was done on a carbon fibre-epoxy matrix laminate and they found that the matrix cracking happened first at the outermost layers of the laminate and that delamination occurred subsequently. These two types of failure happen between different oriented layers and form two oval shapes with their major axis coincident with the direction of the fibres of the lower ply. In composite materials, the presence of damage within the material causes a reduction in the strength. Amaro et al. [35] conducted a study to show the effect of delamination on the strength of a carbon-epoxy composite material in static bending tests. They used a 100 mm length by 2.28 mm thickness (12 plies of 0.19 mm thickness) composite simply supported beam and they introduced Teflon layers (50mm length and 0.04mm thickness) between different plies in the samples to simulate the initial presence of delamination cracks. The result showed that the presence of the delamination cracks reduces the strength of the composite by up to 25% depending on the position of the initial crack. The results for different cases are shown in Figure 4.6.

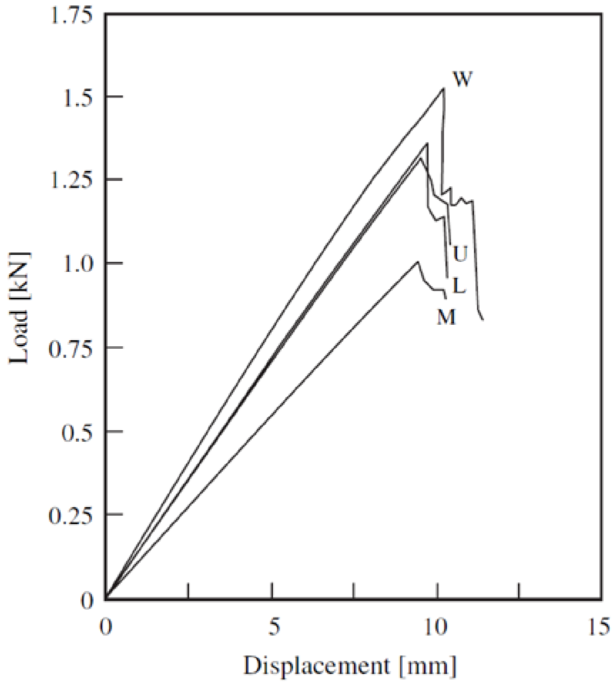

Figure 4.6: Load-displacement curves for laminates with and without delamination. (W, without delamination (defects); M, delamination at half thickness; L, delamination at 0.57 mm from the bottom; U, delamination at 1.71 mm from the bottom [45].

4.8 Initiation of inter-ply damage

In general, delamination occurs for a load case in Figure 4.5 when the following condition is satisfied

$$\left(\frac{\sigma_{33}}{Z_T}\right)^2 + \left(\frac{\sigma_{23}}{S_{23}}\right)^2 + \left(\frac{\sigma_{31}}{S_{31}}\right)^2 \geq 1 \qquad (4.19)$$

where Z_T is the tensile strength in the thickness direction, S_{23} is the shear strength for delamination in the transverse and thickness direction, and S_{31} is the shear strength in the through-thickness and fibre direction [56], as shown in Figure 4.6.

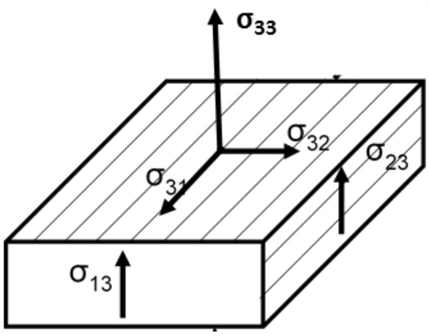

Figure 4.7: Stresses inducing delamination [35].

This results suggests that it is necessary to simulate the nucleation and propagation of individual delamination cracks to accurately predict the failure of a composite laminate.

4.8.1 Fracture mechanics-based approach

Fracture mechanics can generally be used to predict (microscopic) matrix cracking and (mesoscopic) delamination between plies. This approach is used to study the effect of matrix cracking and delamination on the strength of composite structures. The main objective of the fracture mechanics approach is to predict the onset of crack growth within composite structures that contain a flaw of a given size. To calculate the critical load for a cracked composite, the plastic zone at the crack tip is assumed small compared with the length of that crack, i.e. the material is brittle or not very ductile. In fracture mechanics theory, the macroscopic growth of a defect is controlled by the rate of strain energy released in propagation. This term is known as the fracture toughness of a material or an interface [32]. In any material, the loading type consists of three components: Mode I, Mode II, and Mode III loading, as shown in Figure 4.8. Mode I refers to the tensile opening or peeling of the crack surface, Mode II refers to sliding, and Mode III refers to tearing. Using fracture mechanics to predict delamination between plies in a composite structure requires a highly dense mesh, or a computational re-mesh technique should be used, to obtain good results due to its sensitivity to the stress intensity at the crack tip which is a complex function of the local geometry. A further prediction of fracture properties requires special techniques such as J-integral but this approach cannot be used to calculate the energy released in 3D since it can be used only in plane stress. However, many approaches such as virtual crack closure technique (VCCT) based on fracture mechanics have been used with FE codes such as Abaqus for crack propagation analysis. VCCT was used by Rybicki and Kanninen based on Irwins [57] crack tip energy analysis for linear elastic materials. The assumption of VCCT is the energy consumed to open a crack tip is the same amount of energy to close it. This technique was used in Mode II and mixed mode and in 2D continuum and 3D solid without any highly dense mesh. Pereira et al. used the VCCT in Abaqus using 3D 8-node brick C3D8R elements to calculate the energy released in Mode I double cantilever beam (DCB) for woven glass/epoxy multidirectional laminates. Shindo et al. [58] used the same analysis for the same model but for Mode II. The main disadvantage of VCCT technique is that it can only be used with predefined cracks.

An alternative approach to overcome this issue is to use a cohesive-zone and cohesive surface to model crack propagation in FE models such as Abaqus. In this study, cohesive surface and cohesive layer have been used to predict the area of delamination between all plies.

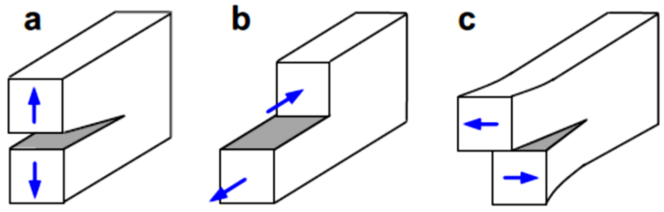

Figure 4.8: Crack growth modes (a) Peeling,(b) Shearing, and (c) Tearing [59].

4.8.2 Fracture mechanics model for initiation of delamination

A cohesive law that is based on fracture mechanics is generally mode dependent and should be defined for both modes; i.e. normal and shear. Mixed mode loading dominates in most composite applications. In this mode, crack faces open and slide relative to each other simultaneously. For this reason, a general formulation that predicts initiation and propagation of mixed modes is required. In bending loading, a mixed-mode traction separation law is used as shown in Figure 4.9

Many approaches based on strength are developed in the initiation stage, such as maximum normal stress and quadratic stress criteria. Cui et al [60], Camanho and Davila [61] found that using quadratic stress criteria gives more reliable result rather than the maximum normal stress criteria because the latter gives an interaction between interlaminar stress components in delamination prediction. The form of the normal quadratic stress criteria is:

$$\left(\frac{\langle\sigma_I\rangle}{\sigma_{I0}}\right)^2 + \left(\frac{\langle\sigma_{II}\rangle}{\sigma_{II0}}\right)^2 + \left(\frac{\langle\sigma_{III}\rangle}{\sigma_{III0}}\right)^2 = 1 \tag{4.20}$$

where $\sigma_{I0}, \sigma_{II0}, and\ \sigma_{III0}$ are the cohesive strength in mode I, mode II, and mode III respectively. The Macauly bracket < > shows that the compressive stress has no effect on damage initiation.

In the propagation stage of delamination, fracture toughness and energy released rate are used instead of stresses. There are two laws of fracture energy which are generally used at this stage. These are a power law, which was proposed by Reeder [62], and the Benzeggagh and Kenane (B-K) law [57]. In this study, B-K law has been used to predict delamination because Camanho and Davila [61] recommended it for thermoplastic composites. The B-K law is given as:

$$G_c = G_{Ic} + (G_{IIc} - G_{Ic}) \left[\frac{G_S}{G_T}\right]^{\eta} \quad (4.21)$$

where G_T is the work done by the interfacial traction; G_S/G_T is the fraction of cohesive energy dissipated by shear traction; G_S is the work done by the shear components of interface traction; G_{IC}, G_{IIC} is the critical energy released in Mode I and Mode II respectively, and η the material mode-mixity which can be found experimentally. To find the properties of the cohesive layer between plies in composite materials, a specific test is conducted to find them. A double cantilever beam (DCB) test is used to find G_{IC} and an end notched flexure (ENF) test is used to find G_{IIC}. Mixed-mode bending (MMB) test is used to find both.

4.8.3 Cohesive-zone models

Delamination of a composite structure is common, especially under impact load, and this type of damage can reduce the structure stiffness significantly. Modelling this type of damage requires simulating initiation and propagation of delamination. As discussed previously, strength-based criteria are generally used to simulate the initiation stage while fracture-mechanics approaches are used for propagation stage in FE methods such as J-integral, the virtual crack extension, and VCCT [63]. However, these approaches are often insufficient as they neglect material nonlinearity in most cases. Furthermore, these models require the exact position of a predefined crack and need a dense mesh. This makes the simulation expensive and impractical. Thus, to capture the interlaminar damage of composite structures, finite element analysis needs to be capable of modelling the strength and toughness of inter-ply damage.

A cohesive element technique at the interface of stacking plies has been employed to model the nonlinearity of both material and geometry. A model first proposed by [64] is the basic of the cohesive-zone element. This model assumed that a plastic zone is generated in front of the crack tip when the stress within a material reachs the yield stress of that material. A cohesive force at the molecular scale was first proposed by Barenblatt [65] to overcome the problem of equilibrium in elastic bodies with cracks. This approach depends on the definition of a traction-separation law.

4.9 Propagation of inter-ply damage

4.9.1 Traction-separation constitutive law for delamination growth

At the interface area between plies, the cohesive-zone model proposes the relationship between traction (stress) and separation (displacement) of any possible delamination crack. Many researchers have developed different types of models to define this relationship. Needleman [66] proposed an exponential law to describe all stages of debonding in metal matrices, i.e. initiation, propagation, and de-cohesion. The trapezoidal law was proposed by Tvergaard and Hutchinson [67] to predict growth resistance in elastoplastic materials and by Cui and Wisnom [68] for fully plastic materials. Damage in interface areas depends on the stiffness of this area, which decreases gradually as cracks propagate. The bi-linear law of the cohesive-zone is shown in Figure 4.9. The work required to complete all three stages of cohesive layer failure (initiation, propagation, and de-cohesion) is equal to the fracture toughness and the stiffness of the cohesive layer becomes zero [69]. Fracture toughness also can be defined as the area under the traction-separation curve. The bi-linear law for brittle materials, such as CFRP, can be defined simply as

$$\sigma = \begin{bmatrix} K\delta & \delta \leq \delta_0 \\ (1-d)K\delta & \delta_0 < \delta < \delta_f \\ 0 & \delta \geq \delta_f \end{bmatrix} \tag{4.22}$$

where

$$d = \frac{\delta_f(\delta - \delta_0)}{\delta(\delta_f - \delta_0)} \tag{4.23}$$

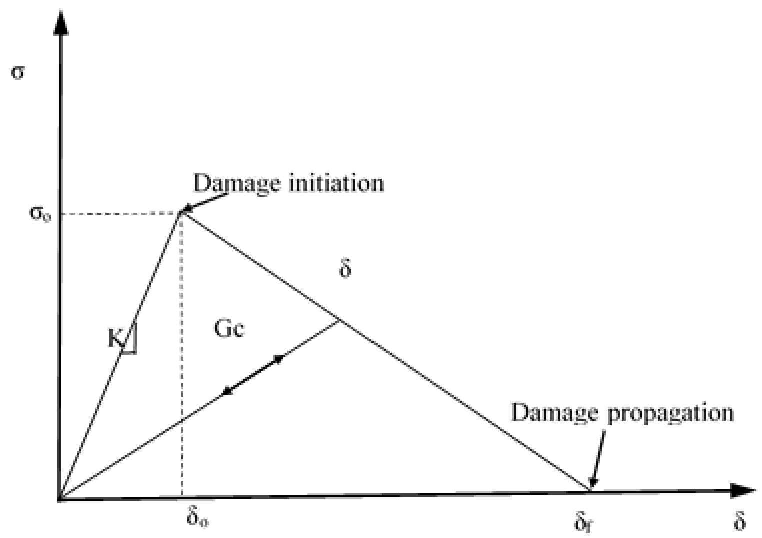

Figure 4.9: Bi-linear law of cohesive-zone.

The bi-linear law illustrated in Figure 4.9 consists of three stages. They are:

(a) Elastic part ($\delta \leq \delta_0$) when the traction relates to the separation linearly until the initiation point.

(b) Softening part($\delta_0 < \delta < \delta_f$) when the relationship between stress and separation is linked with the damage factor and the stiffness of the material. In this stage the stress within the material decreases until full separation between plies is reached.

(c) Decohesion part ($\delta \geq \delta_f$) the stress in this stage is zero as the separation is complete.

For mode I or mode II, the interfacial strength for the bilinear softening law can be found as

$$\sigma_o = K\delta_o \tag{4.24}$$

and the fracture toughness is

$$G_c = \frac{\sigma_{max}\delta_f}{2} \tag{4.25}$$

Using the cohesive zone technique in FE simulation, five properties of the interfacial behaviour are required. These are penalty stiffness, fracture toughness for mode I and II, G_{Ic} and G_{IIc}, B-K exponent (η) and normal tensile and shear strength, σ_{I0} and σ_{II0}, for static modelling. For dynamic modelling, there is another factor that is the effective density of the interface material [70].

4.9.2 Stiffness of cohesive-layer elements

A cohesive layer, or surface, between plies, is used to connect the adjacent plies and to transfer the load between them. The stiffness of this layer should be in a reasonable range. It should be high enough to avoid relative distortion between adjacent plies. However, this stiffness should not be too large to cause numerical problems such as spurious oscillation of the traction in the elements [71]. It is difficult to measure this stiffness experimentally. Thus, several authors have derived different methods to estimate the stiffness of the cohesive layer. Table 5 lists some typical values for different materials adopted by many researchers by trial and error methods [71].

Table 5: Initial interface stiffness K_0, mode I interface strength σ_I^o and mode II interface strength σ_{II}^o adopted by different authors for different materials.

Material	K_0 (x10^{15} N/m^3)	$\sigma_I^o (MPa)$	$\sigma_{II}^o (MPa)$
Aluminium	3 [72], 0.01 [73]	24–30,30	–
Hex-ply IM7/8552	1 [74]	60	90
AS4/PEEK	1 [69], 0.1 [75]	80	100
IM6/3501–6	1 [69], 0.1 [75]	61	68
T300/977–2	1 [76],[61]	60, 60	–, 60
DION 9102	1 [77]	50, 20	–
HTA6376/C	0.1 [76], 0.004 [78], 0.003 [79]	30, 45, 40	60, 40, 40
Glass fibre/epoxy	0.026 [80]	45	45
PEEK/APC2	1 [61]	80	100
XAS-913C	0.057 [81]	57	–
T700/QY9511	1 [82]	50	90
AS4/3501–6	0.0094 [83]	54	87
T300/914	0.3 [84]	75	–

Camanho et al. [61] used a graphite-epoxy material with a stiffness of 10^6 N/mm^3 and he had good, numerically stable results. Zou et al [85] assumed a relationship between the stiffness of the cohesive layer and the strength of this layer. He assumed a value of 10^4-10^7 times the strength of the interface per unit length. Turon et al. [86] derive an equation relating the elastic properties to this stiffness

$$K = \frac{\alpha E_3}{h}$$

where E_{33} is the elastic modulus of the composite though the thickness, h is the thickness of the connected plies, and α is a constant (which should typically be parameter much larger than 1).In this study, the value of α is 5.

It is not easy to perform the dynamic fracture characterization of composites. It is also difficult to manage and control high-speed delamination growth. However, measuring dynamic fracture toughness is important in prediction dynamic delamination propagation in composite laminates [87]. In dynamic delamination, it is known that Mode II is the dominant mode of delamination [88].

According to Wang and Vu-Khanh [89], the dynamic fracture behaviour of materials relates to the difference between the energy that is released when creating a crack per unit length (G) and the energy dissipated in creating the fracture surface (R). The crack growth speed increases as the difference increases as more energy is available to drive the growth of the crack. Thus, fracture stability depends strongly on the variations of the strain energy release rate and the materials resistance during growth. On the other hand, the strain rate at crack tip is very high and the material and the toughness is highly reduced under dynamic load because fracture resistance of polymers is highly sensitive to loading rate [90].

The effect of load rate on the fracture toughness is observed by many authors. Kumar and Kishore [91] found that the fracture of glass fibre epoxy laminate under dynamic load is 90-230 J/m^2 while it is 344-478 J/m^2 under static load.

All these works were carried out on unidirectional laminates. The properties of the cohesive layer are shown in Table 6.

Table 6: Properties of interface material.

Properties	Symbol	Units	Value [54, 71, 92]
Nominal stress mode I	t_n	MPa	60
Nominal stress mode II	t_s	MPa	90
Nominal stress mode III	t_t	MPa	90
Elastic modulus normal direction	K_{nn}	GPa	$1.2X10^3$
Elastic shear modulus	K_{ss}	GPa	$1.2X10^3$
Elastic shear modulus	K_{tt}	GPa	$1.2X10^3$
Fracture toughness I	G_I	N/m	250
Fracture toughness II	G_{II}	N/m	635
Fracture toughness III	G_{III}	N/m	732
Density [Assumed]	ρ	Kg/mm^3	$1.6x10^{-9}$

4.10 The finite element impactor model

In most cases in the drop test, a steel impactor has been used. Generally, the impactor is 20 times stiffer than typical carbon epoxy. Thus it can be modelled as a rigid body such that the deformations within the impactor are neglected [93]. Modelling the impactor in this way will save computational time. The motion of the impactor depends on the type of modelling i.e. static or dynamic. In this study, the impactor was given 1mm downward displacement in the static model and a velocity of 1.134m/s in the dynamic model.

In this study, three different sizes of hemispherical impactor 1, 2, and 4 mm diameter have been used with a mass of 350 g. 484 linear quadrilateral elements of type R3D4 has been used to mesh the impactor.

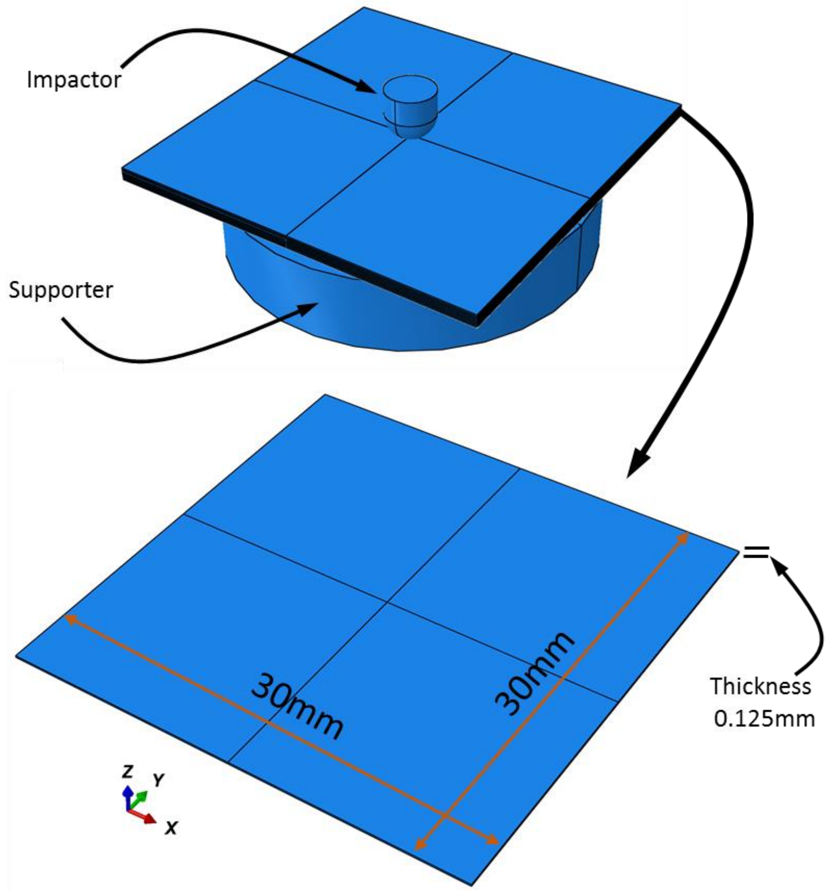

Figure 4.10: Finite element model of the laminate.

4.11 Type of elements and mesh sensitivity

One of the main advantages of using cohesive surfaces and cohesive elements is decreasing the number of elements required to simulate delamination between plies. Many researchers study the effect of mesh size on their results in different types of test on composite materials. Z.Zou et al. [85] used a 1mm mesh size with sample dimensions of (250x108x3 mm) and showed that increasing the mesh size to 2 mm will not have a significant effect on the delamination area of a graphite epoxy under static load. However, in order to obtain accurate results, the mesh should be sufficiently fine to capture the delamination area. Many assumptions have been used to estimate the length of the cohesive zone (l_{cz}). This can be defined as the distance between the potential crack tips to the point where the final failure is reached. According to Yang and Cox for delamination crack in slender bodies, the cohesive-zone length becomes a material and structural property. For constitutive models that prescribe non-zero tractions when the displacement jump is zero, the length of the cohesive-zone [94] the length of cohesive length is:

$$l_{cz} = \left(\frac{EG_c}{\sigma_0^2}\right)^{\frac{1}{4}} h^{\frac{3}{4}}$$

where E is the Young's modulus in the thickness direction, G_c is the critical energy release rate, σ_0 is the maximum interfacial strength, and h is the thickness of the ply. Touron et al. [86] derived an equation to estimate the number of elements required in the cohesive zone N_e as

$$N_e = \frac{l_{cz}}{l_e}$$

where l_e is mesh size.

In terms of the number of elements within the cohesive zone, there is a wide range of values that has been recommended in the literature, which has varied from two to more than ten elements in the cohesive zone [54]. Himayat [26] used different mesh sizes to predict the effect of element size in a fabric composite material and he found that using elements smaller than 0.1 mm will not change the results of the specimen with dimension 40mmx25mmx1mm . Perillo et al. [92] conducted a study on AS4/8552 (125x75x5.8mm) composite material under dynamic load. They examined the effect of mesh size on their results and they found that using a mesh smaller than 1mm will not change the global results (force and deflection with time). F. Caputo et al. [95] have used two techniques to model delamination in composite materials under impact load. They used coincident and not coincident meshes. The first needs a fine mesh and elements of the same dimension for the composite and the cohesive layer without tie constraints, while the latter requires a constraint between the cohesive layer and the ply [96]. Many researchers used different mesh size strategies to obtain a good result in a short time. They divided the sample into two parts; inner and outer part. Fine mesh has been used in the inner part that includes the contact region, and a coarse mesh has been used for the outer part. Wenzhi Wang et al. [97] used a 0.1 mm mesh in the inner part and 1mm for the rest. To capture the bending effect, he used two elements through the thickness. In this study, 0.5x0.5mm elements have been used for the composite laminate and cohesive layer and two elements through the thickness of each ply.

4.12 Contact interactions

The contact between the hemispherical nose of the impactor and top face of the CFRP must be modelled. This contact has been implemented using a surface-to-surface kinematic contact algorithm with finite sliding that is available in Abaqus 14 explicit. The contact property of this algorithm has tangential behaviour and was controlled by the Coulomb friction-based penalty contact enforcement method. The coefficient of friction between the impactor and the first ply was 0.3 as used in many articles [70, 98, 99]. The surface of the impactor and the top face of the laminate are referred to as the master and slave surfaces, as shown in Figure 4.11. An exploded view of the laminate is shown, with a non-existent gap between each ply.

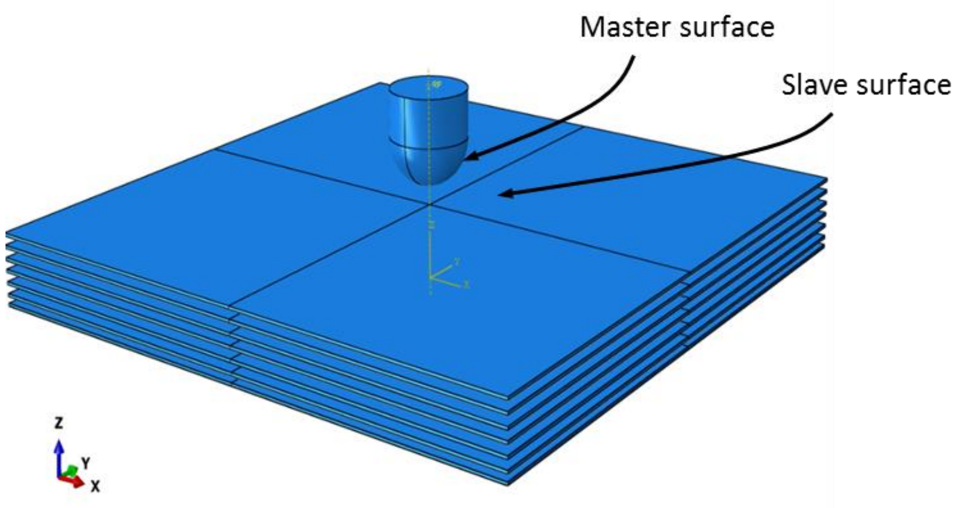

Figure 4.11: Interaction between laminate and impactor.

Chapter 5 Experimental procedure

5.1 Materials and specimen preparation

In this work, two types of specimens have been used. The first type is rectangular laminates with dimensions of 30 x 60 x 1 mm. This unidirectional (UD) material is the carbon/epoxy prepreg Cytec MTM44-1 resin/M55J fibre. This was supplied by the Multimatic CF Tech. the mechanical properties of this type of composite are shown in Table 4. The second type of laminate is manufactured in the Mechanics of Materials lab at Leicester University. The procedure of hand lay-up, vacuum bagging, and curing were followed in the fabrication of composite plates for the coupons tested in this thesis.

The UD material roll needs to be stored in a sealed moisture-proof bag in -18℃ and must be removed from the freezer 24 hours before use to defrost. The sealed moisture-proof bag can only be opened once the material temperature has risen to room temperature to protect it from condensation. The prepreg is 310 mm wide and covered with a non-stick protective sheet. After curing, each layer is around 0.125mm thick. A composite dedicated scissor and a paper trimmer were used to cut the prepreg into sheets with the required specifications (dimensions and fibre orientations) according to the patterns drawn on the protective sheet.

The lay-up of the laminate was carried out manually to stack the laminas in a predetermined sequence which is $[0, 45, 90, -45]_S$. The first lamina was laid on a clean smooth surface with the black prepreg face down, and then the white protective sheet was removed. The next layer, with the prepreg face down, was carefully laid onto the adhesive prepreg face of the first layer so that the fibres were aligned in the desired direction. A hand roller was used to remove the air bubbles out of the laminates.

The composite plate was placed on a clean Aluminium plate and a release film was placed between the composite laminate and the Aluminium plate to prevent the bonding between the laminates and the glass after curing. Another layer of release film was used to ensure the separation between the plate and the breather fabric after curing. Finally, the entire assembly of composite laminates and auxiliary materials was covered by the vacuum bag film. A high-temperature resistant double-sided tape was used to seal the vacuum bag on all the four edges of the rectangular Aluminium base plate.

Figure 5.1 shows a prepared vacuum bagging under vacuum overnight and ready for curing. The vacuum pressure was (-1.015 bar full vacuum). The vacuum quality was evaluated by checking whether the vacuum bag was holding pressure after turning off the vacuum pump. The composite plates were cured by the composite curing oven at the University of Leicester as shown in Figure 5.2

The curing operation consists of two stages. In the first stage, the oven was heated from room temperature to 130℃± 5℃ at an actual component heat-up rate of 1-2 ℃/min. The curing temperature was held for 120min ± 5min at 130℃ ± 5℃. The second stage was the same as the first except the temperature was at 180℃ ± 5℃. After the holding phase, the oven was cooled at an actual component cool-down rate of 2-5 ℃/min.

The fabrication quality of the composite plates was further checked by measuring the cured specimen thickness and using surface visual inspection. The mean individual lamina thickness was 0.125mm ± 0.015mm.

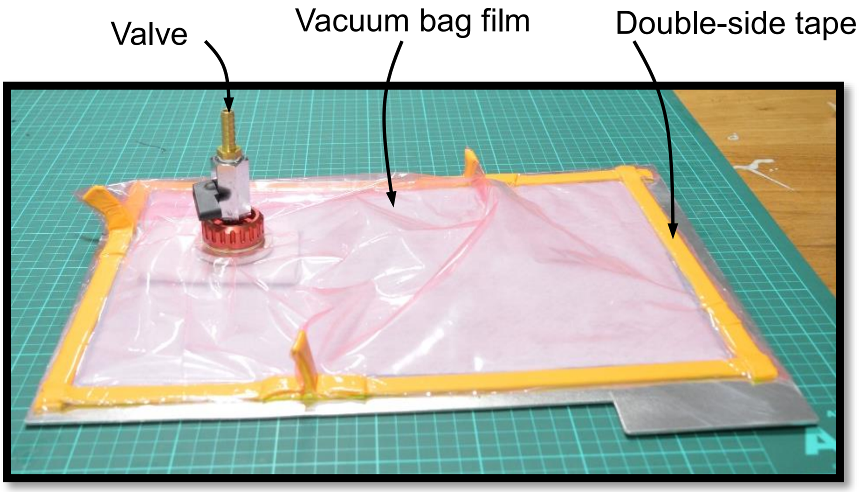

Figure 5.1: An assembly of composite plate and vacuum bagging ready for curing.

Figure 5.2: Composite curing oven.

5.2 Specimen preparation and test set-up

Following the fabrication procedure outlined in5.1, the qualified composite plates were further processed to obtain the final test coupons in accordance with different test standards.

The composite plates were cut into pieces with the required dimensions before curing to overcome the edge damage due to the cutting process. The specimen dimension was measured by a digital Vernier. The dimensional tolerance was about ±0.5mm.

5.2.1Quasi-static testing

Figure 5.3 shows the instrumented quasi-static test facility. The indenters were gripped by the Hounsfield 10kN universal test machine to apply an indentation force under displacement control of 1mm/min. The indenters were given a total displacement of 1mm. To make sure that the indenter was in the centre of the specimen, the specimens were aligned by using alignment tools as shown in Figure 5.4. At first, by using these tools, the tip of the indenter was placed in the centre of the holder to make sure that the tip of the indenter touched the tip of the sensor. The centre of the specimen was located by drawing two diagonal lines on both sides to ensure that the specimen was in the centre of the holder when the tip of the indenter touch the marked centre of the specimen on the top face and the tip of the sensor touched the marked centre of the bottom face.

The specimens with lay-up configuration $[0, 45, 90,-45]_s$ corresponding to the laminate thickness of 1mm were tested under three different indenters. To ensure that all specimens were tested under the same conditions, all the indenters were given the same total displacement of 1mm.

During the test, the applied force and the deflection of the back face contact point were automatically recorded by a data acquisition system which connected to the Hounsfield 10kN universal test machine. The accuracies of the force and the extension are ±0.5 % of the indicated values within the load and deflection ranges. The specimen rests freely on a round steel supporter with 25mm inner diameter. It contains a sensor in the middle to measure the deflection in the centre of the laminates back face. This eliminates the effect of indentation errors resulting from the penetration of the steel indenter at the point of contact with the upper face of the laminate. Three different rigid steel impactors with 1, 2 and 4 mm hemispherical head diameters have been used in this study, as shown in Figure 5.8. The load and deflection were electronically recorded during the test using Lab-view running on a PC connected to the displacement and force transducers. Calibration equations were used to convert these signals to force and displacement units.

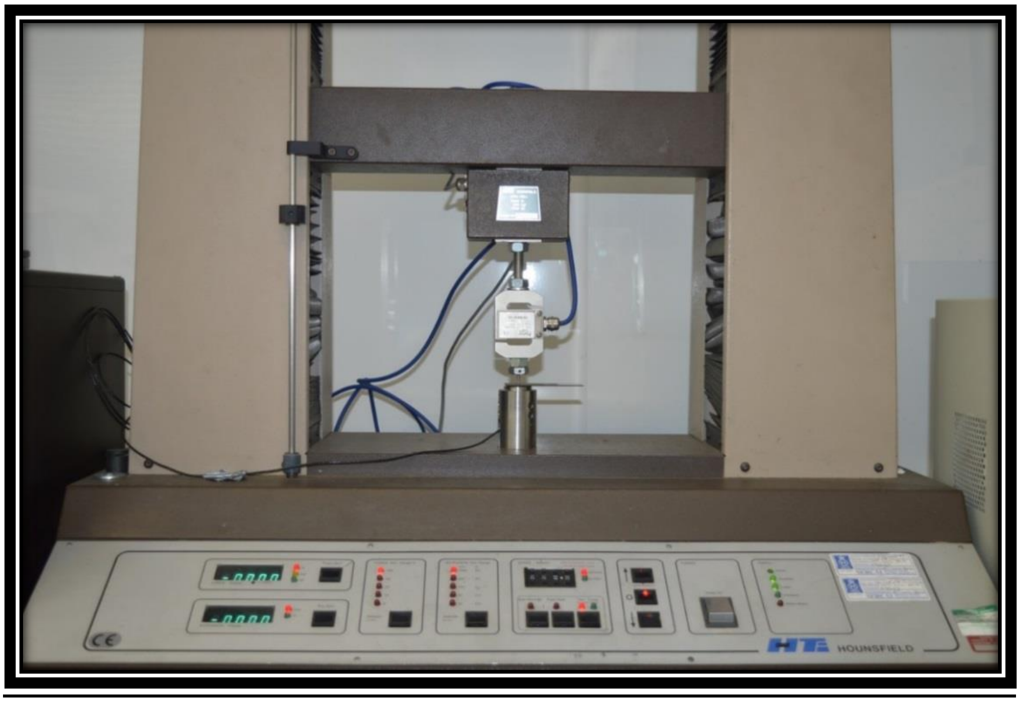

Figure 5.3: Instrumented quasi-static test facility.

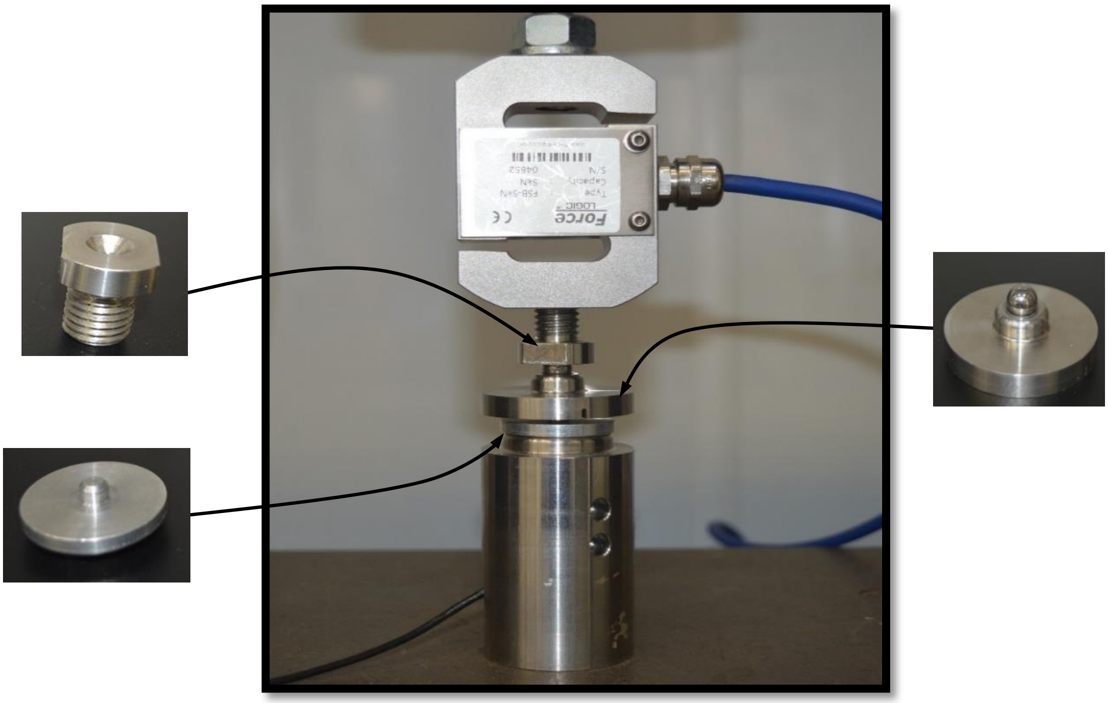

Figure 5.4: Adjustable tools.

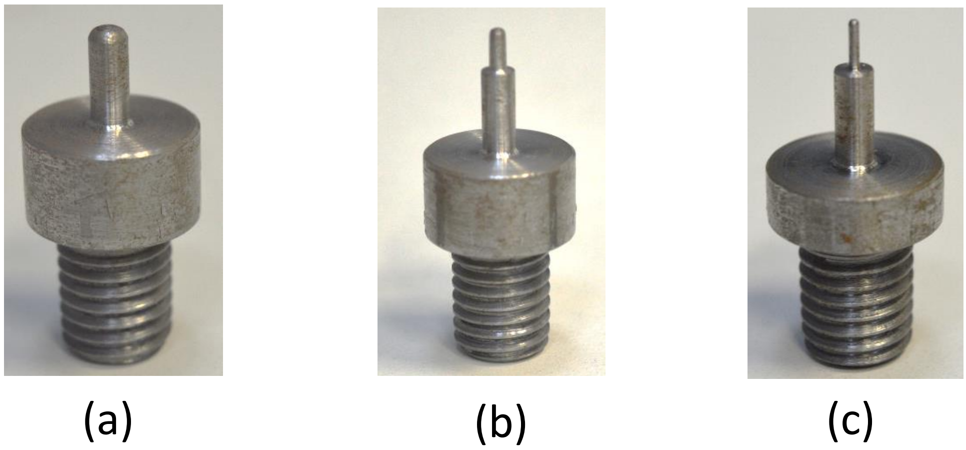

Figure 5.5: Three indenters with different diameters: (a) 4 mm (b) 2mm and (3) 1mm.

To validate the mechanical properties of the new composite laminates with standard laminates, a quasi-static test was carried out on both as shown in Figure 5.6.

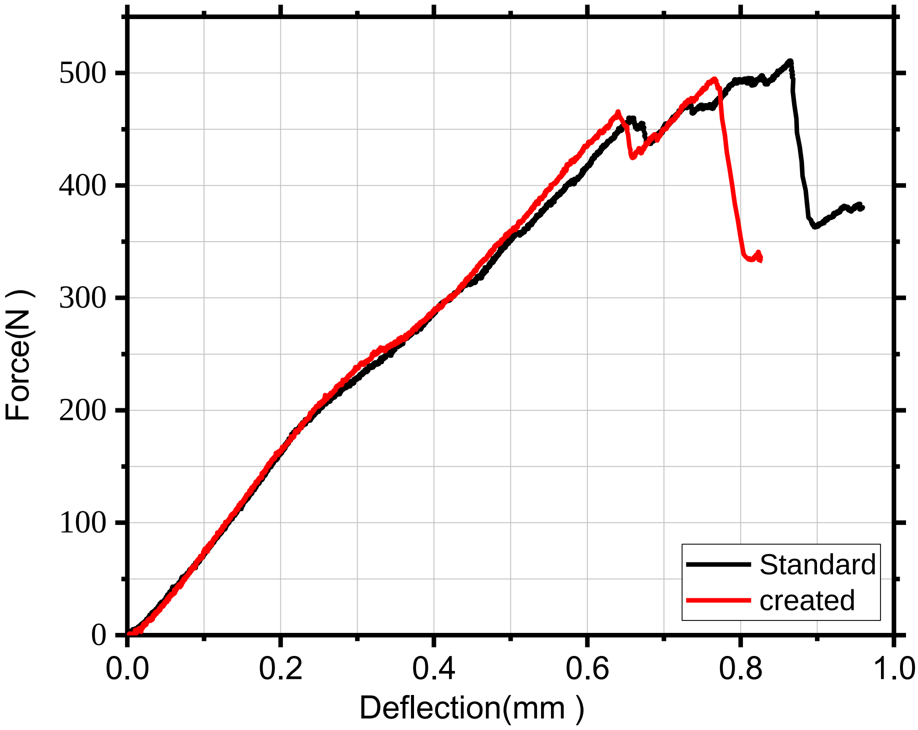

Figure 5.6: A comparison quasi-staic test for standard (outoclave) and manufactured (oven) laminates.

As shown in Figure 5.6, the same behaviour for the new laminate and the standard laminate is shown with small difference in the final or maximum force that the laminate can sustain.

5.3 Drop impact testing

In this part, instrumented drop weight tests were carried out for different indenter diameters with constant input energy.

A series of instrumented drop weight tests were conducted in accordance with ASTM D7136/D7136M-05 test standard in terms of the specimen preparation and test set-up. The test specimens were created by the carbon/epoxy composite system (Cytec MTM44-1 resin/M55J fibre) similar to those tested in the quasi-static tests. From the static part, the work done by the indenter of the static part until final failure which is fibre breakage (area under the force-displacement curve) has been calculated to be 0.225 J. This represents the work done by the indenter. The height of the impactor in the dynamic part was calculated depending on the amount of energy in the quasi-static part. The height was, therefore, 65.5mm for all tests. This value was calculated by using the following equation for the relative gravitational potential energy of the impactor:

$$E = mgh \tag{5.1}$$

where m is the mass of the projectile, g is the acceleration due to gravity, and h is the drop weight initial height above the specimen. To ensure the reliability of the test results, three specimens were prepared.

The impact test rig includes a drop tower, a projectile, a base to support the laminate, a laser displacement sensor, and a data acquisition system, as shown in Figure 5.7. The projectile includes two parts; a hemispherical impactor and the support frame. The total mass of the projectile is 350 Gm. The projectile can slide freely to impact the laminate along a guiding slot.

To measure the force induced between the impactor and the laminate, a 1053V4 dynamic force sensor is used with a range up to 2224.11 N. The sensitivity of the load cell, or the calibration factor to calculate the force depending on the voltage, is 10.78 mV/LbF or 2.4234 mV/N. The weight of the load cell is 28 grams and is included in the total drop mass. This dynamic load cell ensures a high accuracy with a resolution of 0.031 N.

The calculation of the deflection is done on the back side of the contact point to exclude the indentation and the penetration effect. The LK300 laser displacement sensor is used to calculate the deflection of the laminate. The sampling rate of this type of sensor is 20 μs which is sufficiently rapid to obtain a suitable number of data points within the expected impact time, which is expected to be less than 3ms. The accuracy of this type of sensor depends also on the diameter of the spot, which is 20 μm. The data is transferred from the laser displacement sensor to a data acquisition system connected to the sensor to give the deflection as a function of time, as shown in Figure 5.8.

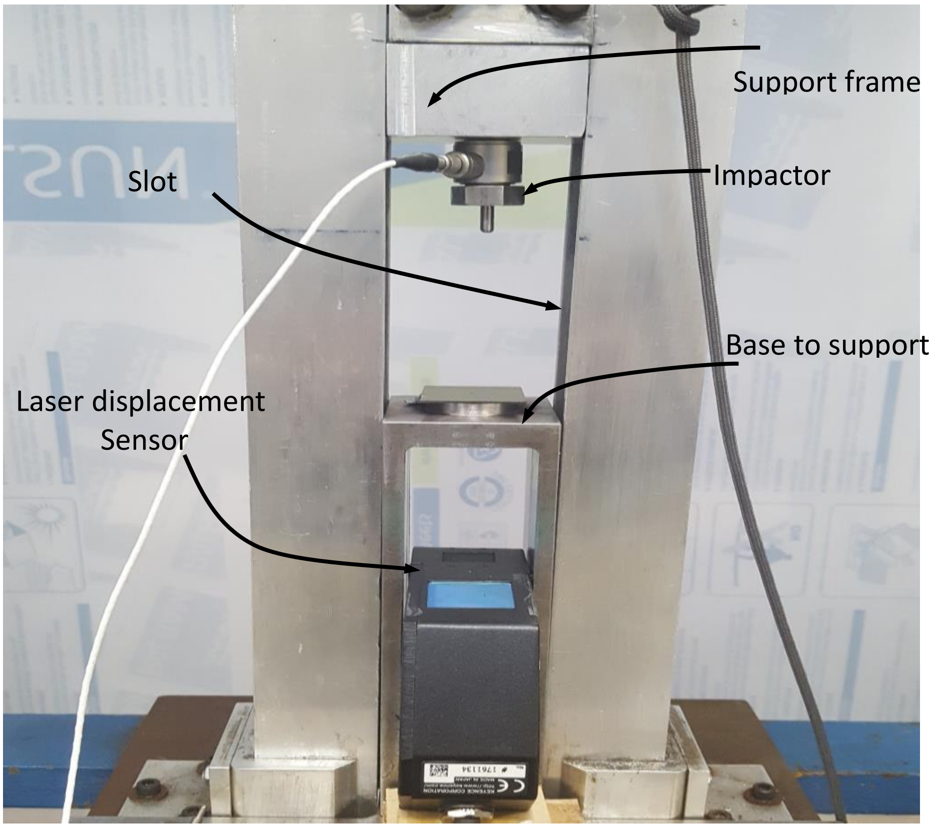

Figure 5.7: Drop-weight test rig.

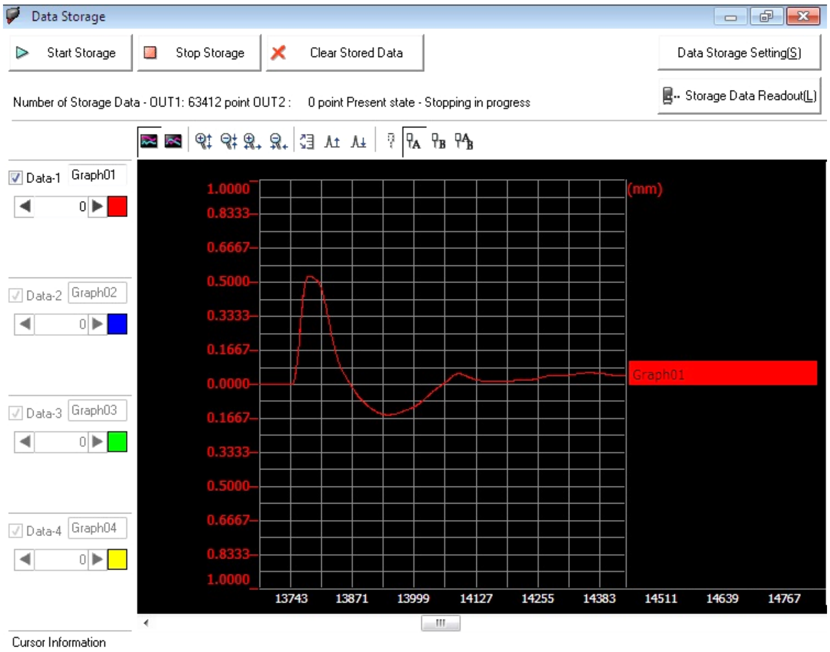

Figure 5.8: The shape of deflecting curve in data acquisition system.

5.4 Micro-CT analysis of damage

After the tests, scanning was performed using an X-Tek Computed Tomography (CT) electron beam machine. A schematic of the scan configuration is shown in Figure 5.8. Each specimen is connected to a stage and positioned between the gun and the detector. A cone of X-rays is released from the target and passes through the specimen to the detector, as shown in Figure 5.9. A transmission X-ray image was acquired from 1800 rotation views over 360º of rotation (0.2º rotation per step) for 3D construction.

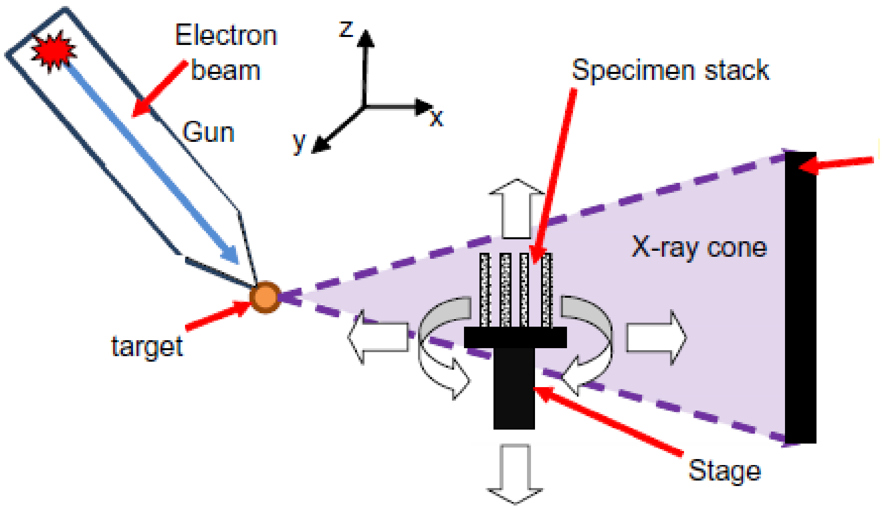

Figure 5.9: Schematic diagram of the CT scan.

CT reconstruction requires that all parts of the sample can be seen through at least 180 degrees. If the sample is rotated through only 180 degrees then the centre of the sample can be seen through 180 degrees but the point (1) in the sample will be seen through less than 180 degrees and point (2) in the sample will be seen through more than 180 degrees, as shown in Figure 5.10. This is because, as the sample moves from left to right, it's viewing angle increases by up to the cone angle (measuring angles clockwise) and as the sample moves from right to left, its viewing angle decreases by up to the cone angle. If the sample is rotating clockwise, the left part is seen through 180 degrees plus the cone angle, and the right part is seen through 180 degrees minus the cone angle (and vice-versa if anti-clockwise).

To form a stable image at a proper voltage, the X-ray source should be conditioned before using the CT scan. This step takes about 10-20 minutes at full voltage. As the number of frames increases, the time required for the scanning increases, but this reduces the noise in the image. In this work, the number of frames is 16 and the time required is about 6 hours.

There are many factors affecting the resolution of the specimen image, such as the distance between the specimen and the target, the type of target, exposure time, the type of filter and the amount of voltage and current supplied to the target etc. In this work, a Molybdenum target was used to generate the X-rays. The scanning voltage and current are 65 kV and 75µA respectively, with a 2 second exposure time without any filter.

The resolution of the image is obtained approximately as the width of the sample divided by the number of pixels horizontally across the detector. In this work, the pixel pitch of the detector is 127 microns and the magnification factor is 12. Thus the resolution of the image is 127 divided by 12 which is about 10 micron. Another factor which can affect the resolution of the scan is the amount of current and voltage that are used. A good rule is to make sure that the minimum grey level does not fall below 10000 pixels. This ensures that the scan will not be too bright, such that it hides many details within the image.

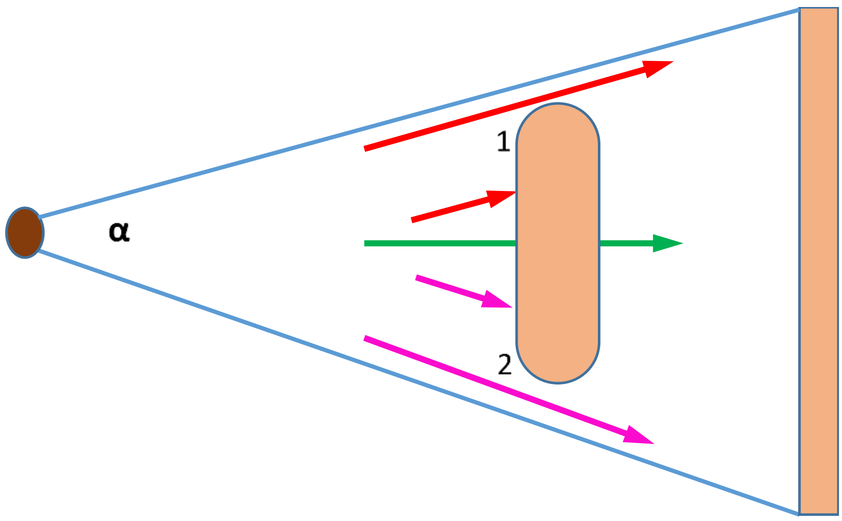

Figure 5.10: Schematic drawing of the rotation of specimen.

There are many factors to consider to obtain good setting of CT scan. These factors are the voltage and current for the X-ray set, sample position, type of filter, type of target, reducing noise, and the number of projections.

The voltage and current: Increasing the X-ray voltage increases the penetrating power of the X-rays which means that more X-rays pass through the specimen to hit the detector and the image becomes brighter. It is important to make sure that the voltage is high enough such that the image is noticeably brighter. A good rule of thumb is to make sure that the minimum grey level does not fall below 10000.

Increasing the X-ray current simply increases the number of X-rays passing through all parts of your specimen. If the voltage is not high enough to penetrate the longest path lengths of the specimen, then increasing only the current, but not the voltage, is not beneficial. If none of the X-rays have enough energy to get through the specimen then firing more of them at it will not help. However, if the voltage is already high enough, then increasing the current is a better option than increasing the voltage still further, as increasing the voltage may wash out low-density areas of the specimen.

Sample position: During a CT scan, the sample being scanned should not leave the sides of the imaging window at any rotation angle. If part of the sample leaves the sides of the imaging window, then information about that part will not be obtained from some rotation angles. However, since those parts pass in front and behind the region of a scan, they will affect the images of those parts. Having information from only some rotation angles and not all can lead to artifacts in the reconstructed volume.

If parts of the sample project up above the top of the image, or down below the bottom of the image, then this is not a problem, as they are then not visible at any rotation angle and so will not affect the reconstruction of other parts of the sample being scanned. So, to obtain the best resolution scan of your sample, the magnification axis should fill about 90% of the width of the image. The resolution is approximately the width of the sample divided by the number of pixels horizontally across the detector. So, if a sample with a maximum horizontal diagonal of 35mm and the detector has 1000 pixels across it, then the sample should span about 900 pixels and so the resolution will be just under 40μm.

Type of filter: Filters in front of the X-ray source are useful to reduce the contrast between the transmitted beam (where there is no sample) and the beam which has passed through a long path length of dense material. They reduce the brightness variations in the image so that the detector, which has a limited dynamic range, can still digitize all of the images without having areas of too bright white (saturated), or black (unpenetrated).

Reducing noise: Since the process of CT reconstruction enhances any noise that is in the projection images, it is imperative that the noise within individual images is as low as possible. There are several ways of doing this – increasing the X-ray current; increasing the exposure time on the camera; averaging more video frames.

Note that increasing the detector exposure time, and increasing the X-ray current, achieve the same aim. The former, however, increases the overall length of the CT scan, while the latter does not. There are times when the current should be kept low, such as when trying to achieve a very high resolution on a very small sample, but for larger samples increasing the current is fine. For high beam currents, a higher than normal filament demand current is needed (the filament must be hot enough to supply all the electrons you are requesting).

The number of projections: To avoid interpolation between edge voxels, the number of projection images should be great enough such that each angular increment moves on by no more than one voxel. This means that if a horizontal slice of N x N voxels, then projection images between $\pi.N/2$ and $\pi.N$ should be used, e.g. between 1.57 and 3.14 times N. So if the horizontal CT slices are to be 500x500 voxels then you should use at least 785 projection images. The vertical height of the volume does not influence the number of projections. Using less than this number of projections will lead to a certain amount of linear interpolation between voxels at the perimeter of the reconstruction volume during the reconstruction process. Using more than this number will not add more detail to the reconstruction, but will increase the signal to noise in the final volume, in the same way that increasing the exposure does. Note that N is not necessarily the number of pixels across the detector, but only across the sample.

5.5 VG studio procedure

When the CT scan process is finished, the 2D slices that have been created are transferred to VG Studio MAX, a program to create 3D images from the axial, right, and front slices. VG Studio Max was used to separate and align the resulting set of two-dimensional pictures to construct a 3D image of the sample. To obtain the best resolution pictures, the CT Flowchart for Inspection (given in the Appendix C) was followed.

5.6 Statistical analysis

To ensure that results were statistically significant, three specimens were tested for each loading e.g. (quasi-static and dynamic) type and indenter diameter e.g. (1, 2, and 4mm. The curves show the average result and the error bars indicate the variation between similar tests.

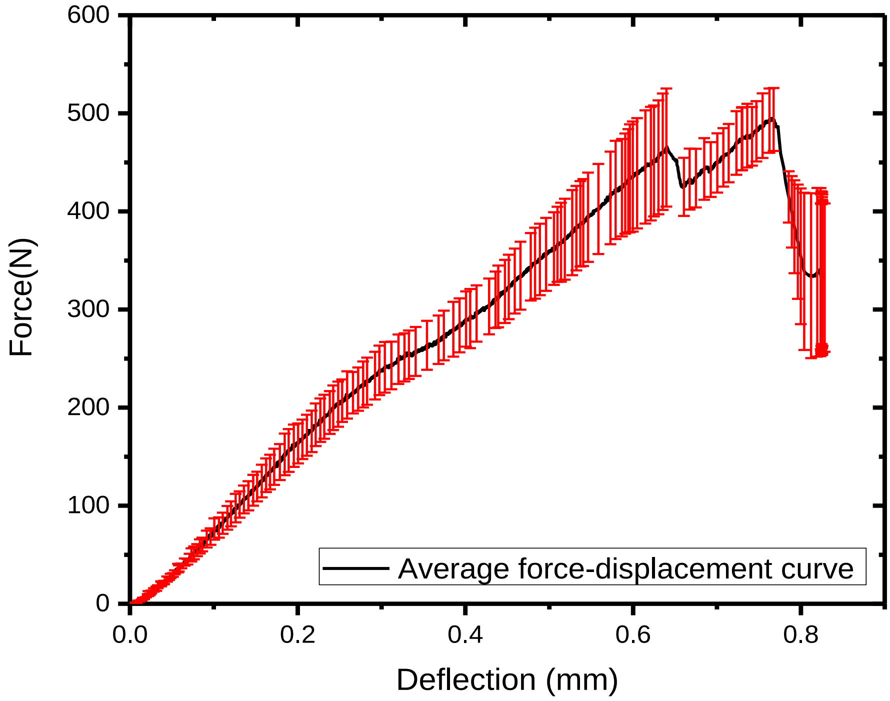

Figure 5.11: Statistical analysis of the force-deflection of 4mm daimeter indenter under quasi-static load.

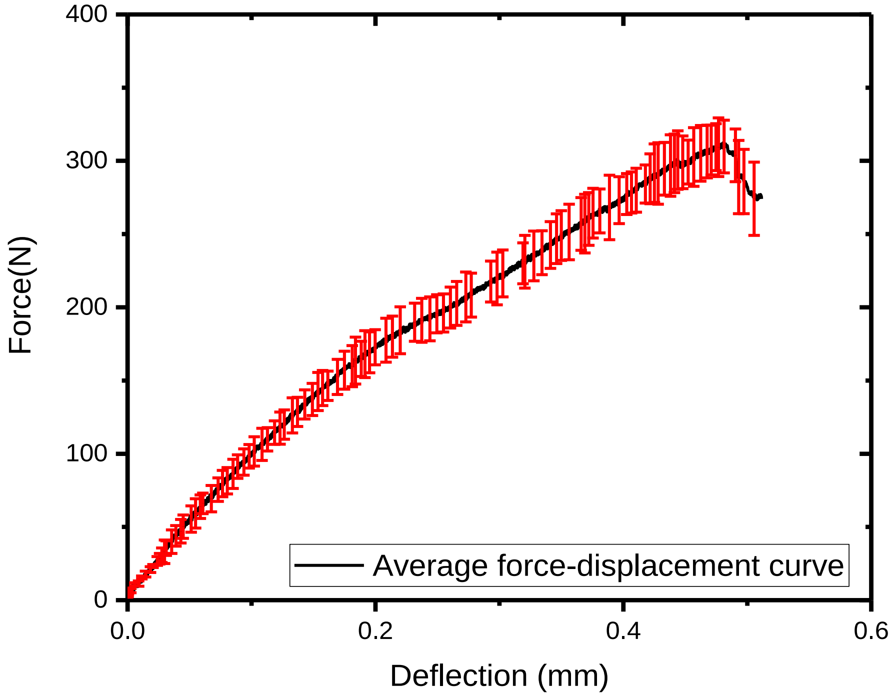

Figure 5.12: Statistical analysis of the force-deflection of 2mm daimeter indenter under quasi-static load.

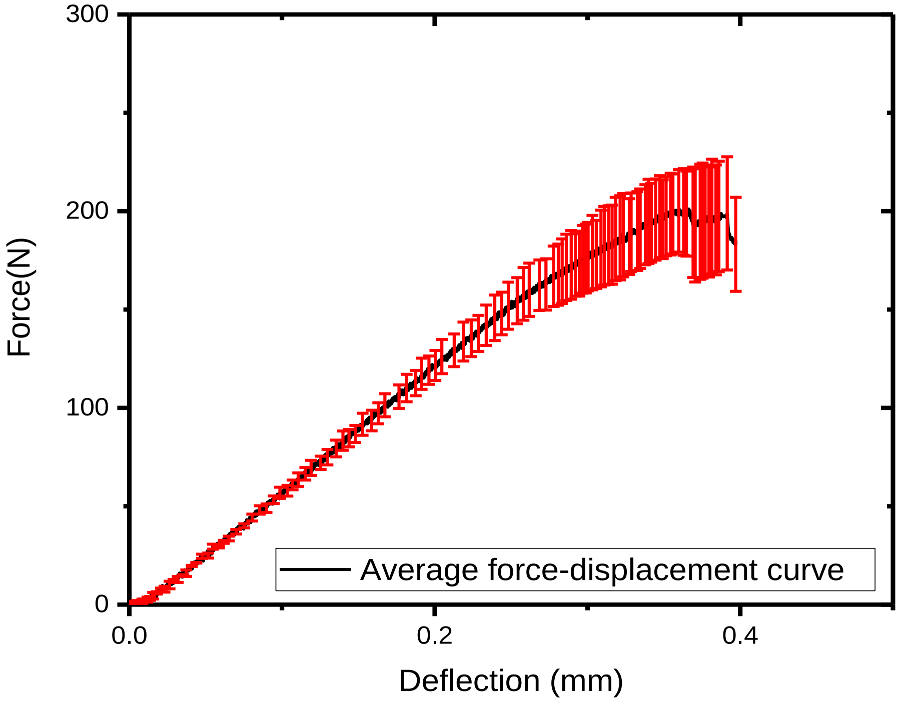

Figure 5.13 : Statistical analysis of the force-deflection of 1mm daimeter indenter under quasi-static load.

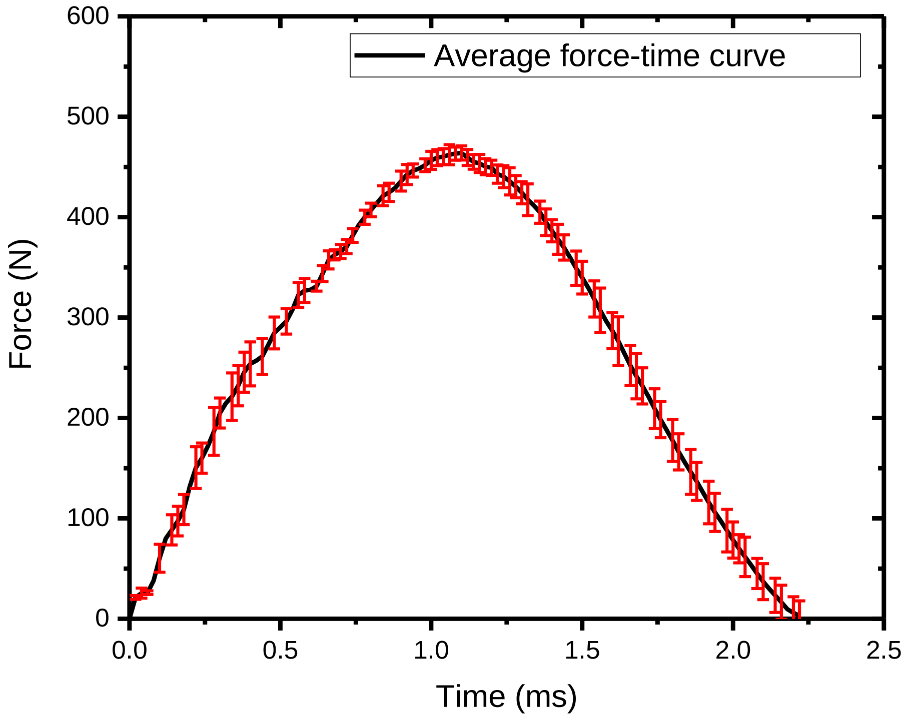

Figure 5.14: Statistical analysis of the force-deflection of 4mm daimeter indenter under drop impact load.

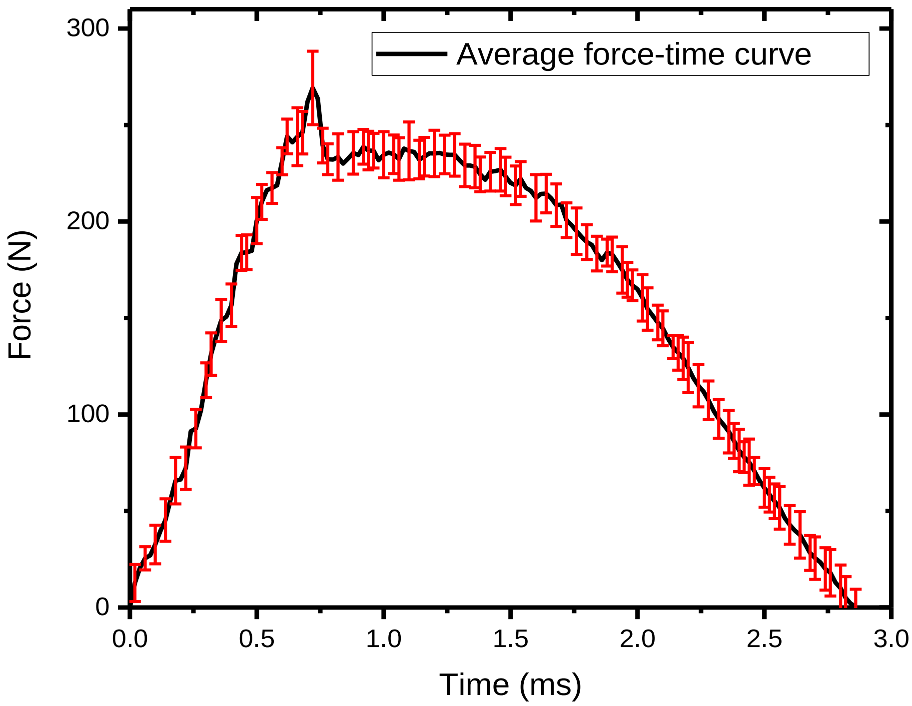

Figure 5.15: Statistical analysis of the force-deflection of 2mm daimeter indenter under drop impact load.

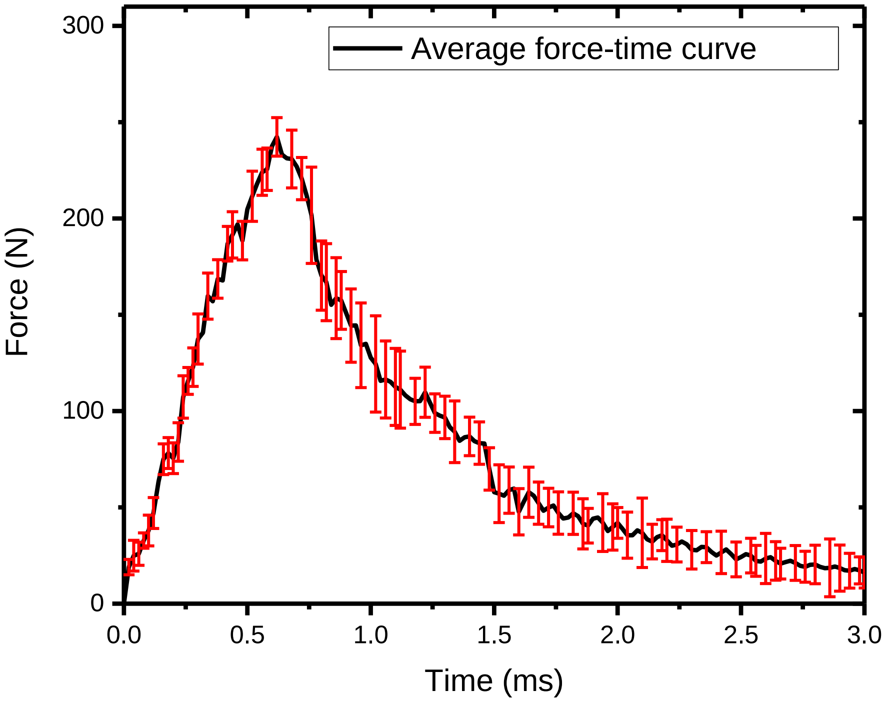

Figure 5.16: Statistical analysis of the force-deflection of 1mm daimeter indenter under drop impact load.

Chapter 6 Results for quasi-static loading

Results of experimental work and simulation of the quasi-static behaviour of laminated CFRP are presented in this chapter. The analytical work is compared with the experimental work in terms of the force-time curves, displacement-time curves, and the delamination areas. The main differences between each indenter diameter are investigated. The experimental work is presented first, followed by the modelling results. The two are then compared in the final sub-section. A comparison with the simulation predictions. The delamination area is calculated in the FE simulations based on the cohesive layer model depending on the damaged area of the cohesive layer which has stress exceed the strength of cohesive layer in each direction.

6.1 Experimental work

In this section, the effect of the indenter radius on the force-displacement curve is investigated. The size effect on the ultimate force that the laminate can sustain and the initiation of delamination force (known as the knee point force) are presented. The structure of the internal damage at the final failure load is also presented.

6.1.1 Force-displacement behaviour

The laminates are tested under the same displacement of 1mm for the three different indenter diameters (1, 2, and 4mm). The speed of applying the displacement was 1mm/min which is considered to be slow enough to represent a quasi-static loading case as the amount of kinetic energy is too small compared to the total energy or the work done during the process. The effect of the indenter diameter on the force-displacement curve is presented in Figure 6.1.

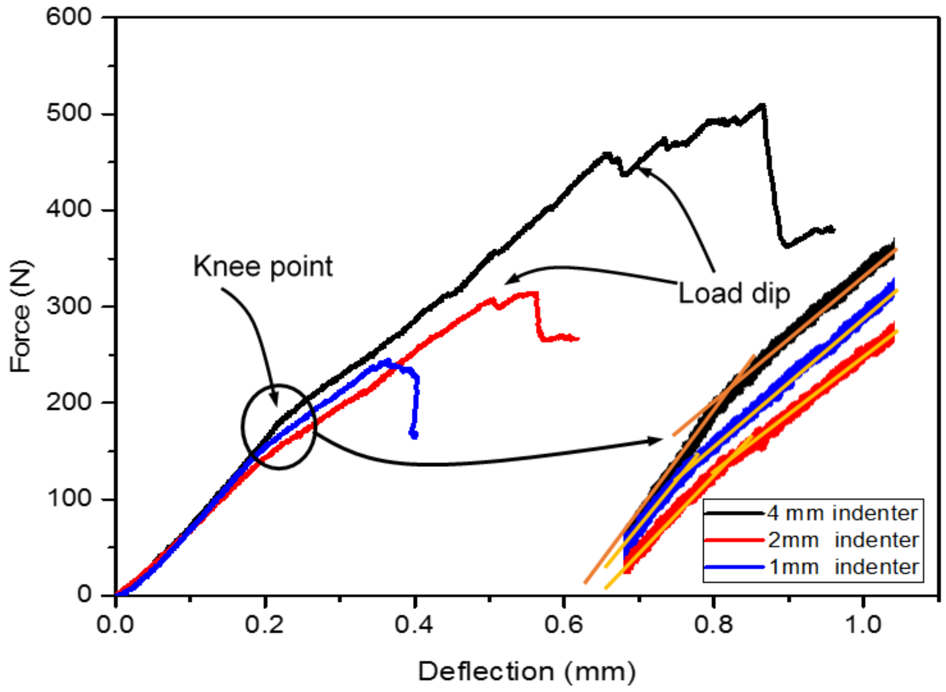

Figure 6.1: Experimental force displacement curve for three indenters 1, 2, and 4mm diameter.

The force-displacement curves show four distinctive features:

(a) Elastic region - The initial linear response is the same for all the load cases and corresponds to elastic loading as one would expect. The slope of the curve in this region is the elastic stiffness.

(b) Knee point – There is a knee point just above 0.2mm displacement which corresponds to a change in the slope of the curve. This is expected to be associated with the onset of damage in the composite resulting in an increase in the compliance of the plate. The new slope appears to be similar in all three cases, indicating that this is not a strongly size-dependent feature. If the initial damage is similar it indicates that this is largely due to the bending deformation rather than the localised stresses due to the indenter contact. The knee force load is slightly different for each case, with the 1mm case having the lowest value and the 4mm case having the highest. These curves are in order of increasing size, as expected for a contact-related failure. There is a slight effect of indenter size on delamination initiation. The slope of the force-displacement curve decrease after this point due to the sudden reduction of laminate stiffness caused by delamination. This knee point also clear for the 2mm indenter.

(c) Load dips - A number of small dips in the force are seen as the plate is loaded beyond the knee point load. The number of these dips depends on the size of the indenter. The biggest indenter size has more load dips. Each load dips indicates failure of fibre bundle or collection of fibres. The biggest indenter size rests on many number of fibres. The increase of load after first load dip indicates that the next fibre carries the additional load result from the failure of the first damaged fibre. The sound of fibre breakage was heard for the first time when the transient load dip happened during the quasi-static test. For 4mm indenter, the first transient load dip occurred at 452 N while the final failure occurred at 504 N. This explain that the laminate carries additional load about 52 N after the first fibre breakage. For 2mm indenter, the first transient load dip occurred at 303 N, while the final failure occurred at 313 N. the difference between them just 10N, which is the additional load after first fibre breakage. For 1mm indenter, there is no transient load dip. The first fibre breakage is the same of the final failure load and the penetration occurs immediately as the indenter rest on a few fibres.

(d) Peak force – Above this force the load drops off steeply at which point final failure is assumed. As the indenter diameter decreases, it can be seen that the peak force decrease (about 500N for 4mm, 350N for 2mm, and 250 N for 1mm diameter). This is due to the decrease of contact area between the indenter and the specimen. The sharper small diameter indenter penetrates the specimen and changes some of the work done by the indenter to penetration energy or fibre breakage damage energy in addition to bending energy and other types of damage energy. For the large diameter, the total work changes to bending energy and damage energy neglecting the effect of penetration. This due to the large contact area between the indenter and the plate for large indenter which allows the plate to absorb enough energy and prevents the penetration.

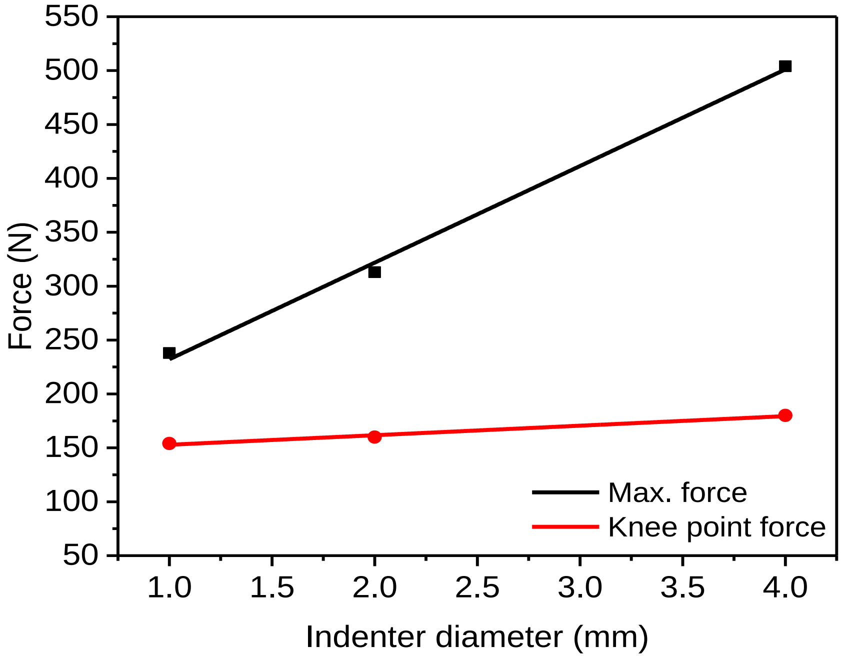

Figure 6.2: The effect of indenter size on effective forces under static load.

Figure 6.2 shows the effect of the indenter diameter on the maximum force or failure force that the laminate sustain before failure. This curve also shows size effect on knee point load which indicates that the three curves have almost the same knee point loads. For both curves, it is clear that the relation between size and maximum loads is quite linear.

This curve indicates that the initiation of delamination does not depend on the indenter size but it depends on the bending stress lower plies. On the other hand, peak force depends directly on the size of the indenter as the final failure results from fibre breakage under the indenter.

6.1.2 Internal damage

A sample from the impacted region of the damaged CFRP laminate was prepared for 3D scanning. As a first step, a damaged specimen is cut into small pieces to observe the shape of damage under a microscope. The sample is firstly polished and ground to obtain a good microscopic image. This process is not accurate to see all the damage within the laminate i.e. fibre breakage, matrix cracking, and delamination. This process also may cause an extra damage because of cutting as the cutting should be into the damaged area. The shape of the delamination at the edge of the cut sample is shown in Figure 6.3.

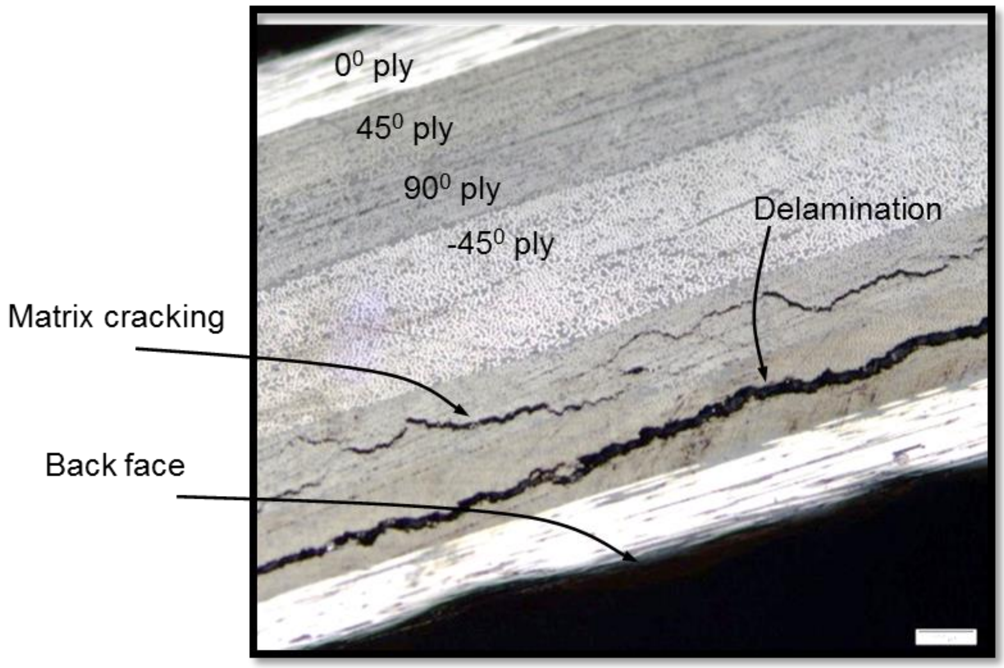

Figure 6.3: Typical delamination morphology of the layups.

To obtain a reasonable resolution and remain within the system field of view, a 3D reconstruction of the internal damage in the composites has been created in accordance with the procedure described in Chapter 5. In this study, the delamination area and the matrix cracking were detected and each type of damage and each delamination layer within different ply colored in different colure. This process was conducted within VG Studio software. The shape of the delamination area between all plies is presented in. The delamination area increases towards the back face of the laminate e.g. in tension side. The shape and size of delamination area depend on many factors such as the orientation of fibres in adjacent plies, the thickness of the laminate, the properties of the ply and cohesive material, and the shape of the indenter. In this study, the effect of the indenter is presented and discussed in the next sub-section. The delamination area increase as the diameter of the indenter increases. This can result from the fact that higher localised stresses under the smaller radius indenter lead to local matric failure and fibre breakage, whereas for larger radii the failure mode is initially dominated by global elastic deformation relieved by delamination. The shape of delamination area is similar for the 1mm, 2mm, and 4mm. The shape of the delamination depends mostly on the orientation of the fibre in the adjacent plies. The delamination starts with the orientation of the top fibre and propagates in the direction of the fibre of the bottom ply. In this study, the effect of the angle between any adjacent plies is the same i.e. (45^0) as the sequence of the laminate is $[0, 45, 90, -45]_s$. Thus, the change of delamination area size results from the position of ply from the impact point.

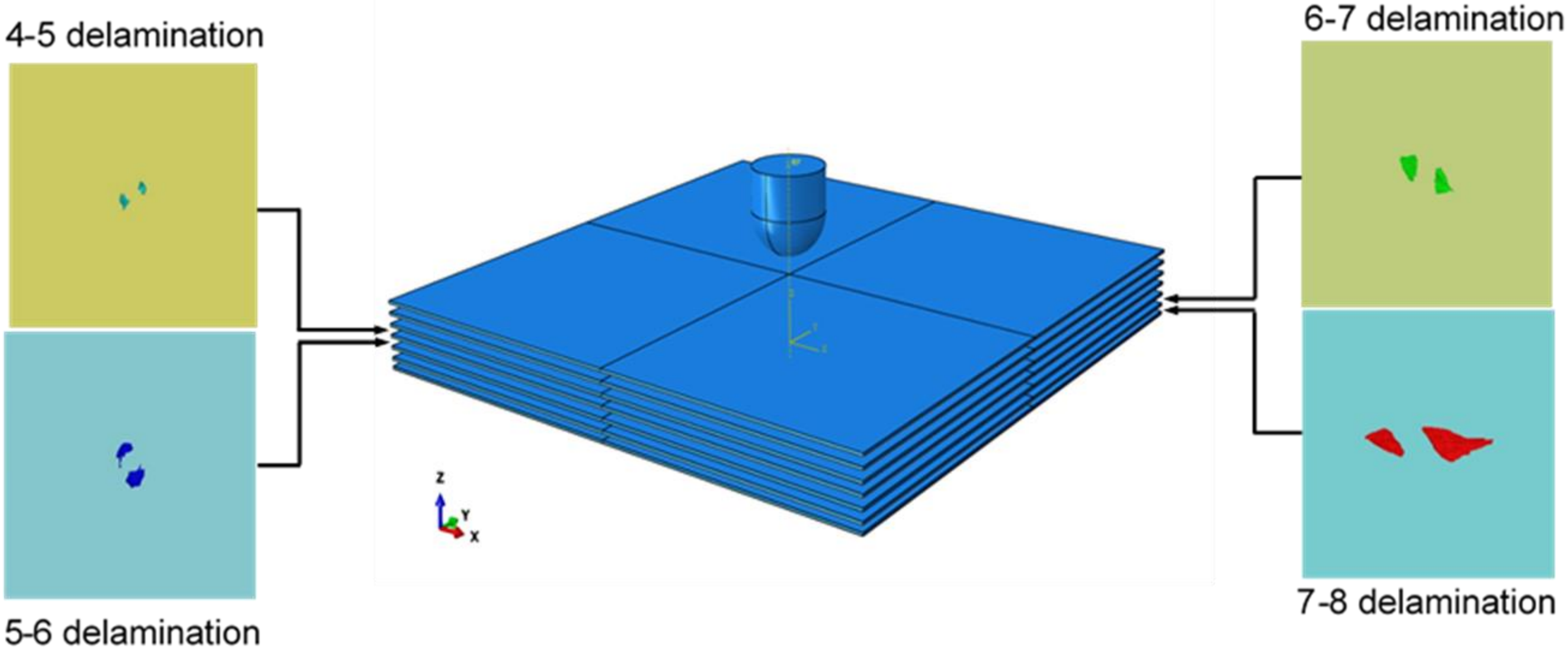

Figure 6.4: Delamination area between different adjacent plies of laminate under quasi-static load with 4 mm impactor under CT scan.

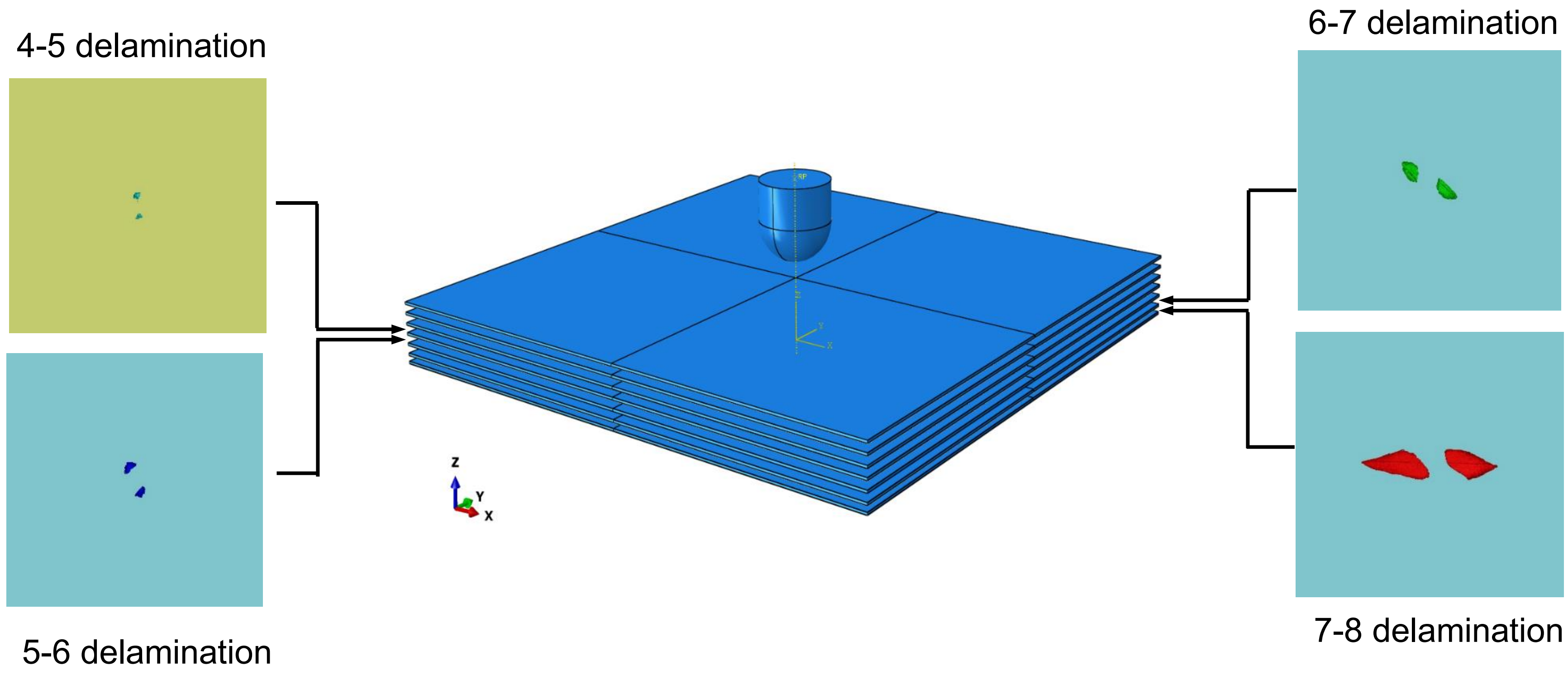

Figure 6.5: Delamination area between different adjacent plies of laminate under quasi-static load with 2 mm impactor under CT scan.

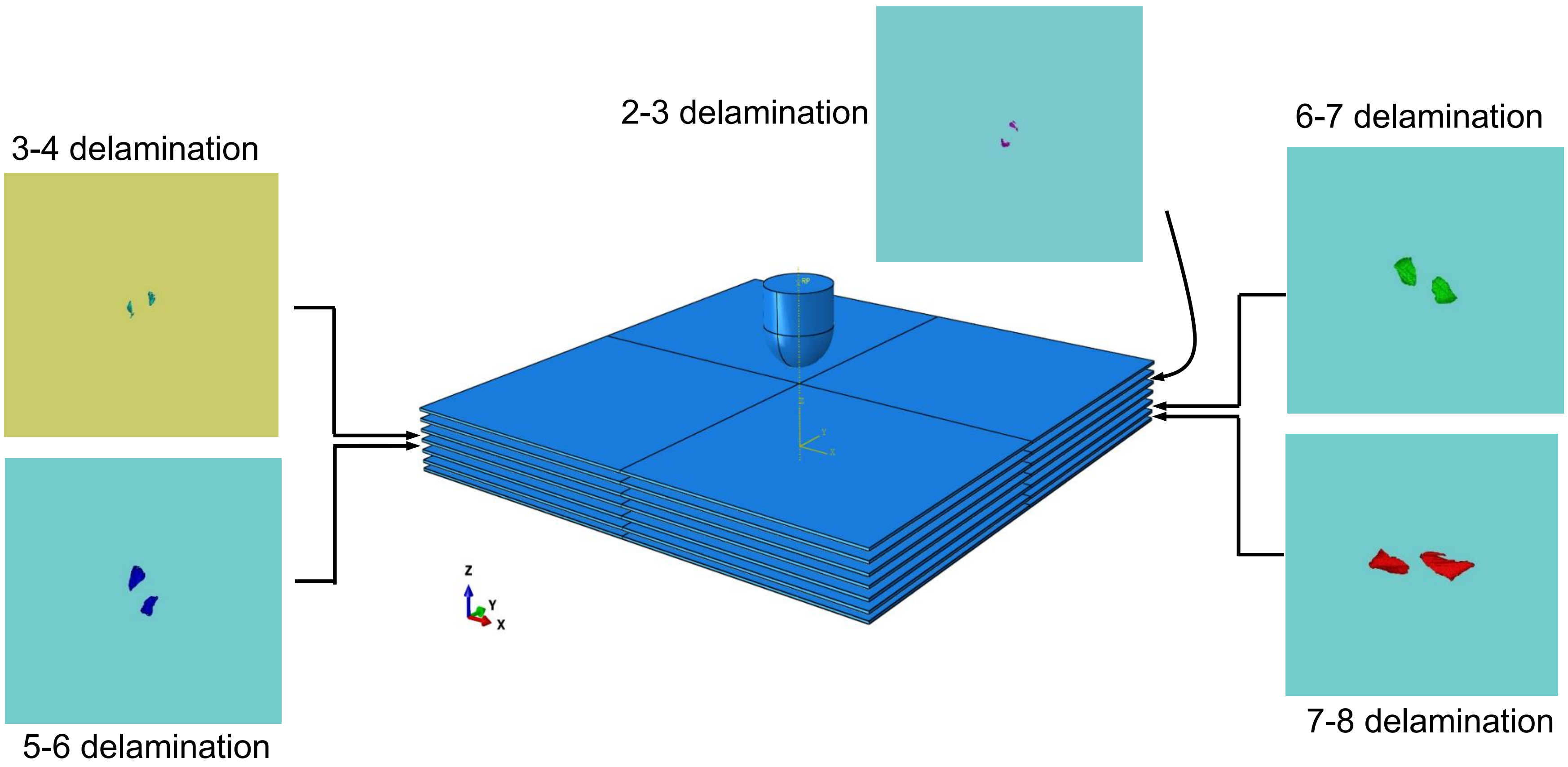

Figure 6.6:Delamination area between different adjacent plies of laminate under quasi-static load with 1 mm impactor under CT scan.

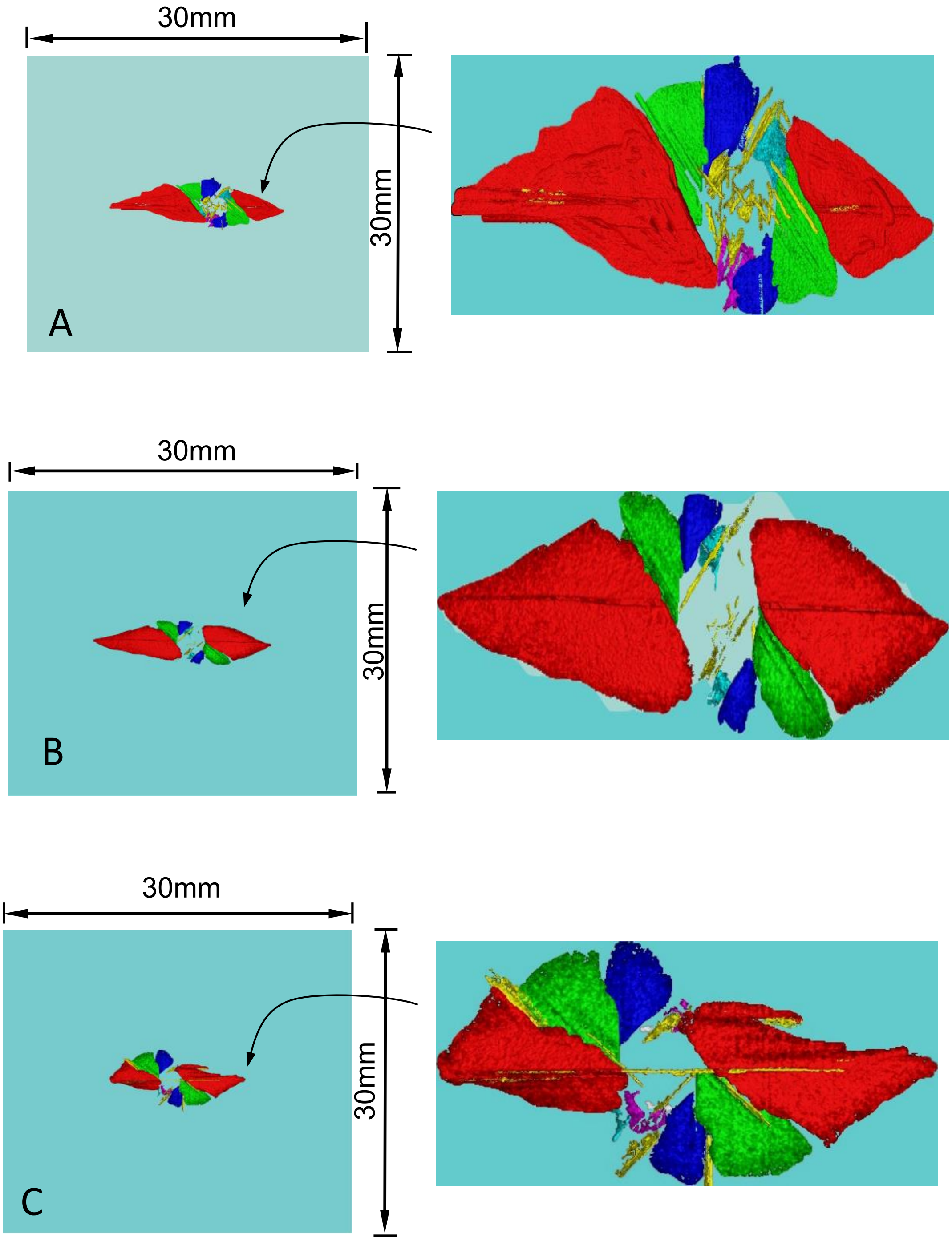

Figure 6.7: Delamination area between different adjacent plies of laminate under quasi-static load with 4 mm impactor under CT scan. (A) 4mm indenter diameter case. (B) 2mm indenter diameter case (C) 1mm indenter diameter case.

6.2 Numerical simulation

A comparison between the experimental and modelling work of the force-displacement response of the damaged specimen is presented in this section. The model is subjected to the same boundary conditions and initial conditions as the experimental part to validate the result, as described in Chapter 5.

6.3 Mesh Sensitivity

In this study, the size of mesh is 0.5*0.5 mm as the damage area is almost constant when the mesh size decrease.

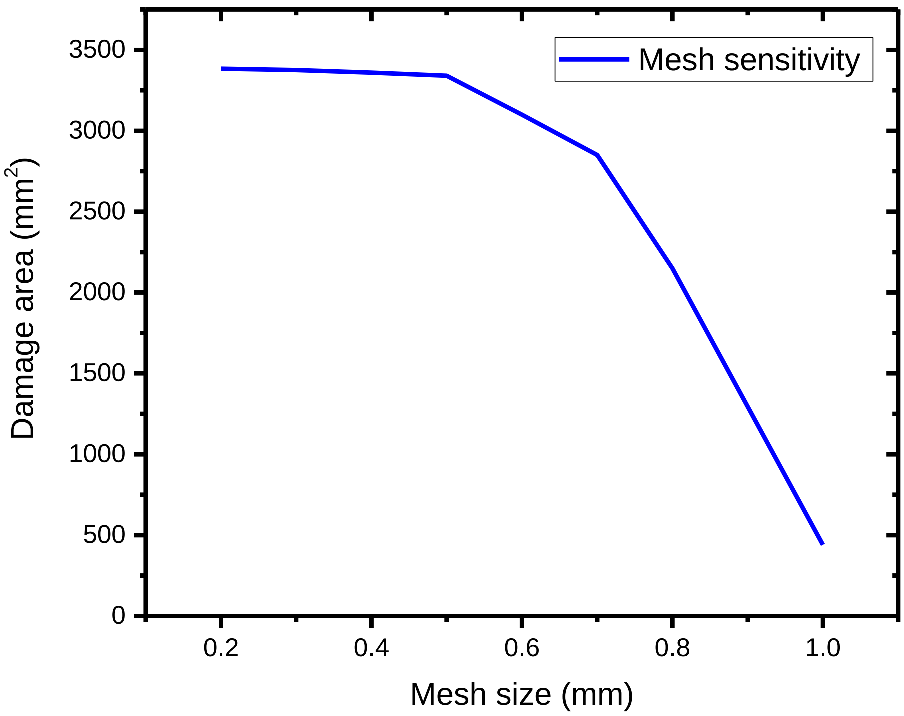

Figure 6.8: Mesh sensitivity of delamination area between 7th and 8th plies of 4mm static load.

320,000 8-node quadrilateral in-plane general-purpose continuum shell elements were used to mesh the plies, while 280,000COH3D8 n 8-node three-dimensional cohesive elements for the seven cohesive layers. 484 linear quadrilateral elements of type R3D4 has been used to mesh the impactor and 5908 linear quadrilateral elements of type R3D4 has been used to mesh the support.

The bottom base of the support fixed in all directions, while the indenter is free in the vertical direction (z-direction that perpendicular to the plate) and fixed in all other directions. A 1mm initial displacement was given to the indenter in this direction which equals to the displacement from the experimental procedure. In this study, the number of increments is 10000 with an initial increment size of 0.005 and minimum increment $1x10^{-15}$. The damping in this study is not considered and the default value of viscosity is used with 0.06 and 1.2 N s/mm^3 for linear and quadratic artificial viscosities.

6.3.1 Force-displacement behavior

To validate the results that obtained from ABAQUS, the simulated force-displacement curves for all three indenter cases are shown in Figure 6.9.

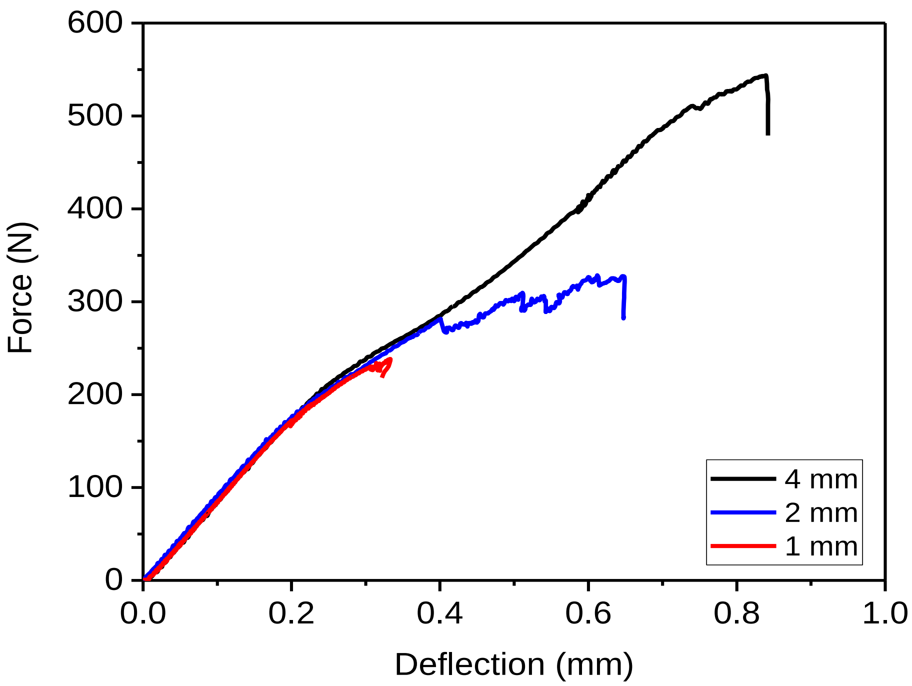

Figure 6.9: Force-displacement curve of three indenters.

Figure 6.9 shows four distinctive features as same as with the experimental results:

(a) Elastic region: the elastic region is similar for all three different indenters with same slope within this region which indicates that ABAQUS is accurate enough in this region. The slope of elastic region depends completely on the interface stiffness of the cohesive layer [70].

(b) Knee point: There is a knee point for all three curves just at 0.2mm displacement. The slope of all curve is the same for all three curves after the elastic region. The presence of knee point indicate that the dominant failure is delamination and ABAQUS captured the reduction in laminate stiffness due to delamination properly.

(c) Load dips: the general trend of load dips is similar with experimental results i.e. the number of load dips increase with the size of indenter. The range of load dips values are 222,280, and 508 N for 1, 2, and 2mm diameter respectively.

(d) Peak force: the effect of indenter size is clear for the peak force. It can be seen that the peak force decrease as the diameter of the indenter decrease (222 N for 1mm, 321N for 2mm, and 539N for 4mm).

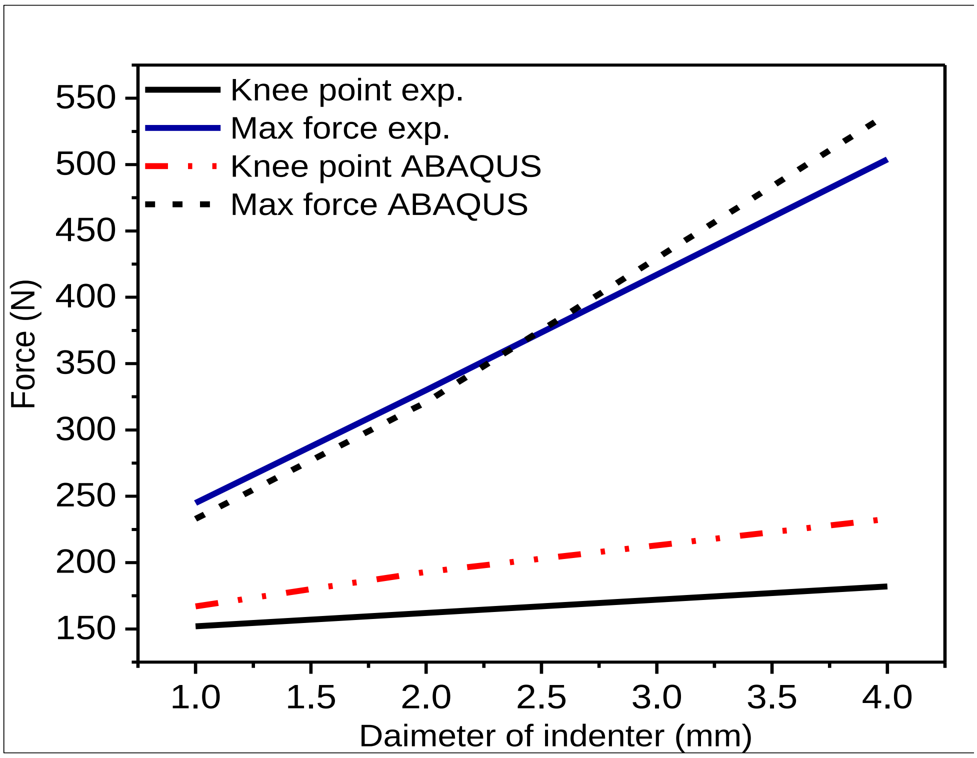

Figure 6.10: The effect of indenter size on effective forces under static load for experimental and modelling part.

6.3.2 Internal damage

As discussed before, cohesive zone model has been used to simulate the shape of the delamination between adjacent plies. In this work, the thickness of the cohesive layer is 1x 10^{-6} m. Quads stress criterion (QUADS) has been used to model the delamination as it gives more accurate results than maximum nominal stress.This differince in results between two criteria because maximum nominal stress does not take into account the relation between the different stress direction as the (QUADS) [92] [100].

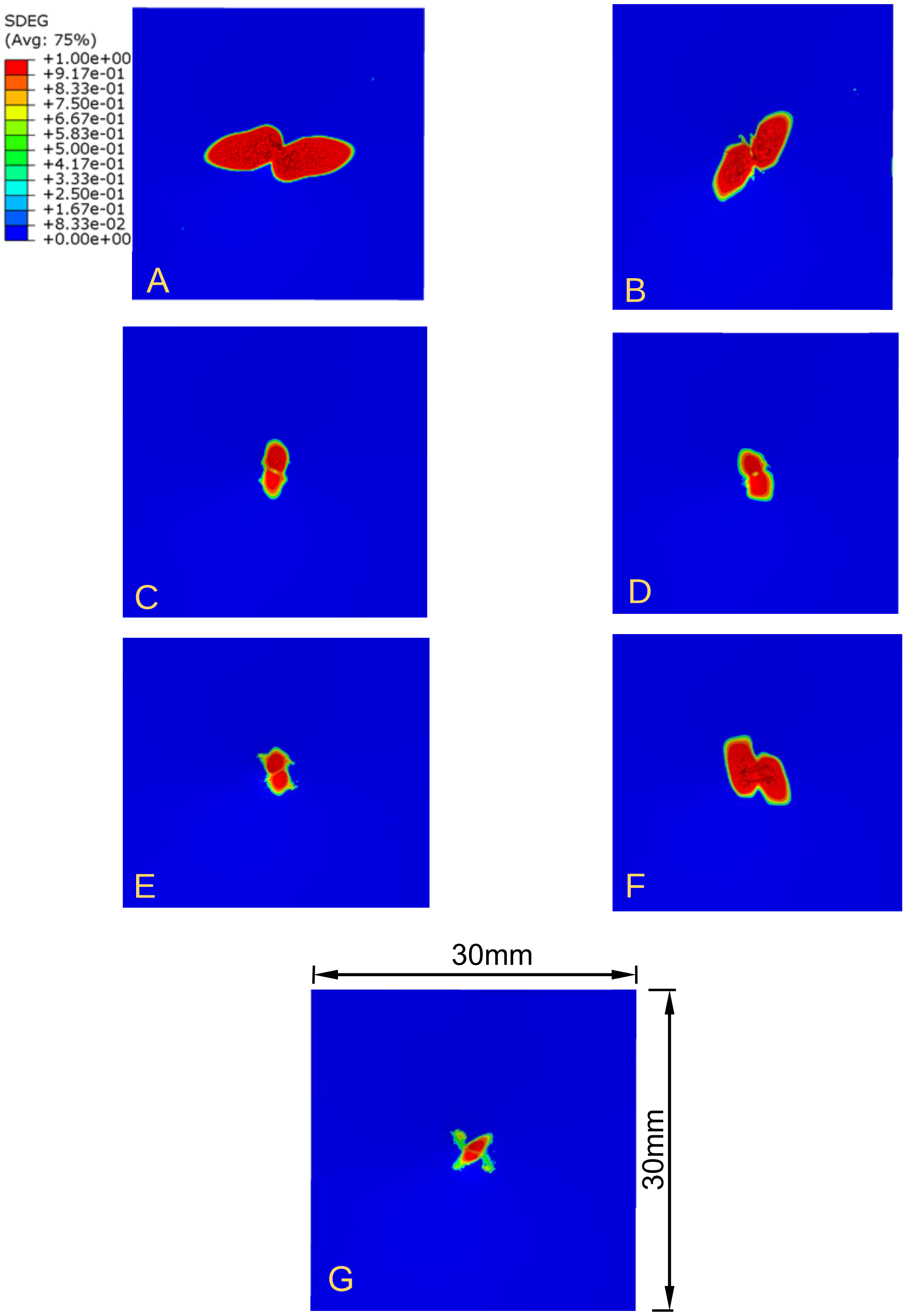

Figure 6.11: Delamination area between different adjacent plies of laminate under Quasi-static load with 4 mm impactor. (A) Between 7th and 8th plies. (B) Between 6th and 7th plies (C) Between 5th and 6th plies (D) Between 4th and 5th plies (E) Between 3rd and 4th and 5th plies (F) Between 2nd and 3rd plies (G) Between 1st and 2nd plies.

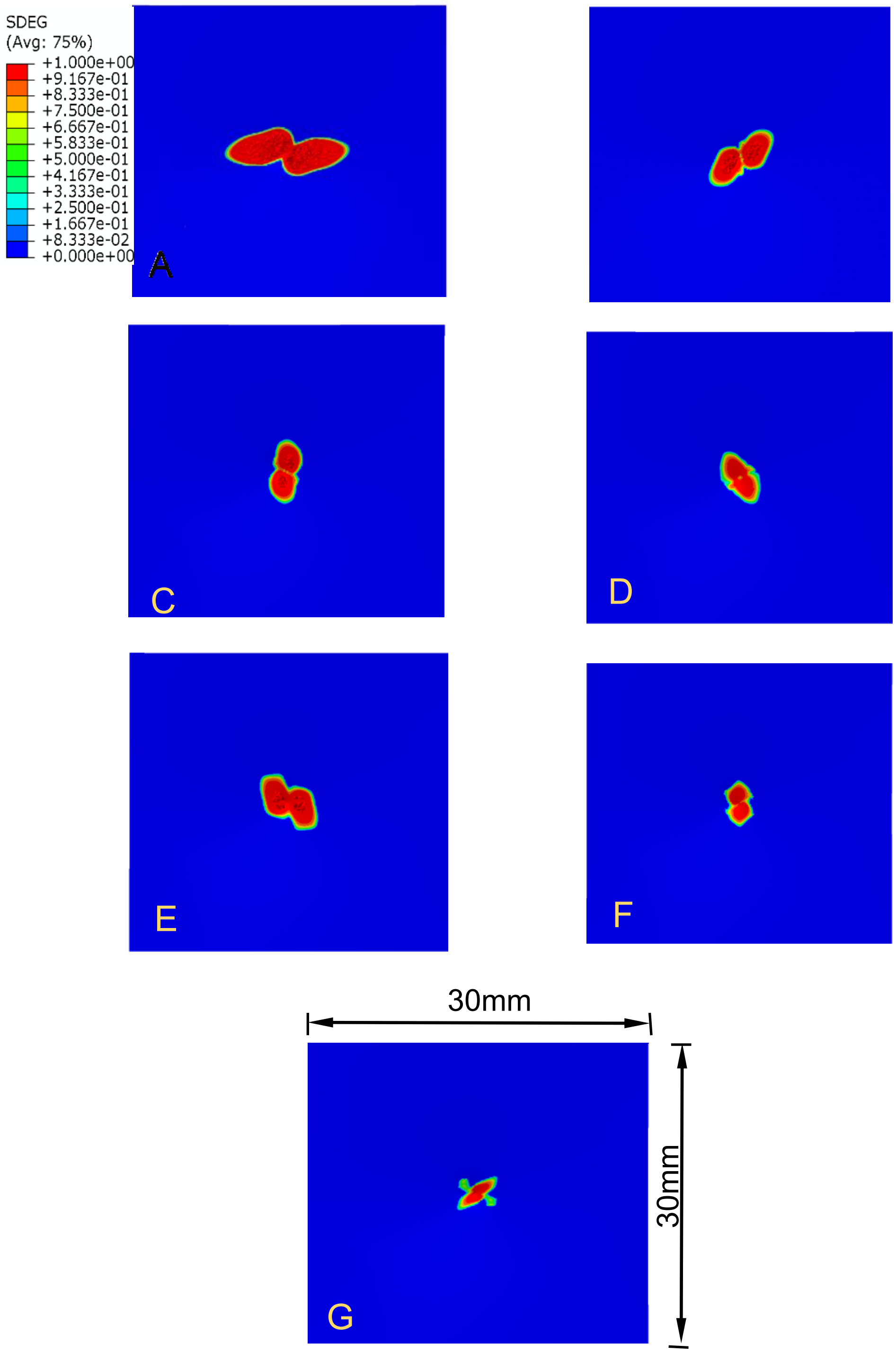

Figure 6.12: Delamination area between different adjacent plies of laminate under Quasi-static load with 2 mm impactor. (A) Between 7th and 8th plies. (B) Between 6th and 7th plies (C) Between 5th and 6th plies (D) Between 4th and 5th plies (E) Between 3rd and 4th (E) Between 3rd and 4th plies (F) Between 2nd and 3rd plies (G) Between 1st and 2nd plies.

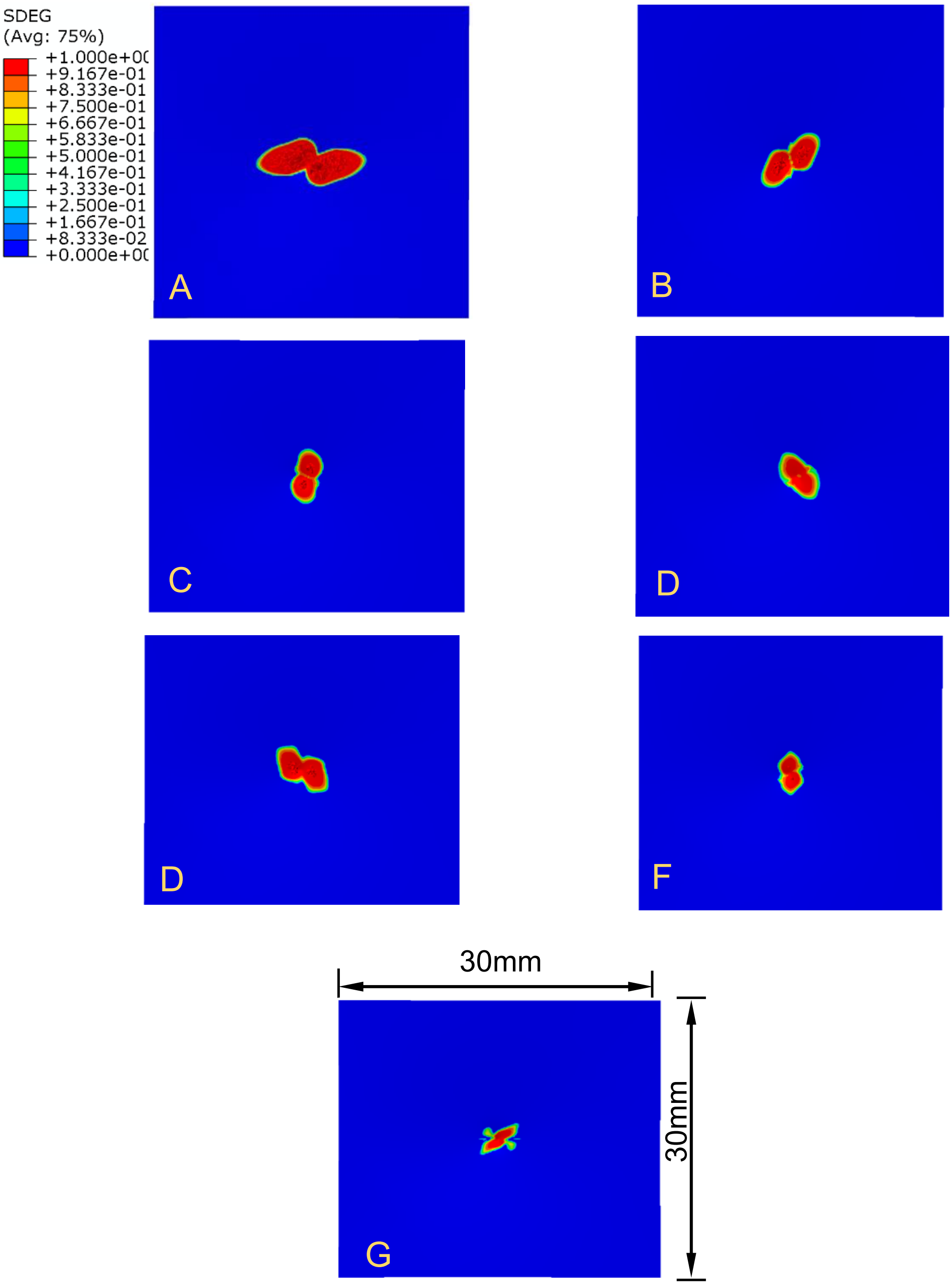

Figure 6.13: Delamination area between different adjacent plies of laminate under Quasi-static load with 1 mm impactor. (A) Between 7th and 8th plies. (B) Between 6th and 7th plies (C) Between 5th and 6th plies (D) Between 4th and 5th plies (E) Between 3rd and 4th (E) Between 3rd and 4th plies (F) Between 2nd and 3rd plies (G) Between 1st and 2nd plies.

The shape of the damaged area as shown Figure 6.11, Figure 6.12, and Figure 6.13 form depends on these directions. The shape of the delamination is a figure eight. The major axis aligned with the bottom ply orientation while the minor axis aligned with the top ply.

The shape and size of delaminated area depend on many factors such as the distance to the impacted point i.e. whether the area in the tension side or in compression side. Generally, the delamination result from shear stress or tensile stress. The delamination in the mid-thickness is generated due to shear stress while the main delamination result from the tension stress results from bending in the further point from the impact point which causes the matrix cracking in this region.Some cracks are vertical and due to tensile bending in this region theses cracks extend to reach the area between adjacent plies and cause delamination within this region.

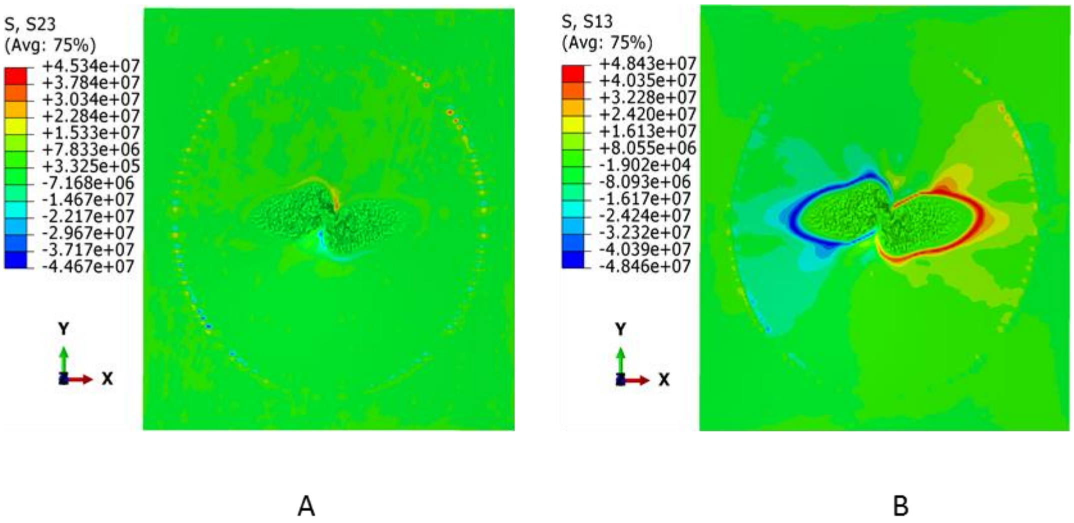

Figure 6.14: Shear stress distribution in cohesive layer between 7th and 8th plies (a) S23 (B) S13.

From Figure 6.11 to Figure 6.13, the main and the biggest delamination area occurs between the 7th and 8th plies as the tension is the maximum at this area while the minimum delamination area occurs near to impact point. Delamination also strongly depends on the orientation of the fibres in the adjacent plies. The shape of the damaged area as shown in previous figures depends on these directions. The shape of the delamination is a figure eight. The major axis aligned with the bottom ply orientation while the minor axis aligned with the top ply. From these figures, it is also shown that as the diameter size increases, the matrix cracking increase (shown as yellow lines). As discussed in section 3.3.1. The shape of stresses within plies play an important role in the final shape of delamination. Figure B shows dominant in-plane shear stress is in x-direction due to anisotropy. It is maximum at delamination front as one would expect, with complete relief in the delaminated zone.

6.4 Comparison between experimental and modelling work

6.4.1 Force displacement curves

To validate the modelling results, the modelling force-displacement curves have been drawn side by side with experimental curves for all three indenter diameters.

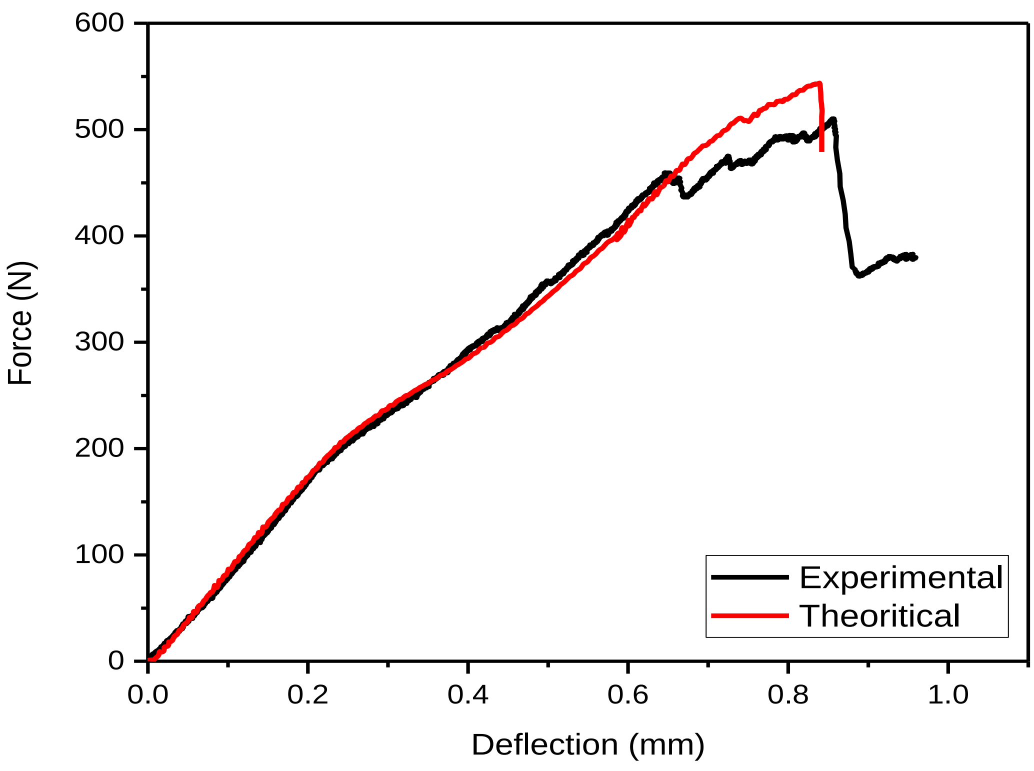

Figure 6.15: Force-displacement curve of 4mm diameter.

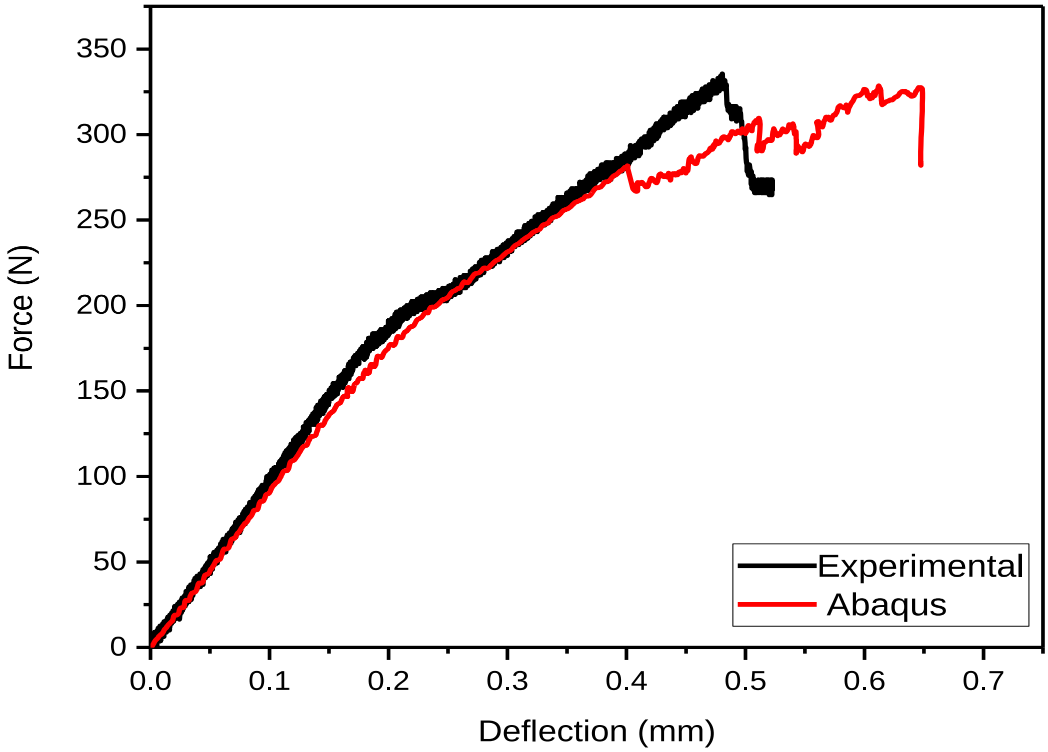

Figure 6.16: Force-displacement curve of 2mm diameter.

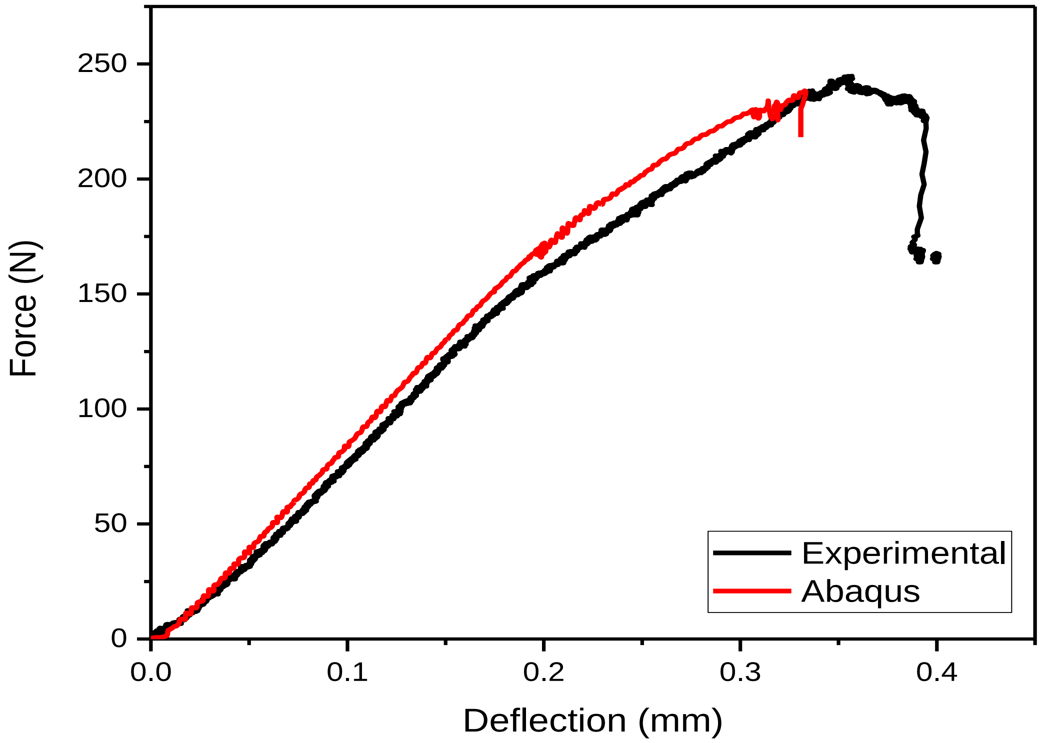

Figure 6.17: Force-displacement curve of 1mm diameter.

The experimental results of Figure 6.1 for the three indenter cases are compared with the numerical results of Figure 6.9 in the following Figure 6.15 to Figure 6.17. It can be shown that the force-displacement or global response of static experimental part is similar in the elastic part of all three indenters of damaged specimen with modelling part. The modelling part captures all the essential features in the force-displacement curves in all different cases such as knee loads and dips loads.

The four distinctive features seen in section 6.1.1 are reproduced in the simulation results to different levels of accuracy as one might expect:

(a) Elastic region: the elastic region is similar in both case i.e. experimental and modelling for all three different indenters as would be expected because the modelling part was built in the same condition with experimental in term of boundary condition and initial conditions.

(b) Knee point: modelling result agrees well with the experimental at this point. The knee point at 0.2 mm for all cases. The slope after the knee point is the same for all cases (experimental and modelling results).

(c) Load dips: the general trend of load dips is the same for both cases i.e. experimental and ABAQUS. The range of load dips values are 239, 303, and 508 N for the experimental and for 239, 273, and 508 N theoretically for 1, 2, and 4mm diameter respectively.

(d) Peak force: there is a slight difference between the peak force in Experimental and modelling results in all three cases. In 4mm diameter the peak force for the experimental and modelling are 504, 538 N respectively and 313,324 for 2mm indenter, and 239,232 for 1mm indenter

6.4.2Internal damage

The shape of the delamination area in the modelling part is quite similar to the experimental part but there is no space between the two parts of the figure eight as the experimental one. This because the modelling part does not take into account the effect of the indenter on the delamination as the compression results from the impact works as an additional out of the plane strength of the laminate. This prevents the presence of delamination under the impactor. This effect explains the increase of this space with increasing the diameter of the indenter. Generally, the size of the delamination area in the modelling part is smaller than in experimental part because of the effect of the space between the two parts of fiigure eight. The direction of the major and minor axis of delamination area in the modelling part agree well with the experimental part. In the quasi-static part, the size of the delamination area increases with the diameter of the indenter. The length of the major axis for 4, 2, and 1mm is shown in Figure 6.18.

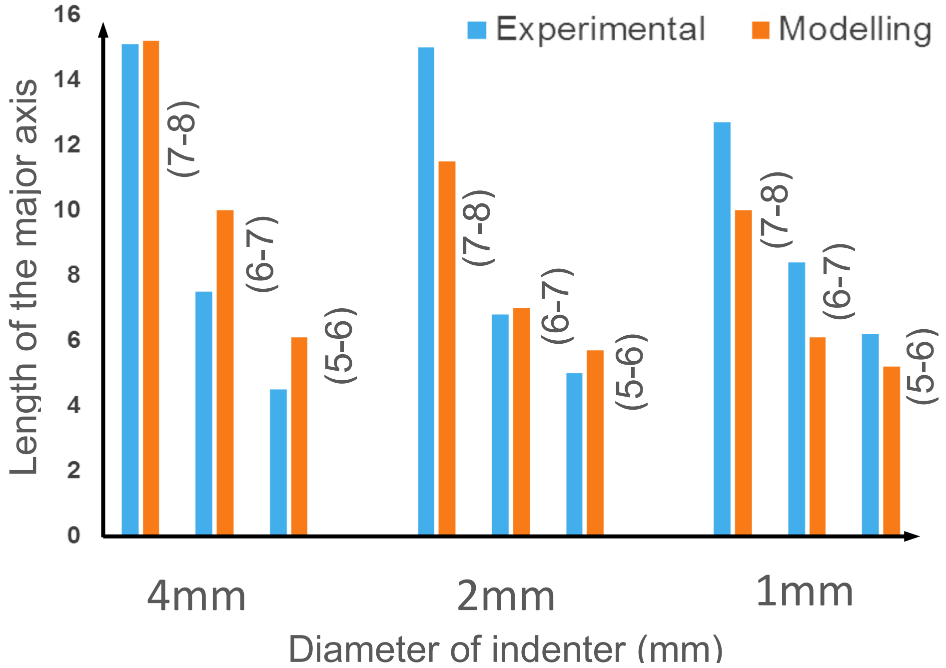

Figure 6.18: Comparison between experimental and modelling size of delamination.

The length of the major axis of 4, 2, and 1mm indenter diameter in the last three cohesive layers i.e. 7^{th} - 8^{th}, 6^{th} - 7^{th}, and 5^{th} - 6^{th} is shown in Figure 6.18. These delamination area are chosen because these delamination areas are the most dangerous and are considered the main reason for losing stiffness of the laminates under such type of loading. In general, the delamination area in experimental and modelling part is quite similar to 1, 2, and 4mm indenter diameter. In different diameter indenter, the delamination between the same adjacent plies increases with the diameter of the indenter. i.e. (the delamination between 7th and 8th plies of 4 diameter indenter is bigger than the delamination between 7th and 8th plies of the 2mm indenter diameter and bigger than the 1 mm diameter). This clear in the modelling part as the same material parameters and boundary conditions have been chosen. For the experimental part, the same trend is shown with the small difference as the experiments will also have scatter if repeated.

To clarify the effect of cohesive layer position and tensile bending stress on the start of delamination, a time sequence curve of all cohesive layers of the laminate has been drawn in Figure 6.19

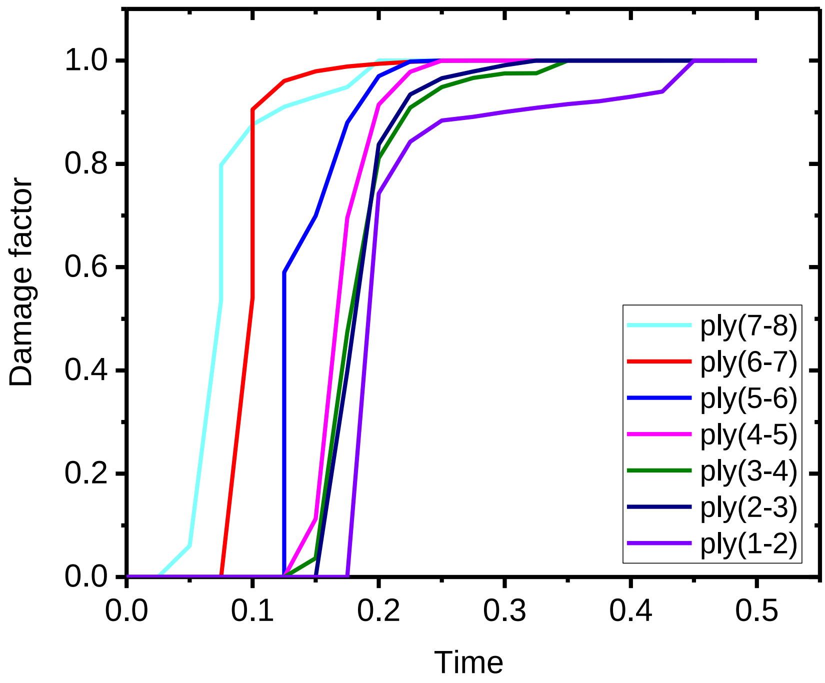

Figure 6.19: Time sequence of delamination in different adjacent plies.

As shown in Figure 6.19: Time sequence of delamination in different adjacent plies, the delamination starts at the cohesive layer between ply 7 and 8 followed by the cohesive between 3 and 4 plies and 6-7 cohesive layer. The last damage occurs between plies 1 and 2 and 3 and 4 plies. This indicates that the delamination depends on both the position of the cohesive area and the orientation of the fibre of the adjacent plies above and below the cohesive layer.

It is worth noting that there the complex interaction between delamination and matrix crack and the delamination is second stage of crack propagation. Cracks at bottom layers from the load surface are vertical and caused by the bending effect at these layers. The dominant mode at these layers which is the main reason of crack propagation and delamination is Mode I [101]. Thus, the initiation of delamination is controlled by mode I and the propagation of delamination is typically a mixed shear mode (II and III). The shape of shear stress distribution for both static and dynamic stress are quite the same as shown in Figure 3.15 and Figure 3.16.

Chapter 7 Results of dynamic loading

In this chapter, the CFRP specimen is tested and analysed under low-velocity impact. The structure is similar to chapter 5, in that the experimental work is presented initially, then the simulation results, followed by a comparison between them.

7.1 Experimental work

7.2 Force-displacement behaviour

In the experimental work, the external work done of the dynamic part is the same as the work of the static case in each case. The velocity of the impactor has been calculated due to the static part in section 5.3 which is 1.134 m/sec. the same procedure of the static part is repeated in this part in term of studying the effect of the diameter of the impactor on the force-time, displacement-time, and delamination area.

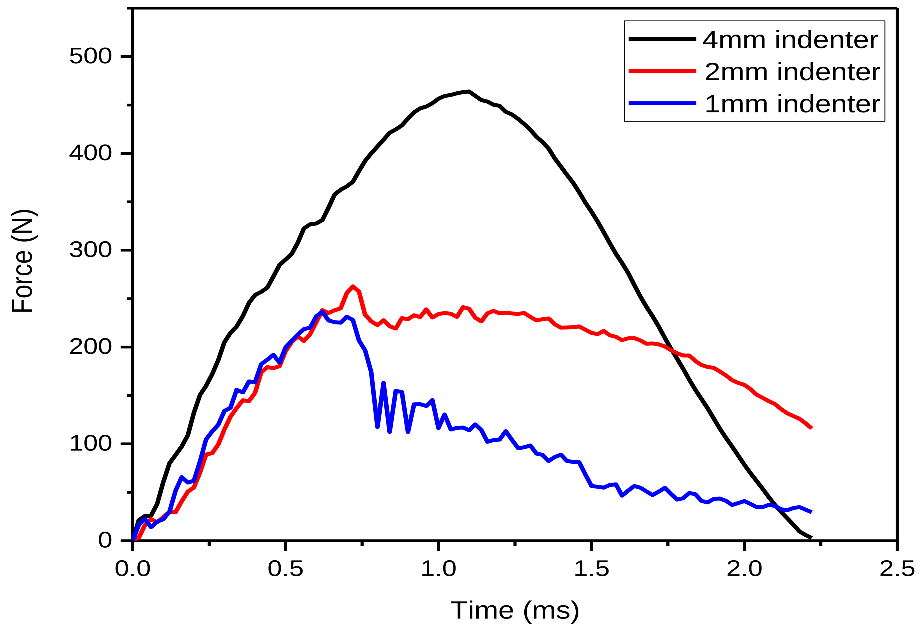

Figure 7.1: Experimental force- time curve of composite laminate under dynamic loads with three different impactors.

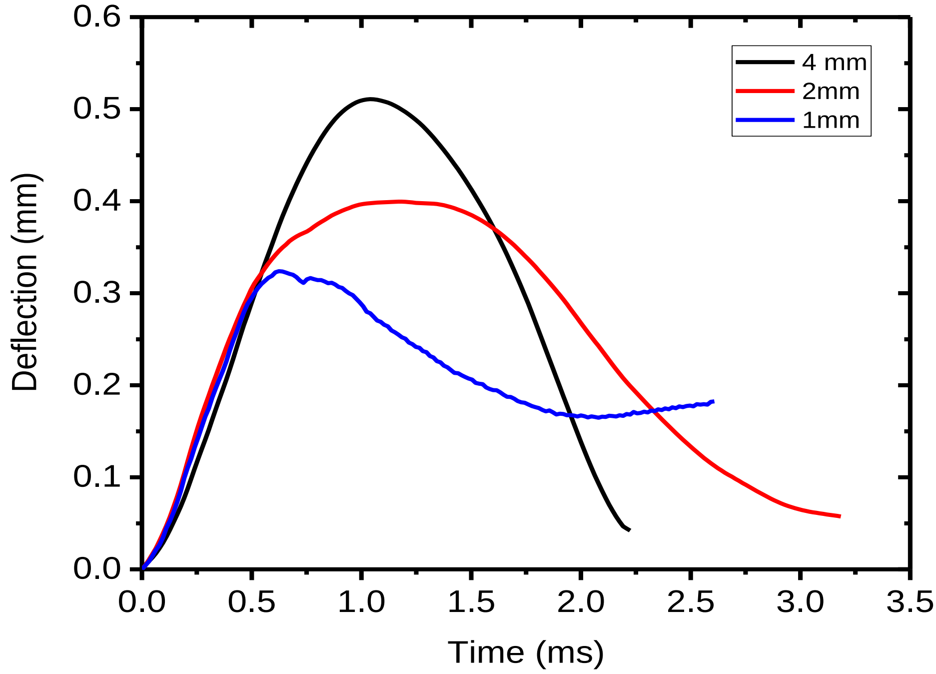

Figure 7.2: Deflection- time curve of composite laminate under dynamic loads with three different impactors.

From Figure 7.1 and Figure 7.2, it is clear that the force and displacement increase as the diameter of the indenter increase. Also, from previous figures, many features can be captured such as:

a) Elastic region: all curves have the same slope within this region which is clear in displacement-time curve rather that the force-time curve. This region ends just below 0.7ms for all impactor size.
b) Damage threshold load (DTL): The point in the curve where is a sudden reduction in force curve is called damage threshold load (DTL) [13] which indicate the initiation of delamination. This reduction result from the reduction of laminate stiffness which explain the reduction in force curve. The DTL for 1 and 2mm are 257 and 227 N respectively but the DTL is not clear in the 4mm force-time curve.
c) Load dips: There are many drops in all force-time curves that indicate local damage or matrix damage that effect on the force-time curves due

a slight decrease of laminate stiffness. This agreed with the study made by [4] which indicate that the DTL in a relatively high energy impact became less significant in load curve. This because the dominant failure will be the other type of damage such as fibre breakage rather than delamination initiation.

d) Peak force: in dynamic part, the maximum force of the curve is not the ultimate force the laminate sustain as the impactor reflects at the end of the impact time. The maximum force depends on the impactor diameter because the contact area will change accordingly. The maximum force of 1, 2, and 4mm was 226, 258, and 455N respectively.

It is also shown that the time of impact increase as the diameter of the indenter decrease. This indicates that the introduction of damage leads to increase the impact duration and decrease the maximum lad force and this agrees with the other results [102]. The difference between the 4mm indenter with 2 and 1mm is clear in term of force. This explains that for the 1mm, there is fibre breakage or penetration which make the laminate almost zero stiffness and there is no rebounding. For the 1 and 2mm diameter which the plate is clearly damaged, the force time curve is not symmetric about the maximum load point and this different from the results that were conducted by [103]. This result agrees with [96] regarding of the behaviour of the force-time curve and the presence of DTL and but the shape of the delamination is different. The previous study showed the sequence of delamination with time during the impact.

7.3 Internal damage

The same procedure of the static case had been followed to detect the delamination of the laminate subjected to impact load in term of the thickness of the cohesive layer and the type of criterion.

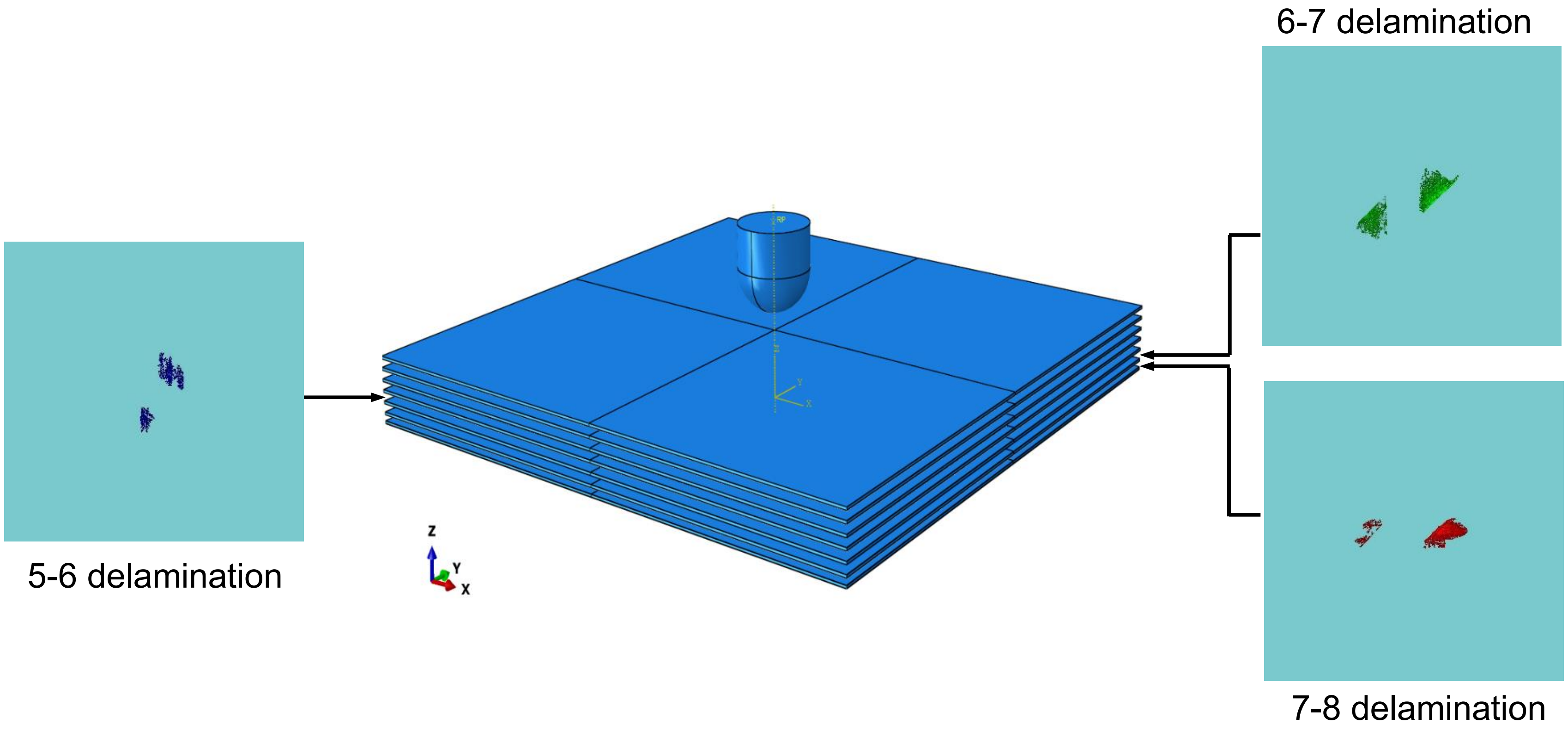

Figure 7.3: Delamination area between different adjacent plies of laminate under dynamic load with 4 mm impactor under CT scan.

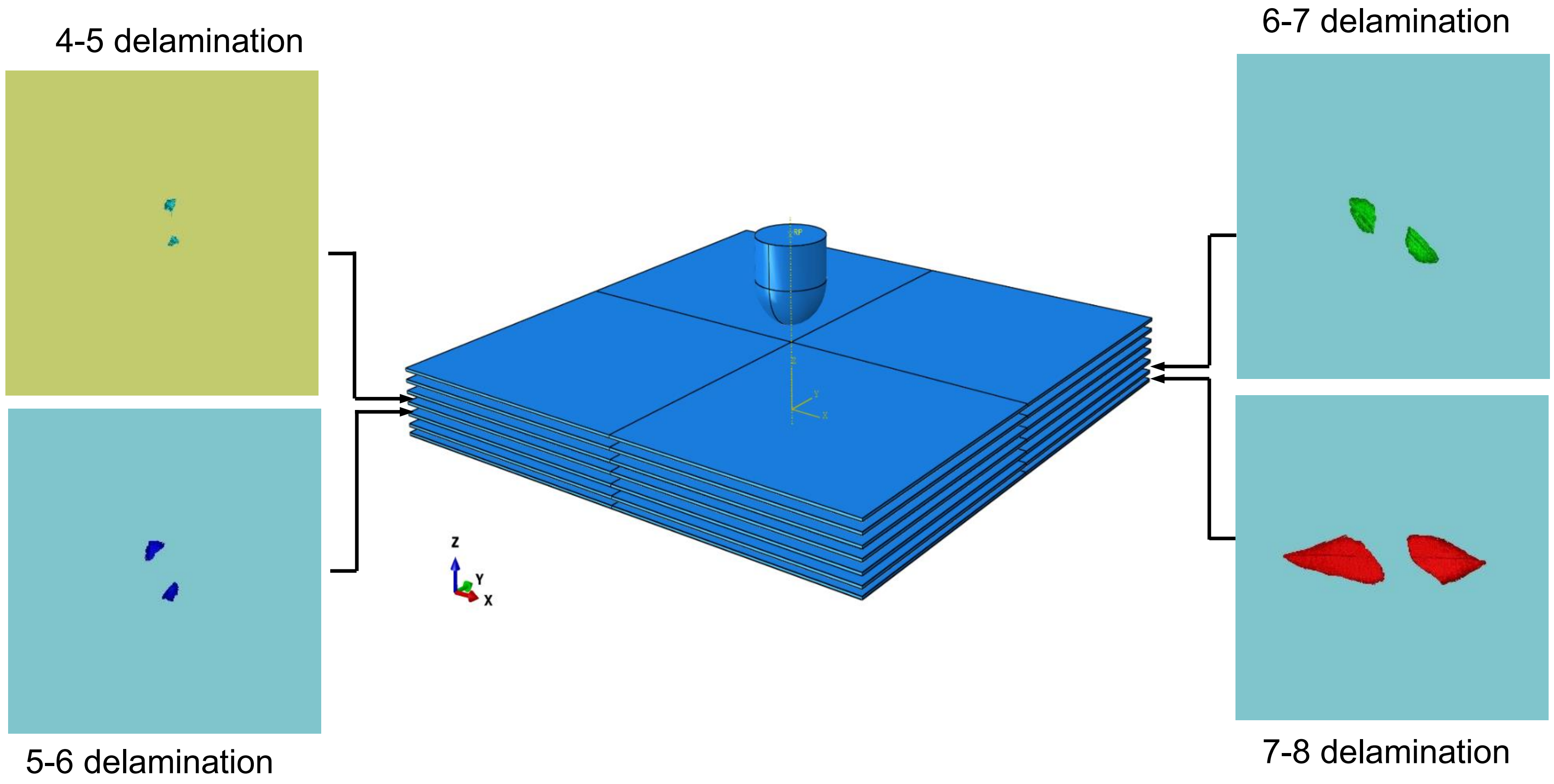

Figure 7.4: Delamination area between different adjacent plies of laminate under dynamic load with 2 mm impactor under CT scan.

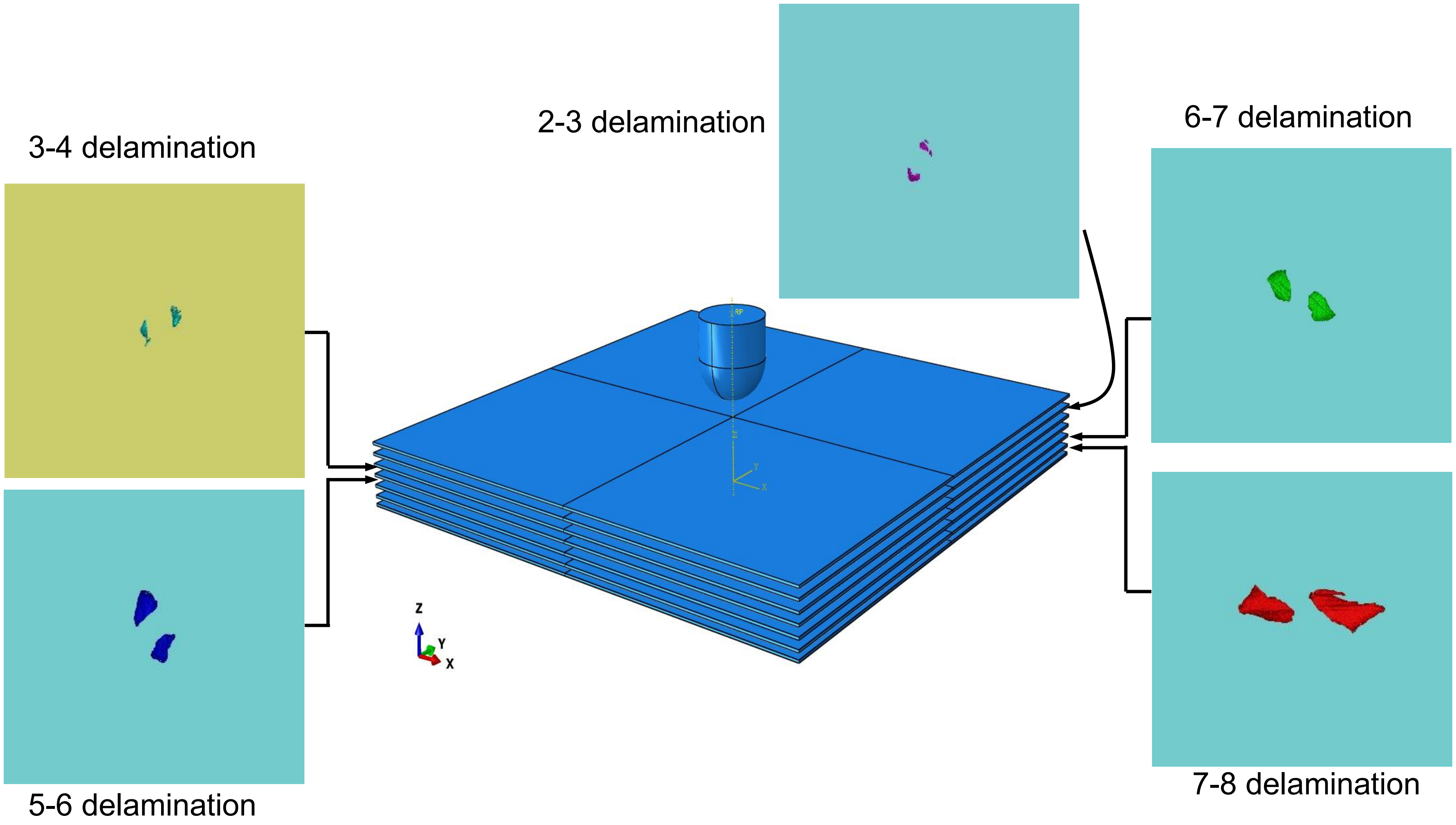

Figure 7.5: Delamination area between different adjacent plies of laminate under dynamic load load with 1 mm impactor under CT scan.

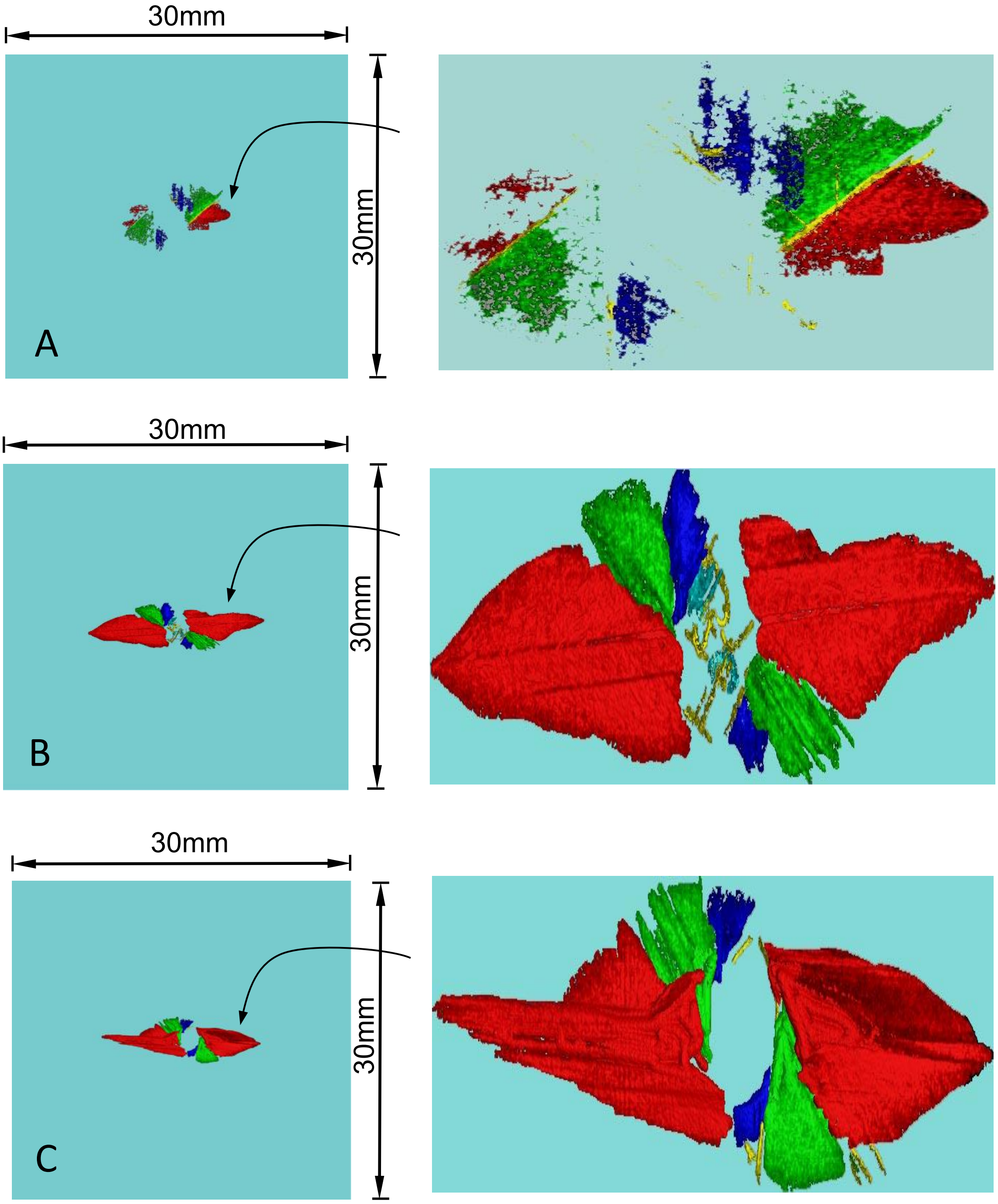

Figure 7.6: Delamination area between different adjacent plies of laminate under dynamic load with 4 mm impactor under CT scan. (A) 4mm indenter diameter case. (B) 2mm indenter diameter case (C) 1mm indenter diameter case.

7.4 Numerical simulation

7.4.1 Force-time and displacement- time curve

To show the effect of indenter size on force and displacement curve in dynamic part, force-time curve and displacement-time curves have been shown in Figure 7.7 and Figure 7.8. All analysis was performed on quad-core Intel i5-3470 processor and 32 GB RAM using the MPI based parallel solver available in ABAQUS/ Explicit. A total computing time of approximately 10 h was required for the simulation. The stable time increment ΔT can be redefined using the wave speed of the material, Cd, and element length, Le, as $\Delta T = Le/Cd$. The wave speed is given as $Cd = (E/\rho)^{1/2}$, where E is Young's modulus and ρ is the density of the material. The stable time increment calculated automatically by Abaqus was found to be adequate for most simulations conducted in this study. In the longitudinal direction wave speed in this model is and required time increment is 3.7x 10^{-5} and the default time increment of Abaqus is $1x10^{-5}$ and this value is efficient for the analysis.

In this study, the specimen consist of three parts composite laminate, impactor, and the support. The plate dimensions are (30x30x1mm) and contain eight plies. Each ply was modelled separately with an individual thickness of 0.125mm. The cohesive layer inserted between these plies to capture the delamination between them. The cohesive layer has 0.001mm thickness. All the plies and the cohesive layers considered as the 3D deformable body while the indenter and the support were modelled as discrete rigid. This because the study focuses on the plate behaviour and the indenter and the support are much stiffer than the plate. The time of the process is 0.0025 sec and this value is the same with the experimental value. In this study, the mass scaling was used to reduce the time of the job. $1x10^{-8}$ value was used as scale to target time increment. The value of the mass scaling should be chosen carefully to ensure that the kinetic energy will not increase more than 5% of the total value. Tie constraints were used to connect the cohesive layers with plies of composite material. The plate rests freely on the support. Many authors assumed different value of viscosity parameter and they found that the value of $1x10^{-3}$ N s/mm^3 gives good agreement with the experimental [70].

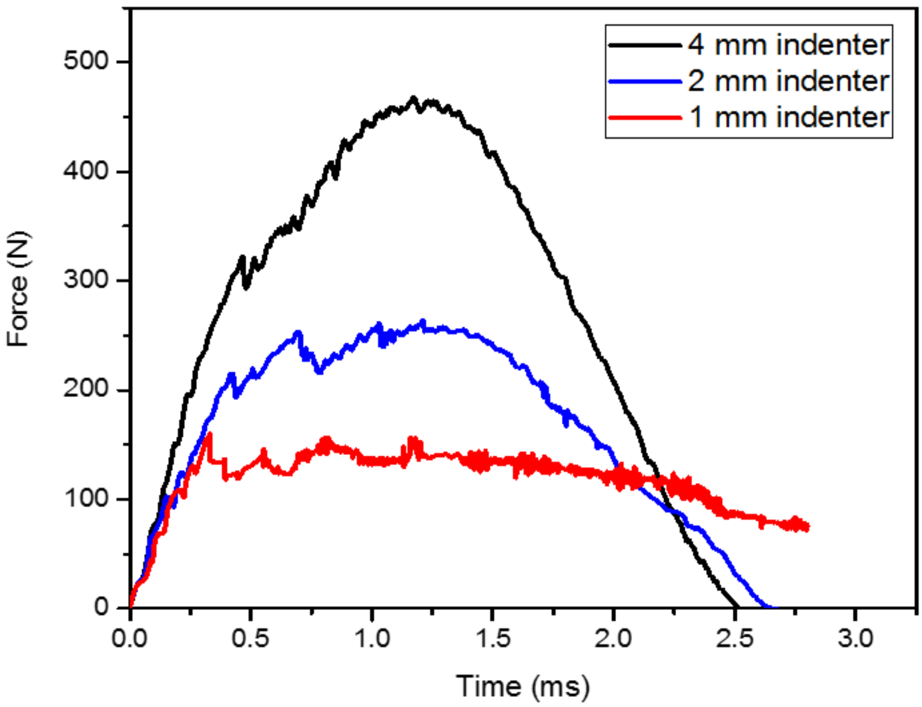

Figure 7.7: Numerical Force- time curve of low velocity impact for three different impactor diameters.

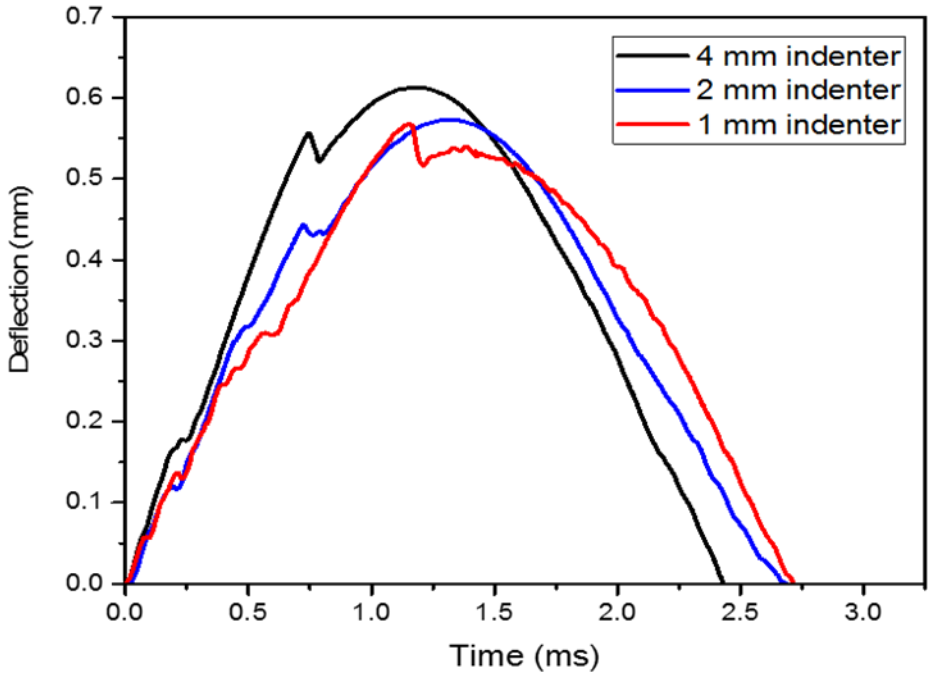

Figure 7.8: Displacement-time curve of low velocity impact for three different impactor diameters.

From Figure 7.7, the effect of impactor size on the force-time curve is clear. All the curves start with an elastic regions which have the same slope. This region ends around 100N or below 0.5ms. After this stage, there are many small drops which probably indicate the local damage or matrix damage under the impactor. R.C Batra [104] explained these drops as fibre breakage under the impactor which has a slight effect on the global response. Each curve has a different slope in this region and the slope depends on the size of the impactor. The slope increases with the diameter of the impactor. This region ends with a sudden reduction of force at different point that indicate the value of DTL. DTL is the maximum or ultimate load for 1mm diameter case as the fibre breakage occurs. The ultimate loads for 4, and 2mm are 459 and 249 N respectively. The dynamic threshold loads (DTL) are clear for 2, and 4mm (306, 203N) respectively. For 1mm case, the ultimate load is the same with DTL as the penetration and fibre breakage occurs immediately.

Figure 7.8 has the same features of in term of curve stage. The 1mm curve has the maximum value of displacement at same time with the sudden reduction in displacement which agrees with force curve as the laminate fails due to penetration. For 4, and 2mm the laminate carries further load beyond the first delamination initiation.

7.4.2 Internal damage

To compare the results of modelling work in term of delamination area, the same procedure of static load has been repeated for the dynamic work in term of the thickness of the cohesive layer, size of mesh and boundary conditions. The same thickness of the cohesive layer was used in the static part.

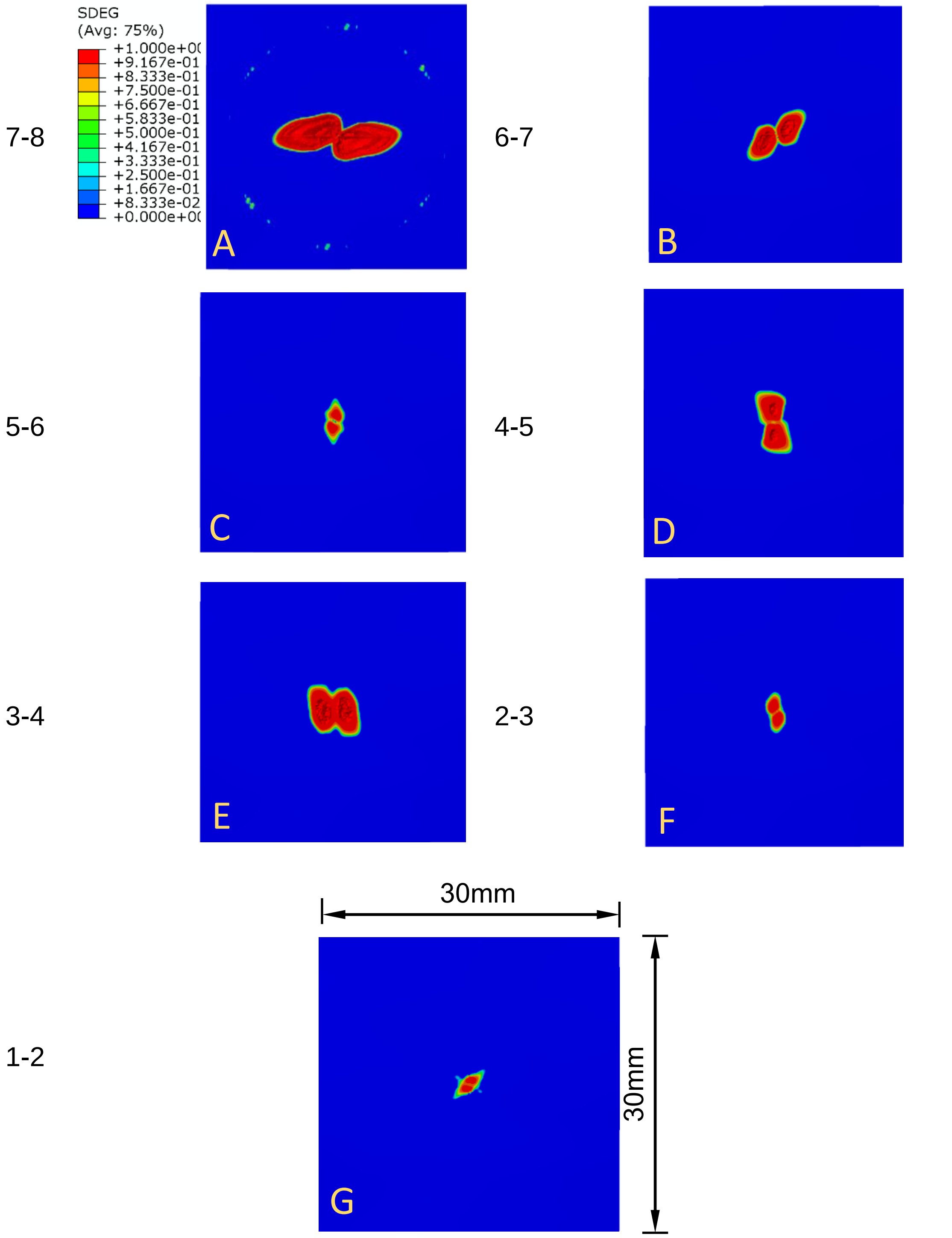

Figure 7.9: Delamination area between different adjacent plies of laminate under dynamic load with 4 mm impactor. (A) Between 7th and 8th plies. (B) Between 6th and 7th plies (C) Between 5th and 6th plies (D) Between 4th and 5th plies (E) Between 3rd and 4th plies (F) Between 3rd and 2nd plies (F) Between 1st and 2nd plies.

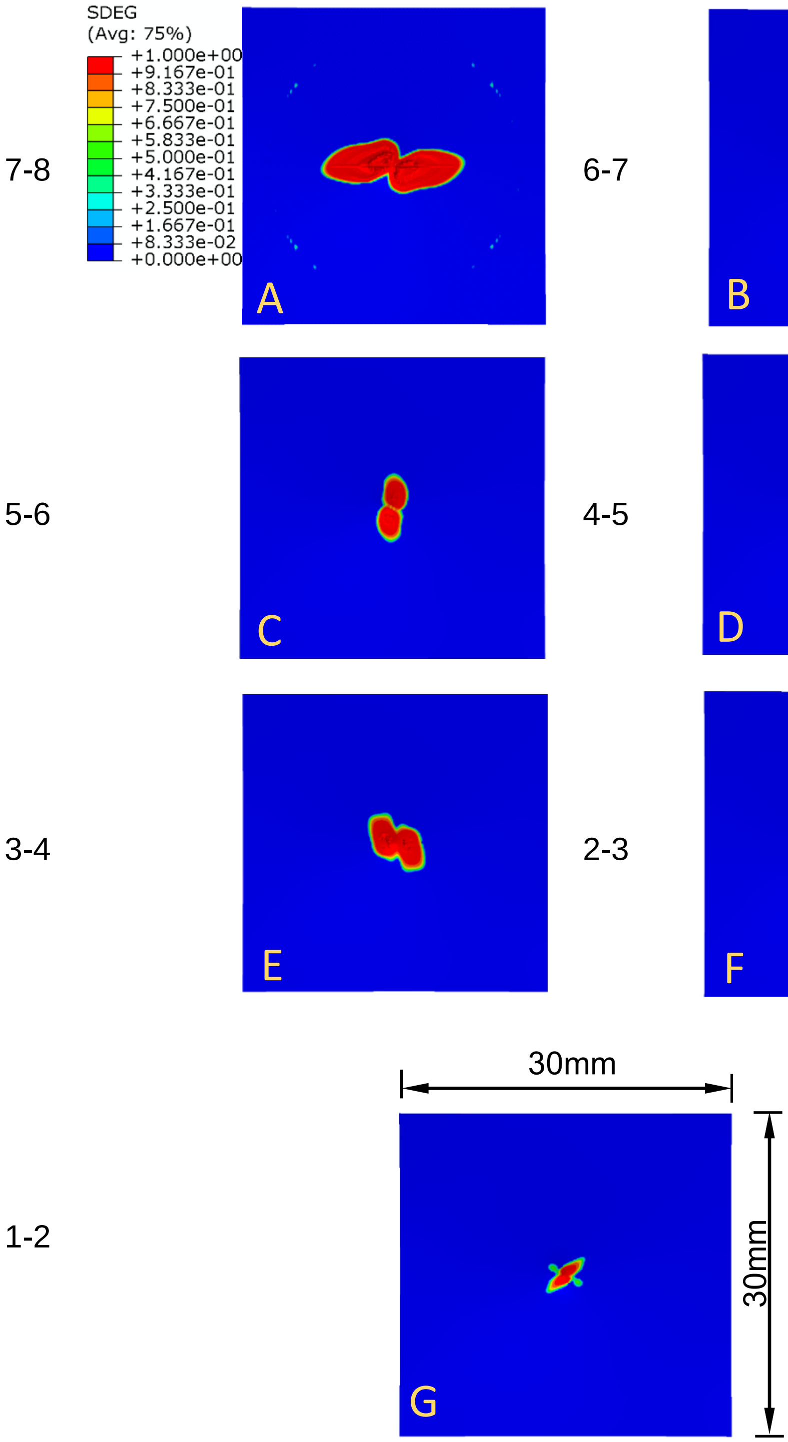

Figure 7.10: Delamination area between different adjacent plies of laminate under dynamic load with 4 mm impactor. (A) Between 7th and 8th plies. (B) Between 6th and 7th plies (C) Between 5th and 6th plies (D) Between 4th and 5th plies (E) Between 3rd and 4th plies (F) Between 2nd and 3rd plies (G) Between 1st and 2nd plies.

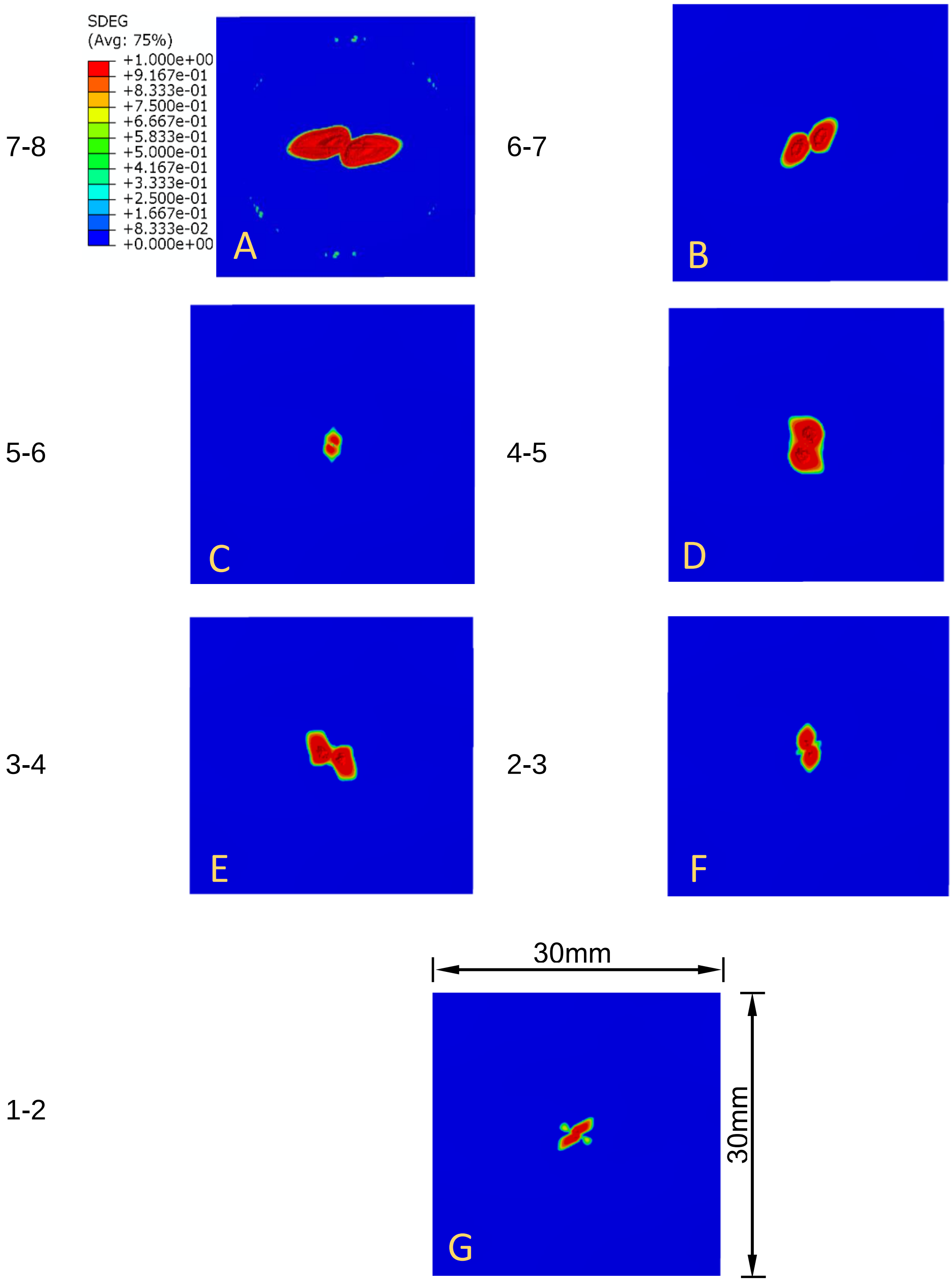

Figure 7.11: Delamination area between different adjacent plies of laminate under dynamic load with 1 mm impactor. (A) Between 7th and 8th plies. (B) Between 6th and 7th plies (C) Between 5th and 6th plies (D) Between 4th and 5th plies (E) Between 3rd and 4th lies (F) Between 2nd and 3rd lies (G) Between 1st and 2nd plies.

7.5 Comparison between experimental and simulation work

To validate modelling results that obtained from ABAQUS, a comparison of these results with the experimental results at same condition has been made for both force-time curves and displacement-time curves with three impactor diameters.

7.5.1 Force-displacement behaviour

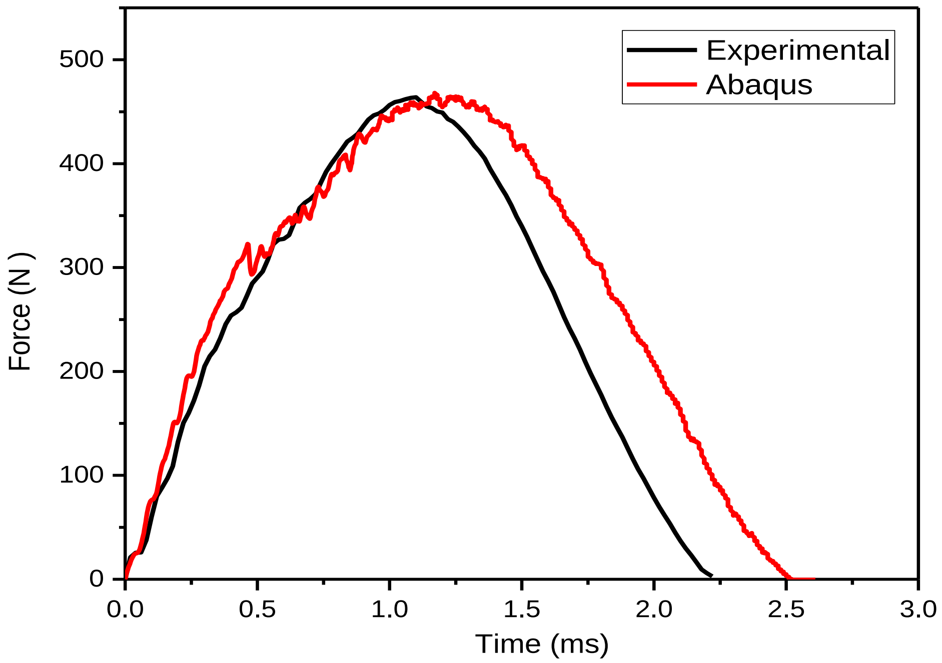

Figure 7.12: Comparison between experimental and numerical force-time curve of 4mm indenter.

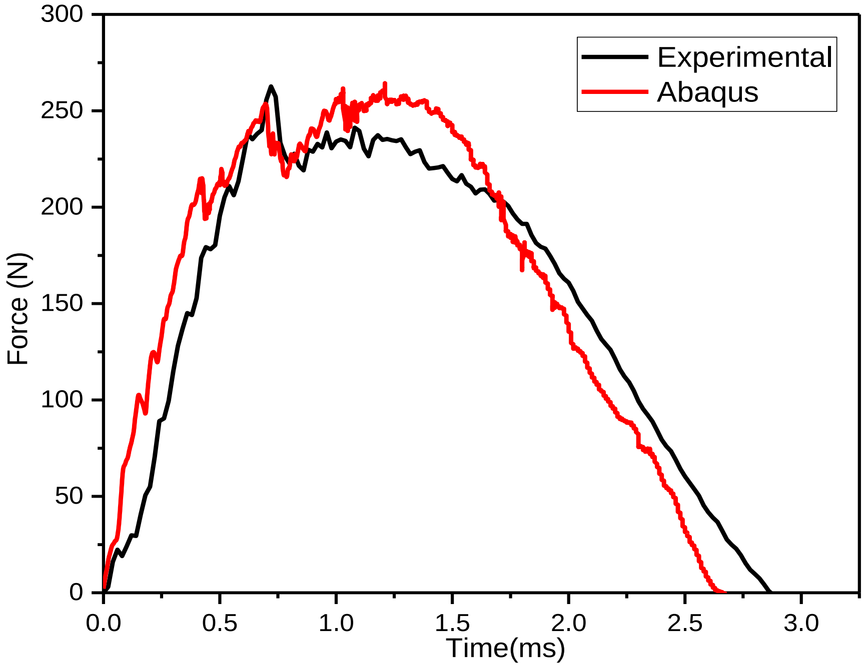

Figure 7.13: Comparison between experimental and numerical force-time curve of 2mm indenter.

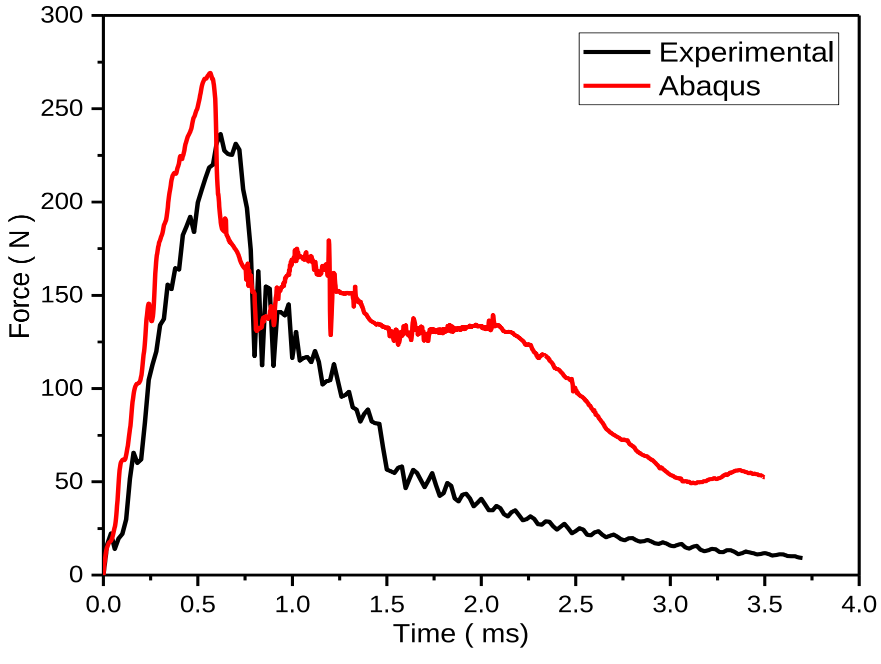

Figure 7.14: Comparison between experimental and numerical force-time curve of 1mm indenter.

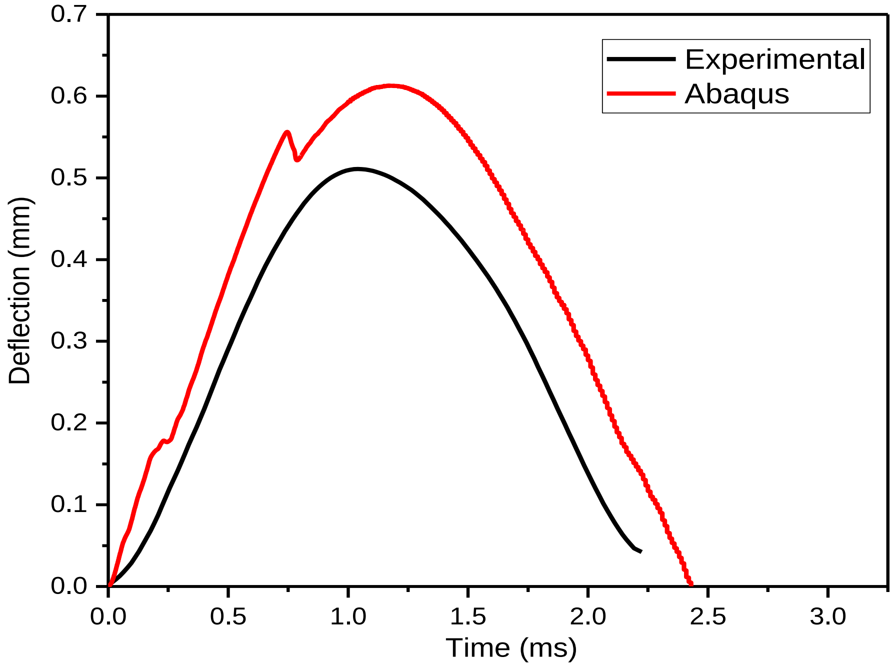

Figure 7.15: Comparison between experimental and numerical deflection-time curve of 4mm indenter.

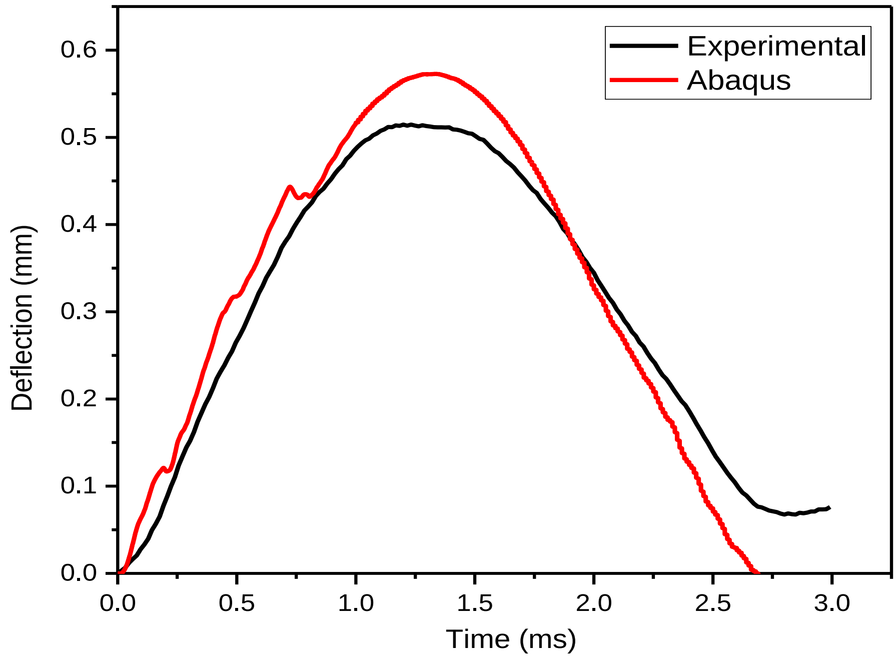

Figure 7.16: Comparison between experimental and numerical deflection-time curve of 2mm indenter.

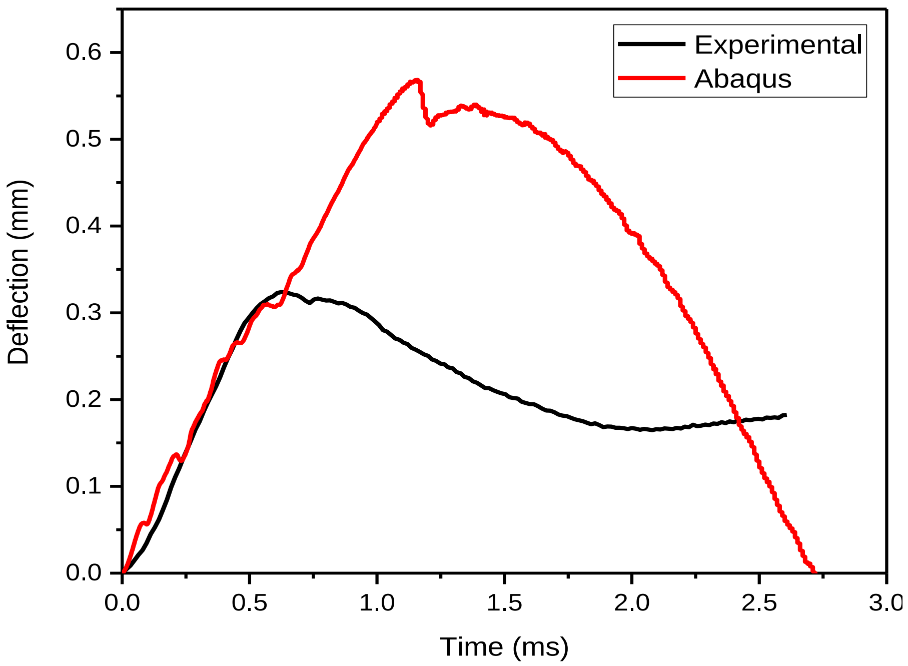

Figure 7.17: Comparison between experimental and numerical deflection-time curve of 1mm indenter.

From Figure 7.12 to Figure 7.17, the time of impact increase as the impactor size decrease (2.25 ms for 4mm and 2.8 for 2mm). In a 1mm case, the time of impact is more than 3.5 ms as time was consumed by the penetration. The force-time curves for all three impactors in the modelling work agree very well with the experimental work and capture all the features in these figures. The maximum force of 1, 2, and 4 mm are 480,250,250 n respectively. The DTL are 306,203 for 2 and 4mm impactor. On the other hand, there is no DTL for 1mm case and that has the same behaviour of the static case as the failure happened immediately. The other difference between experimental and modelling result in 1mm case that the force at the end of impact time is higher in the modelling part as ABAQUS did not capture the full penetration which happened in the experimental part.

7.5.2 Internal damage

For the delamination area, the modelling result agrees with the experimental result in term of the length of the major axis of the delaminated area and the shape of that are expected of the space between the two parts of number eight figure.

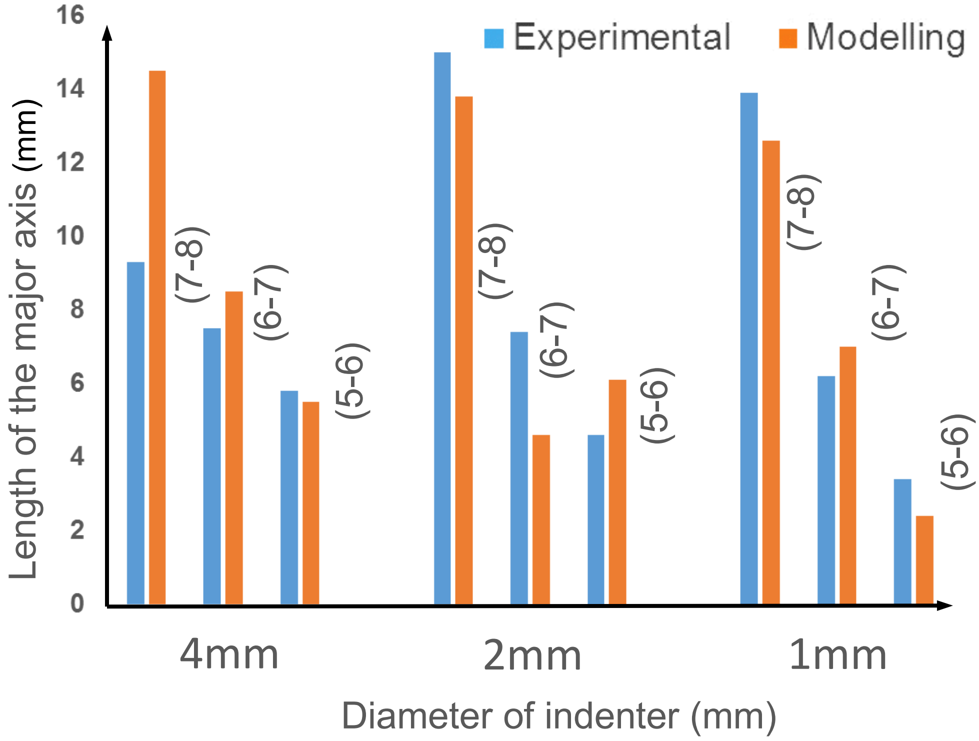

Figure 7.18: Comparison between experimental and modelling size of delamination for dynamic loading.

As shown in Figure 7.18, the comparison between experimental and modelling work has been conducted on the tension side area of the laminate as it is most effected damage area. The modelling work is well predicted the delamination area on the tension side. However, the delamination between the 7^{th} and 8^{th} plies is over estimated in 4 mm indenter.

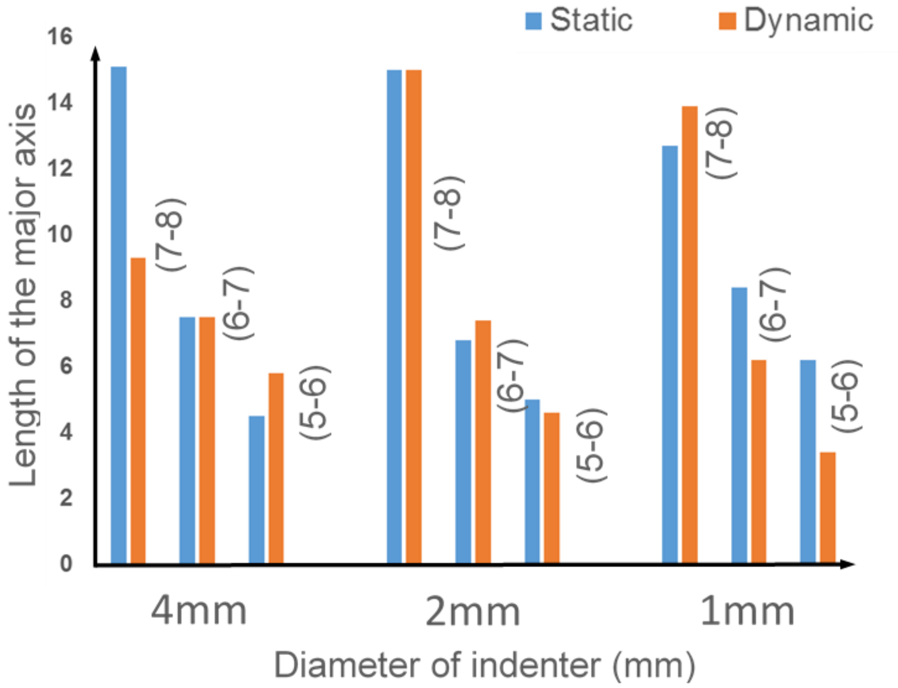

Figure 7.19: Comparison between static and dynamic loading size of delamination for experimental test.

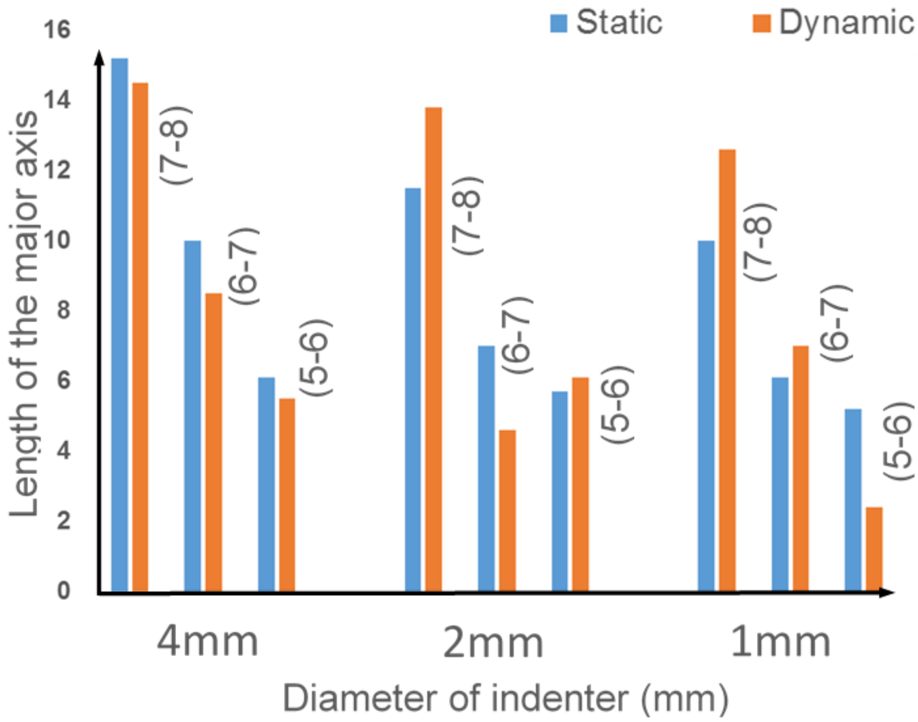

Figure 7.20: Comparison between static and dynamic loading size of delamination for Modelling.

As shown in Figure 7.19 and Figure 7.20, for 4mm and 2mm diameter, the delamination area of the low-velocity load increase towards the centre compared with the static case. This explains the fact that the dominant mode of delamination is mode II or shear mode which increase near to the centre of the laminate.The mode of delamination in the outermost layer is mode I. This is not the case for the 1mm diameter because most of the dynamic energy consume in fibre fracture rather than delamination. The energy balance is shown in figureFigure 7.21.

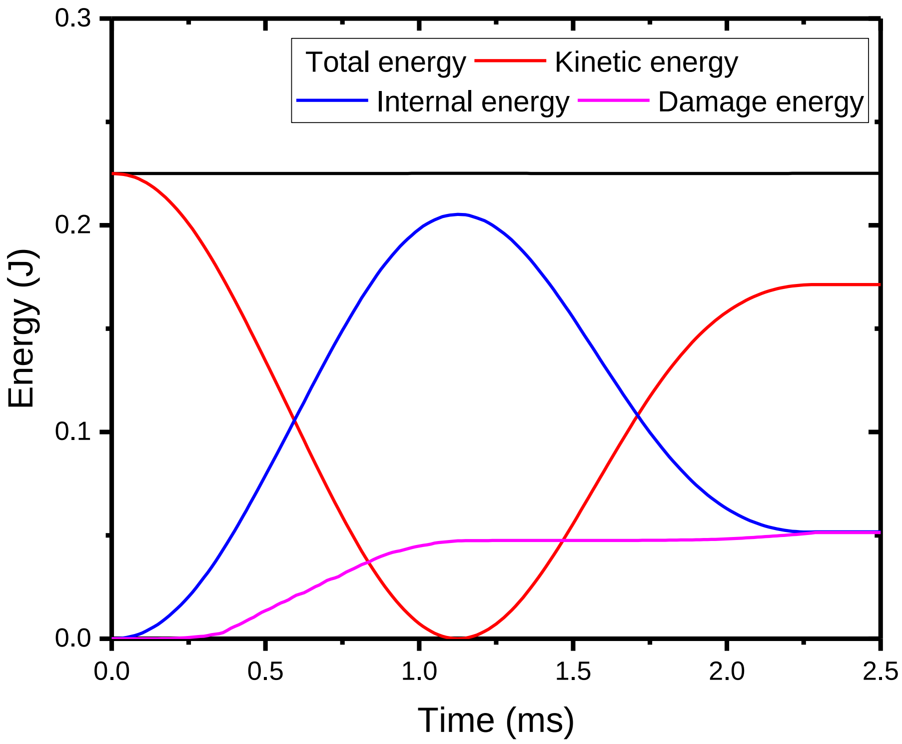

Figure 7.21: Energy balance of the model under dynamic load.

The figure shows that the total energy is constant but it changes in different shapes. The internal energy is not zero after the impact because some energy consumed as damage energy. The same behaviour for dynamic energy of the impact which should be the same energy at the start of contact (0.225J).

Chapter 8 Conclusion and future work

This thesis aims to give further knowledge on the impact behaviour and damage mechanisms of CFRP laminates under quasi-static and low velocity impact. This project also aims to explore the effect of internal damage such as delamination and matrix cracking on the force deflection curve. This chapter summarises the main conclusions derived from the experimental and simulation investigations that have been conducted in this thesis. Further work continues this study is then recommended.

8.1 Summary

An experimental and simulation investigation of the damage mechanisms and impact response of composite laminates under quasi-static and low velocity impact has been conducted. A dominant damage mode, which is delamination, and a delamination threshold load (DTL) are considered to be the most important factors to characterise in both types of impact of CFRPs, which have been a particular focus in this thesis. The following conclusions can be derived from quasi-static and low velocity related investigation results:

- The force indentation curve of the simulation part of this work for thick laminates agreed well with the Hertz contact law, while for thinner laminates it has been shown that the global deflection due to bending dominates. This behaviour has been demonstrated for isotropic and composite materials.
- A delamination threshold load is clearly observed for the quasi static loading case where the slope of the force-displacement curve changes. However, this effect is not always quite so clear for the low velocity impact case.
- The effect of the diameter of the indenter on the force curve is clear for both cases; quasi-static and lo velocity impact. As the diameter increases, the force and displacement of the laminates increases.

An optical microscopy and micro-CT technique has been developed to obtain a complete damage picture of the full-scale specimen for comparison with simulation.

The effect of the diameter on the size of the delamination area is clear and has the same effect as load and displacement i.e. as the diameter increases, the delamination increases.

At the same energy level, the size of the delamination area is bigger for the quasi-static impact than the low velocity impact with the same diameter of indenter.

The existence of delamination in certain areas between two adjacent plies increases the flexibility of the laminate and relieves local stresses. Thus, there is often no evidence of delamination between the next adjacent plies.

The initial and the final fibre breakage are related to transient load dips and the ultimate load drop on the deflection load curve, respectively.

The proposed cohesive zone-based modelling scheme for interacting damage modes can work for modelling the interaction between more than one types of damage i.e. the inter-laminar and the intra-laminar damage under a different type of loading. This strategy has proven to be capable of predicting the damage that induces a degradation in a composite laminates stiffness.

The simulation result shows high sensitivity to model setup and some parameters should be selected carefully and calibrated by trial and error such as the stiffness of the cohesive layer.

The shape of delamination strongly depends on the orientation of fibres of the two adjacent plies, especially the lower one. The delamination propagates in the direction of the fibre of the bottom ply. The delamination propagation ends along the fibre direction of the higher ply. Thus, both fibre directions are important in determining the final shape of the delamination.

The meso-level numerical models for simulation of damage of composite laminates, which has been used in this work, could be a good tool to reduce the cost and time of doing the experimental test and this will reduce product design time.

For the quasi-static load, the difference between the load dips and the ultimate load decreases as the diameter of the indenter decreases. This difference is zero in the 1mm indenter diameter.

As the diameter of the indenter increases or the ratio of laminate to indenter radius increase, the force-displacement curve shows a recovery after the first fibre crack. This means that the laminate sustains more load after the first fibre crack. This ability decreases as the indenter diameter decreases and finally, as in the 1mm case, there is no recovery after the first drop.

8.2 Conclusion

The novelty of the work conducted in this thesis has been to explore the change in failure mechanism in carbon fibre reinforced polymer composites when the key dimensions of the impactor geometry are in the range of the composite thickness. It was expected that the localised stress field generated would be modified when these two length scales are comparable and this was found to be the case both experimentally and computationally. A composite of thickness 1mm has been considered. The effect of a number of hemi-spherical indenters of radii 1mm, 2mm and 4mm have been investigated, and a change in mechanism has been observed across this range. Delamination dominates the failure mechanism for the 2mm and 4mm indenters, whereas localised failure of the matrix is more important for the 1mm case, where complete penetration was observed in the dynamic impact case. Close inspection of the internal damage using micro x-ray computer tomography has allowed a novel comparison with finite element cohesive zone models. Both demonstrate that delamination failure initially occurs underneath the impact between the two lowest plies (furthest beneath the impactor). This initial delamination area grows to the largest damage area, with delamination also spreading to the higher plies (nearer to the indenter) as the damage process continues. This corresponds well with computational results is the delamination zones rotate with the ply orientation, but the effect of fibre orientation can also be clearly seen in the delineation of the delaminated region morphologies. This suggests that crack propagation is easier along the fibres than across them, a feature that is not currently incorporated into cohesive zone models. This work suggests that alternative criteria for non-visible damage assessment need to be used if there is the possibility of low velocity impact by projectiles with dimensions comparable to the composite thickness.

8.3 Recommended work.

Damage characterisation of composite laminates under impact load is a complicated issue and it is a big challenge to industry. Although significant research has been conducted to develop further knowledge in this field, there are still many areas that need to be investigated further. The following points are recommended for future work related to this project.

Experimental CT-scan tests at different times of quasi-static test to investigate the initiation and propagation of the delamination. These tests should be conducted before and after the DTL to show the effect of DTL on propagation of delamination. One of these tests should be at low force to show the matrix cracking in early stage of loading.

In term of modelling part, the cohesive zone model (CZM) can be further developed to simulate the interaction between the matrix and fibre to incorporate the effects of fibre orientation on preferred crack propagation direction as observed. This will help the matrix crack initiation in early load stage before reaching the ply interface and delamination initiation.

Using the new generation of the VG studio software to examine the intra-laminar damage mode i.e. the interface between the matrix and the fibre within the ply. This will help to understand the matrix cracking by visualizing the path of the matrix cracking.

In this work, the behaviour of CFRP laminates under an impact and quasi-static loads has been conducted. The behaviour of this type of laminates under multiple loads of both type of loading needs to be investigated.

Appendix A: Derivation of composite matrices

The state of stress at a certain point in the space can be represented as:

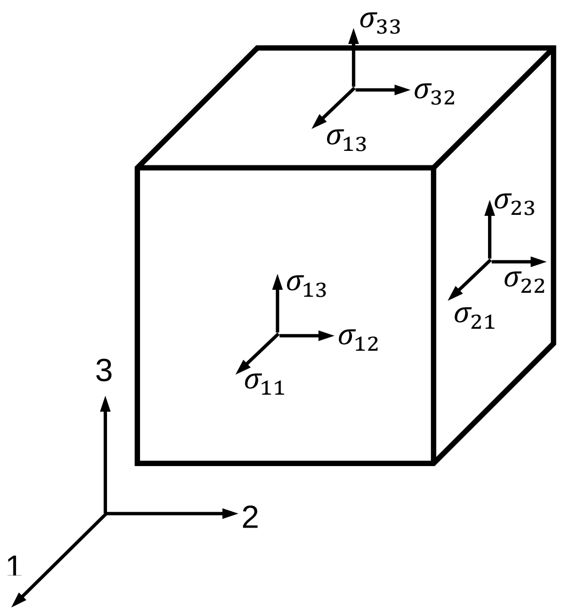

Figure A.1: State of stress at a point in three dimensions [3]

$$\begin{bmatrix}\sigma_{11}\\ \sigma_{22}\\ \sigma_{33}\\ \sigma_{23}\\ \sigma_{31}\\ \sigma_{12}\\ \sigma_{32}\\ \sigma_{13}\\ \sigma_{21}\end{bmatrix} = \begin{bmatrix} C_{1111} & C_{1122} & C_{1133} & C_{1123} & C_{1131} & C_{1112} & C_{1132} & C_{1113} & C_{1121}\\ C_{2211} & C_{2222} & C_{2233} & C_{2223} & C_{2231} & C_{2212} & C_{2232} & C_{2213} & C_{2221}\\ C_{3311} & C_{3322} & C_{3333} & C_{3323} & C_{3331} & C_{3312} & C_{3332} & C_{3313} & C_{3321}\\ C_{2311} & C_{2322} & C_{2333} & C_{2323} & C_{2331} & C_{2312} & C_{2332} & C_{2313} & C_{2321}\\ C_{3111} & C_{3122} & C_{3133} & C_{3123} & C_{3131} & C_{3112} & C_{3132} & C_{3113} & C_{3121}\\ C_{1211} & C_{1222} & C_{1233} & C_{1223} & C_{1231} & C_{1212} & C_{1232} & C_{1213} & C_{1221}\\ C_{3211} & C_{3222} & C_{3233} & C_{3223} & C_{3231} & C_{3212} & C_{3232} & C_{3213} & C_{3221}\\ C_{1311} & C_{1322} & C_{1333} & C_{1323} & C_{1331} & C_{1312} & C_{1332} & C_{1313} & C_{1321}\\ C_{2111} & C_{2122} & C_{2133} & C_{2123} & C_{2131} & C_{2112} & C_{2132} & C_{2113} & C_{2121} \end{bmatrix} \begin{bmatrix}\epsilon_{11}\\ \epsilon_{22}\\ \epsilon_{33}\\ \epsilon_{23}\\ \epsilon_{31}\\ \epsilon_{12}\\ \epsilon_{32}\\ \epsilon_{13}\\ \epsilon_{21}\end{bmatrix} \quad \text{(A.1)}$$

Due to the symmetry of stress and strain is:

$$\sigma_{ij} = \sigma_{ji} \quad and \;\; \epsilon_{ij} = \epsilon_{ji}$$

This symmetry leads to:

$$\begin{bmatrix} \sigma_1 \\ \sigma_2 \\ \sigma_3 \\ \tau_4 \\ \tau_5 \\ \tau_6 \end{bmatrix} = \begin{bmatrix} C_{11} & C_{12} & C_{13} & C_{14} & C_{15} & C_{16} \\ C_{21} & C_{22} & C_{23} & C_{24} & C_{25} & C_{26} \\ C_{31} & C_{32} & C_{33} & C_{34} & C_{35} & C_{36} \\ C_{41} & C_{42} & C_{43} & C_{44} & C_{45} & C_{46} \\ C_{51} & C_{52} & C_{53} & C_{54} & C_{55} & C_{56} \\ C_{61} & C_{62} & C_{63} & C_{64} & C_{65} & C_{66} \end{bmatrix} \begin{bmatrix} \epsilon_1 \\ \epsilon_2 \\ \epsilon_3 \\ \gamma_4 \\ \gamma_5 \\ \gamma_6 \end{bmatrix} \tag{A.2}$$

Where: $\sigma_{11} = \sigma_1$, $\sigma_{22} = \sigma_2$, $\sigma_{33} = \sigma_3$, $\sigma_{12} = \tau_6$, $\sigma_{31} = \tau_5$, $\sigma_{23} = \tau_4$

$$\begin{matrix} C_{1111} = C_{11} & C_{1122} = C_{12} & C_{1133} = C_{13} & C_{1123} = C_{14} & C_{1131} = C_{15} & C_{1112} = C_{16} \\ C_{2211} = C_{21} & C_{2222} = C_{22} & C_{2233} = C_{23} & C_{2223} = C_{24} & C_{2231} = C_{25} & C_{2212} = C_{26} \\ C_{3311} = C_{31} & C_{3322} = C_{32} & C_{3333} = C_{33} & C_{3323} = C_{34} & C_{3331} = C_{35} & C_{3312} = C_{36} \\ C_{2311} = C_{41} & C_{2322} = C_{42} & C_{2333} = C_{43} & C_{2323} = C_{44} & C_{2331} = C_{45} & C_{2312} = C_{46} \\ C_{3111} = C_{51} & C_{3122} = C_{52} & C_{3133} = C_{53} & C_{3123} = C_{54} & C_{3131} = C_{55} & C_{3112} = C_{56} \\ C_{1211} = C_{61} & C_{1222} = C_{62} & C_{1233} = C_{63} & C_{1223} = C_{64} & C_{1231} = C_{65} & C_{1212} = C_{66} \end{matrix}$$

For an orthotropic materials which have three perpendicular planes of symmetry i.e at any point in the material, has different properties in three different directions.

Under plane stress load:

$$\sigma_3 = 0 \quad \tau_5 = 0 \quad \tau_4 = 0$$

For local coordinates, equation (A.2) will be:

$$\begin{bmatrix} \sigma_1 \\ \sigma_2 \\ \sigma_3 \\ \tau_4 \\ \tau_5 \\ \tau_6 \end{bmatrix} = \begin{bmatrix} C_{11} & C_{12} & C_{13} & 0 & 0 & 0 \\ C_{21} & C_{22} & C_{23} & 0 & 0 & 0 \\ C_{31} & C_{32} & C_{33} & 0 & 0 & 0 \\ 0 & 0 & 0 & C_{44} & 0 & 0 \\ 0 & 0 & 0 & 0 & C_{55} & 0 \\ 0 & 0 & 0 & 0 & 0 & C_{66} \end{bmatrix} \begin{bmatrix} \epsilon_1 \\ \epsilon_2 \\ \epsilon_3 \\ \gamma_4 \\ \gamma_5 \\ \gamma_6 \end{bmatrix} \tag{A.3}$$

$$\sigma_1 = C_{11}\epsilon_1 + C_{12}\epsilon_2 + C_{13}\epsilon_3$$

$$\sigma_2 = C_{12}\epsilon_1 + C_{22}\epsilon_2 + C_{23}\epsilon_3$$

$$0 = C_{13}\epsilon_1 + C_{23}\epsilon_2 + C_{33}\epsilon_3$$

For in plane case, $\epsilon_3 = 0$

Equation (A.3) we will obtain:

$$\sigma_1 = \left(C_{11} - \frac{C_{13}C_{13}}{C_{33}}\right)\epsilon_1 + \left(C_{12} - \frac{C_{13}C_{23}}{C_{33}}\right)\epsilon_2 = Q_{11}\epsilon_1 + Q_{12}\epsilon_2$$

$$\sigma_1 = \left(C_{12} - \frac{C_{23}C_{13}}{C_{33}}\right)\epsilon_1 + \left(C_{22} - \frac{C_{23}C_{23}}{C_{33}}\right)\epsilon_2 = Q_{12}\epsilon_1 + Q_{22}\epsilon_2$$

$$\tau_6 = C_{66}\gamma_6 + Q_{66}\gamma_6$$

Or:

$$\begin{bmatrix} \sigma_1 \\ \sigma_2 \\ \tau_6 \end{bmatrix} = \begin{bmatrix} Q_{11} & Q_{12} & 0 \\ Q_{21} & Q_{22} & 0 \\ 0 & 0 & Q_{66} \end{bmatrix} \begin{bmatrix} \varepsilon_1 \\ \varepsilon_2 \\ \gamma_6 \end{bmatrix} \qquad \text{(A.4)}$$

And:

$$\begin{bmatrix} \varepsilon_1 \\ \varepsilon_2 \\ \gamma_6 \end{bmatrix} = \begin{bmatrix} S_{11} & S_{12} & 0 \\ S_{21} & S_{22} & 0 \\ 0 & 0 & S_{66} \end{bmatrix} \begin{bmatrix} \sigma_1 \\ \sigma_2 \\ \tau_6 \end{bmatrix} \qquad \text{(A.5)}$$

The previous equation can be expressed in term of engineering constant as below:

$$S_{11} = \frac{1}{E_1} \quad S_{22} = \frac{1}{E_2} \quad S_{12} = S_{21} = -\frac{\nu_{12}}{E_1} \quad -\frac{\nu_{21}}{E_2} \quad S_{66} = \frac{1}{G_{12}}$$

Where:

$$Q_{11} = \frac{E_1}{1 - \nu_{12}\nu_{21}}$$

$$Q_{22} = \frac{E_2}{1 - \nu_{12}\nu_{21}}$$

$$Q_{12} = Q_{21} = \frac{\nu_{21}E_1}{1 - \nu_{12}\nu_{21}} = \frac{\nu_{21}E_2}{1 - \nu_{12}\nu_{21}} \qquad \text{(A.6)}$$

$$Q_{66} = G_{12}$$

$$
\begin{gathered}
\overline{Q}_{11} = c^4 Q_{11} + s^4 Q_{22} + 2c^2 s^2 Q_{12} + 4c^2 s^2 Q_{66} \\
\overline{Q}_{12} = (Q_{11} + Q_{22} - 4Q_{66})c^2 s^2 + +(c^4 + s^2)Q_{12} \\
Q_{22} = s^4 Q_{11} + c^4 Q_{22} + (Q_{12} + 2Q_{66})c^2 s^2 \\
Q_{16} = (Q_{11} - Q_{12} - 2Q_{66})c^3 s - (Q_{22} - Q_{12} - 2Q_{66})s^3 c \\
Q_{26} = (Q_{11} - Q_{12} - 2Q_{66})s^3 c - (Q_{22} - Q_{12} - 2Q_{66})c^3 s \\
Q_{66} = (Q_{11} + Q_{22} - 2Q_{12} - 2Q_{66})c^2 s^2 + Q_{66}(c^4 + s^4)
\end{gathered} \tag{A.7}
$$

In composite materials, the distribution of stresses within a laminate varies from layer to layer discontinuously. For this reason, we need to know the relation between the applied forces and moments and the laminate deformations. The load per unit length acting on a point distance z from the reference plane as shown in Figure (2.5). Load and moment equation can be written as

$$
N_x^k = \int_{-t/2}^{t/2} \sigma_x dz \qquad N_y^k = \int_{-t/2}^{t/2} \sigma_y dz \qquad N_s^k = \int_{-t/2}^{t/2} \tau_s dz \tag{A.8}
$$

And moments are:

$$
M_x^k = \int_{-t/2}^{t/2} \sigma_x z dz \qquad M_y^k = \int_{-t/2}^{t/2} \sigma_y z dz \qquad M_s^k = \int_{-t/2}^{t/2} \tau_s z dz \tag{A.9}
$$

Where: t ≡ layer thickness

N_x^k, N_y^k ≡ Normal force per unit length for a layer k

N_s^k ≡ Shear force per unit length for a layer k

M_x^k, M_y^k ≡ Bending moment per unit length for a layer k

M_s^k ≡ Twisting moment per unit length for a layer k

$$
\begin{bmatrix} N_x \\ N_y \\ N_s \end{bmatrix} = \sum_{k=1}^{n} \left[\begin{bmatrix} Q_{xx} & Q_{xy} & Q_{xs} \\ Q_{yx} & Q_{yy} & Q_{ys} \\ Q_{sx} & Q_{sy} & Q_{ss} \end{bmatrix}_k \begin{bmatrix} \epsilon_x^0 \\ \epsilon_y^0 \\ \gamma_s^0 \end{bmatrix}_k \int_{z_{k-1}}^{z_k} dz + \begin{bmatrix} Q_{xx} & Q_{xy} & Q_{xs} \\ Q_{yx} & Q_{yy} & Q_{ys} \\ Q_{sx} & Q_{sy} & Q_{ss} \end{bmatrix}_k \begin{bmatrix} k_x \\ k_y \\ k_s \end{bmatrix} \int_{z_{k-1}}^{z_k} z dz \right] \tag{A.10}
$$

And:

$$\begin{bmatrix} M_x \\ M_y \\ M_s \end{bmatrix} = \sum_{k=1}^{n} \left[\begin{bmatrix} Q_{xx} & Q_{xy} & Q_{xs} \\ Q_{yx} & Q_{yy} & Q_{ys} \\ Q_{sx} & Q_{sy} & Q_{ss} \end{bmatrix}_k \begin{bmatrix} \epsilon_x^0 \\ \epsilon_y^0 \\ \gamma_s^0 \end{bmatrix}_k \int_{z_{k-1}}^{z_k} zdz + \begin{bmatrix} Q_{xx} & Q_{xy} & Q_{xs} \\ Q_{yx} & Q_{yy} & Q_{ys} \\ Q_{sx} & Q_{sy} & Q_{ss} \end{bmatrix}_k \begin{bmatrix} k_x \\ k_y \\ k_s \end{bmatrix} \int_{z_{k-1}}^{z_k} z^2 dz \right] \tag{A.11}$$

$$[N]_{x,y} = \left[\sum_{k=1}^{n} [Q]_{x,y}^{k} \int_{z_{k-1}}^{z_k} dz \right] [\epsilon^0]_{x,y} + \left[\sum_{k=1}^{n} [Q]_{x,y}^{k} \int_{z_{k-1}}^{z_k} zdz \right] [k]_{x,y} \tag{A.12}$$

Then:

$$[N]_{x,y} = \left[\frac{1}{2} \sum_{k=1}^{n} [Q]_{x,y}^{k} (z_k - z_{k-1}) \right] [\epsilon^0]_{x,y} + \left[\frac{1}{2} \sum_{k=1}^{n} [Q]_{x,y}^{k} (z_k^2 - z_{k-1}^2) \right] [k]_{x,y} \tag{A.13}$$

$$[M]_{x,y} = \left[\sum_{k=1}^{n} [Q]_{x,y}^{k} (z_k^2 - z_{k-1}^2) \right] [\epsilon^0]_{x,y} + \left[\frac{1}{3} \sum_{k=1}^{n} [Q]_{x,y}^{k} (z_k^3 - z_{k-1}^3) \right] [k]_{x,y} \tag{A.14}$$

Or

$$[N]_{x,y} = [A]_{x,y} [\epsilon^0]_{x,y} + [B]_{x,y} [k]_{x,y} \tag{A.15}$$

$$[M]_{x,y} = [B]_{x,y} [\epsilon^0]_{x,y} + [D]_{x,y} [k]_{x,y} \tag{A.16}$$

where

$$\begin{aligned} A_{ij} &= \left[\sum_{k=1}^{n} [Q]_{ij}^{k} (z_k - z_{k-1}) \right] \\ B_{ij} &= \left[\frac{1}{2} \sum_{k=1}^{n} [Q]_{ij}^{k} (z_k^2 - z_{k-1}^2) \right] \\ D_{ij} &= \left[\frac{1}{3} \sum_{k=1}^{n} [Q]_{ij}^{k} (z_k^3 - z_{k-1}^3) \right] \end{aligned} \tag{A.17}$$

In full notation this becomes

$$\begin{bmatrix} N_x \\ N_y \\ N_s \end{bmatrix} = \begin{bmatrix} A_{xx} & A_{xy} & A_{xs} \\ A_{yx} & A_{yy} & A_{ys} \\ A_{sx} & A_{sy} & A_{ss} \end{bmatrix} \begin{bmatrix} \epsilon_x^0 \\ \epsilon_y^0 \\ \gamma_s^0 \end{bmatrix} + \begin{bmatrix} B_{xx} & B_{xy} & B_{xs} \\ B_{yx} & B_{yy} & B_{ys} \\ B_{sx} & B_{sy} & B_{ss} \end{bmatrix} \begin{bmatrix} k_x \\ k_y \\ k_s \end{bmatrix} \quad \text{(A.18)}$$

$$\begin{bmatrix} M_x \\ M_y \\ M_s \end{bmatrix} = \begin{bmatrix} B_{xx} & B_{xy} & B_{xs} \\ B_{yx} & B_{yy} & B_{ys} \\ B_{sx} & B_{sy} & B_{ss} \end{bmatrix} \begin{bmatrix} \epsilon_x^0 \\ \epsilon_y^0 \\ \gamma_s^0 \end{bmatrix} + \begin{bmatrix} D_{xx} & D_{xy} & D_{xs} \\ D_{yx} & D_{yy} & D_{ys} \\ D_{sx} & D_{sy} & D_{ss} \end{bmatrix} \begin{bmatrix} k_x \\ k_y \\ k_s \end{bmatrix} \quad \text{(A.19)}$$

For the laminate that used in this thesis, the derivation of its properties as below:

E_1= 300 Gpa. E_2= E_3=6.37 Gpa. ν_{12} =0.3, ν_{21} =0.0105, G_{12}=3.9.

From equation (A.6)

$$[Q] = \begin{bmatrix} 301 & 3.1 & 0 \\ 3.1 & 10.3 & 0 \\ 0 & 0 & 3.9 \end{bmatrix}$$

The laminate used in this thesis has $(0/45/90/-45)_s$

The A, B, and D matrices for this laminate can be calculated based on the laminate thickness and its consequence. For 1mm thickness and previous layup, the distance for each lamina will be as shown:

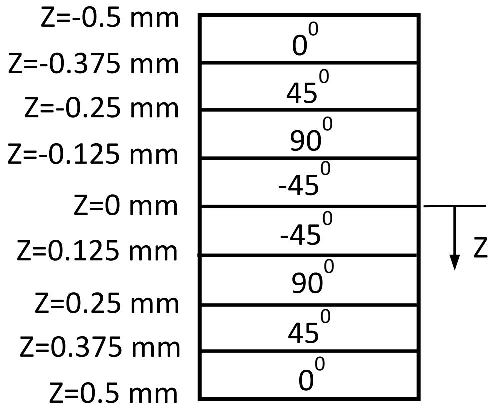

Thus, the A, B, D matrices for this laminate based on equation (A.17) will be:

$$[A] = \begin{bmatrix} 0.119 & 0.03928 & 0 \\ 0.03928 & 0.119 & 0 \\ 0 & 0 & 0.04 \end{bmatrix}$$

$$[B] = \begin{bmatrix} 0 & 0 & 0 \\ 0 & 0 & 0 \\ 0 & 0 & 0 \end{bmatrix}$$

$$[D] = \begin{bmatrix} 16.76 & 2.143 & 1.703 \\ 2.143 & 5.41 & 1.703 \\ 1.703 & 1.703 & 2.21 \end{bmatrix}$$

C=1, 0.707, 0, 0.707 and s= 0,0707,1,-0.707 respectively. Thus,

From equation (A.7) :

$$[\bar{Q}]_0 = \begin{bmatrix} 301 & 3.1 & 0 \\ 3.1 & 10.3 & 0 \\ 0 & 0 & 3.9 \end{bmatrix}$$

$$[\bar{Q}]_{90} = \begin{bmatrix} 10.3 & 3.1 & 0 \\ 3.1 & 300.1 & 0 \\ 0 & 0 & 3.9 \end{bmatrix}$$

$$[\bar{Q}]_{45} = \begin{bmatrix} 83.26 & 76.2 & 72.65 \\ 76.2 & 83.26 & 72.65 \\ 72.65 & 72.65 & 76.265 \end{bmatrix}$$

$$[\bar{Q}]_{-45} = \begin{bmatrix} 83.26 & 76.2 & -72.65 \\ 76.2 & 83.26 & -72.65 \\ -72.65 & -72.65 & 76.265 \end{bmatrix}$$

Appendix B: Hertz contact law

$$z_1 = \left(\frac{r^2}{2R_1}\right) \qquad z_2 = \left(\frac{r^2}{2R_2}\right) \tag{B.1}$$

When point M and N touch each other

$$\delta - (w_1 + w_2) = z_1 + z_2 = \beta r^2 \tag{B.2}$$

where w1 and w2 are local vertical displacements of points N and M respectively, and β is a factor depends on the shape of body i.e for two spheres

$$\beta = \frac{r^2(R_1 + R_2)}{2R_1R_2} \tag{B.3}$$

Thus:

$$(w_1 + w_2) = \delta - \beta r^2 \tag{B.4}$$

$$w_1 = \left(\frac{1-\upsilon_1^2}{\pi E_1}\right) \iint q\, ds\, d\psi \qquad w_2 = \left(\frac{1-\upsilon_2^2}{\pi E_2}\right) \iint q\, ds\, d\psi \tag{B.5}$$

$$w_1 = \left(\frac{1-\upsilon_1^2}{\pi E_1}\right) \iint q\, ds\, d\psi \qquad w_2 = \left(\frac{1-\upsilon_2^2}{\pi E_2}\right) \iint q\, ds\, d\psi \tag{B.6}$$

substiuting equation (2.9) into (2.8) we will get:

$$w_1 + w_2 = (k_1 + k_2) \iint q \, ds \, d\psi \qquad \text{(B.7)}$$

Where:

$$k_1 = \left(\frac{1 - \upsilon_1^2}{\pi E_1}\right) \quad k_2 = \left(\frac{1 - \upsilon_2^2}{\pi E_2}\right) \qquad \text{(B.8)}$$

From eq (2.8) and (2.10):

$$\delta - \beta r^2 = (k_1 + k_2) \iint q \, ds \, d\psi \qquad \text{(B.9)}$$

If we assume that: $q_0 = Ka$

Where q0 is the pressure at the centre, thus $k = \frac{q_0}{a}$ $\int q \, ds = \frac{q_0}{a} A$

A is the area of contact and it is $\frac{1}{2}\pi(a^2 - r^2 \sin^2\psi)$.

Thus

$$\frac{\pi(k_1 + k_2)}{a} \int_0^{\frac{\pi}{2}} (a^2 - r^2 \sin^2\psi) \, d\psi = \delta - \beta r^2 \qquad \text{(B.10)}$$

$$\alpha = (k_1 + k_{2)} q_0 \frac{\pi^2 a}{2} \quad \text{and} \quad a = (k_1 + k_{2)} \frac{\pi^2 q_0}{4\beta} \qquad \text{(B.11)}$$

The sum of pressure of the contact area is the contact force thus:

$$\frac{q_0}{a}\frac{2}{3}\pi a^3 = P \quad \xrightarrow{\text{yields}} \quad q_0 = \frac{3P}{2\pi a^2} \tag{B.12}$$

For a special case: two sphere the value of $\beta = \frac{R_1+R_2}{2\,R_1R_2}$

Thus:

$$a = \sqrt[3]{\frac{3\pi}{4}\frac{P(k_1+k_2)\,R_1R_2}{(R_1+R_2)}}$$

(B.13)

$$\alpha = \sqrt[3]{\frac{9\pi^2}{16}\frac{P(k_1+k_2)^2\,(R_1+R_2)}{R_1R_2}}$$

Appendix C: CT Flowchart for Inspect

No.	**CT Acquisition**	**CT Reconstruction**
1	Put sample on turntable and adjust sample position and magnification to best view the region of interest.	When scan is completed, if you did not select to automatically reconstruct the CT volume, then open the *.XTEKCT file in CT-Pro.
2	Rotate sample to make sure all parts remain in view at all rotation angles. Reduce the magnification or reposition the sample on the sample holder if necessary	On the setup tab, use the automatic centre of rotation tool in CT-Pro to ensure sharp data.
3	Rotate sample to the angle which presents the greatest path length. Increase the kV until detail in the darkest areas of the image is visible. Keep darkest pixels > 10000.	Also on the setup tab, select the beam hardening correction, noise reduction and interpolation settings to use – test all if necessary.
3	Follow the filter guidelines to choose a suitable filter to reduce beam hardening. Adjust the current and detector exposure so that the unimpeded X-ray beam does not cause saturated grey levels (65535). Generally best keep below about 63000 to allow for noise	Select a starting angle to optimise the orientation of the sample within the CT volume.
4	Run the CT wizard to set up the scan and collect reference images. Choose the number of frames to average and the number of projection images to maximise signal to noise within your time constraints.	On the 3D CT tab, choose your volume of interest by marking areas on the 0 and 90 radiographs.
5	If you have scanned a similar item before, you can preselect your reconstruction parameters and choose to automatically reconstruct the CT volume on completion of scanning.	Save your reconstruction settings – this updates the *.XTEKCT file (or you can “Save As” a new file and Start the 3D CT reconstruction.
6	To analyse a previous dataset, make sure you use a PC other than the one the data is being stored to avoid missing data.	

References

1. Strong, A.B., *History of Composite Materials-opportunities and necessities.* Brigham Young University, 2002: p. 1-8.

2. Talreja, R. and C.V. Singh, *Damage and failure of composite materials*. 2012: Cambridge University Press.

3. Nolan, R.L., *Ubiquitous IT: The case of the Boeing 787 and implications for strategic IT research.* The Journal of Strategic Information Systems, 2012. **21**(2): p. 91-102.

4. Shen, Z., *Characterisation of Low Velocity Impact Response in Composite Laminates*. 2014, School of Engineering and Technology, University of Hertfordshire.

5. Davies, G. and X. Zhang, *Impact damage prediction in carbon composite structures.* International Journal of Impact Engineering, 1995. **16**(1): p. 149-170.

6. Zhang, X., *Impact damage in composite aircraft structures-experimental testing and numerical simulation.* Proceedings of the Institution of Mechanical Engineers, Part G: Journal of Aerospace Engineering, 1998. **212**(4): p. 245-259.

7. Zhang, X., F. Bianchi, and H. Liu, *Predicting low-velocity impact damage in composites by a quasi-static load model with cohesive interface elements.* The Aeronautical Journal, 2012. **116**(1186): p. 1367-1381.

8. Schoeppner, G. and S. Abrate, *Delamination threshold loads for low velocity impact on composite laminates.* Composites Part A: applied science and manufacturing, 2000. **31**(9): p. 903-915.

9. Olsson, R., M.V. Donadon, and B.G. Falzon, *Delamination threshold load for dynamic impact on plates.* International Journal of Solids and Structures, 2006. **43**(10): p. 3124-3141.

10. Abrate, S., *Impact on composite structures*. 2005: Cambridge university press.

11. Nettles, A.T., *Basic mechanics of laminated composite plates.* 1994.

12. Daniel, I.M. and O. Ishai, *Engineering Mechanics Of Composite Materials*. 2006: New work

Oxford.

13. Vasiliev, V.V. and E.V. Morozov, *Mechanics Of Advanced Composite Materials*.

14. Chen, P., J. Xiong, and Z. Shen, *Thickness effect on the contact behavior of a composite laminate indented by a rigid sphere.* Mechanics of Materials, 2008. **40**(4): p. 183-194.

15. Johnson, K., *Contact Mechanics, 452 pp.* Cambridge University, New York, 1985.

16. Timoshenko, S., J. Goodier, and H.N. Abramson, *Theory of elasticity.* Journal of Applied Mechanics, 1970. **37**: p. 888.

17. Abrate, S., *Modeling of impacts on composite structures.* Composite structures, 2001. **51**(2): p. 129-138.

18. Yang, S. and C. Sun, *Indentation law for composite laminates.* ASTM STP, 1982. **787**: p. 425-449.

19. Swanson, S.R., *Contact deformation and stress in orthotropic plates.* Composites Part a-Applied Science and Manufacturing, 2005. **36**(10): p. 1421-1429.

20. Turner, J., *Contact on a transversely isotropic half-space, or between two transversely isotropic bodies.* International Journal of Solids and Structures, 1980. **16**(5): p. 409-419.

21. Chen, P.H., J.J. Xiong, and Z. Shen, *Thickness effect on the contact behavior of a composite laminate indented by a rigid sphere.* Mechanics of Materials, 2008. **40**(4-5): p. 183-194.

22. Olsson, R., *Mass criterion for wave controlled impact response of composite plates.* Composites Part A: Applied Science and Manufacturing, 2000. **31**(8): p. 879-887.

23. Cantwell, W. and J. Morton, *The impact resistance of composite materials—a review.* composites, 1991. **22**(5): p. 347-362.

24. LLorca, J., et al., *Multiscale modeling of composites: toward virtual testing… and beyond.* JOM, 2013. **65**(2): p. 215-225.

25. Zohdi, T.I. and P. Wriggers, *An introduction to computational micromechanics*. 2008: Springer Science & Business Media.

26. Ullah, H., *Analysis of mechanical behaviour and damage of carbon fabric-reinforced composites in bending*. 2013, © Himayat Ullah.

27. Puck, A. and H. Schürmann, *Failure analysis of FRP laminates by means of physically based phenomenological models.* Composites Science and Technology, 1998. **58**(7): p. 1045-1067.

28. Tita, V., J. de Carvalho, and D. Vandepitte, *Failure analysis of low velocity impact on thin composite laminates: Experimental and numerical approaches.* Composite Structures, 2008. **83**(4): p. 413-428.

29. Chen, P.H., et al., *Failure mechanisms of laminated composites subjected to static indentation.* Composite Structures, 2006. **75**(1-4): p. 489-495.

30. Manual, A.U., *Version 6.10-1.* Dassault Systémes Simulia Corp., Providence, RI.

31. Gan, K.W., M.R. Wisnom, and S.R. Hallett, *Effect of high through-thickness compressive stress on fibre direction tensile strength of carbon/epoxy composite laminates.* Composites Science and Technology, 2014. **90**: p. 1-8.

32. Orifici, A., I. Herszberg, and R. Thomson, *Review of methodologies for composite material modelling incorporating failure.* Composite structures, 2008. **86**(1): p. 194-210.

33. Batra, R.C., G. Gopinath, and J.Q. Zheng, *Damage and failure in low energy impact of fiber-reinforced polymeric composite laminates.* Composite Structures, 2012. **94**(2): p. 540-547.

34. Rodríguez, M., et al., *A methodology to measure the interface shear strength by means of the fiber push-in test.* Composites Science and Technology, 2012. **72**(15): p. 1924-1932.

35. Amaro, A., P. Reis, and M. De Moura, *Delamination effect on bending behaviour in carbon–epoxy composites.* Strain, 2011. **47**(2): p. 203-208.

36. Hinton, M. and P. Soden, *Predicting failure in composite laminates: the background to the exercise.* Composites Science and Technology, 1998. **58**(7): p. 1001-1010.

37. Hashin, Z., *Analysis of cracked laminates: a variational approach.* Mechanics of materials, 1985. **4**(2): p. 121-136.

38. Nairn, J.A., *The strain energy release rate of composite microcracking: a variational approach.* Journal of Composite Materials, 1989. **23**(11): p. 1106-1129.

39. Hashin, Z., *Failure criteria for unidirectional fiber composites.* Journal of applied mechanics, 1980. **47**(2): p. 329-334.

40. Hoffman, O., *The brittle strength of orthotropic materials.* Journal of Composite Materials, 1967. **1**(2): p. 200-206.

41. Tsai, S.W. and E.M. Wu, *A general theory of strength for anisotropic materials.* Journal of composite materials, 1971. **5**(1): p. 58-80.

42. Chang, F.-K. and K.-Y. Chang, *A progressive damage model for laminated composites containing stress concentrations.* Journal of composite materials, 1987. **21**(9): p. 834-855.

43. Erdogan, F. and G. Sih, *On the crack extension in plates under plane loading and transverse shear.* Journal of basic engineering, 1963. **85**(4): p. 519-525.

44. Hill, R., *The mathematical theory of plasticity*. Vol. 11. 1998: Oxford university press.

45. Pipes, R.B. and B. Cole, *On the off-axis strength test for anisotropic materials1.* Journal of Composite Materials, 1973. **7**(2): p. 246-256.

46. Kachanov, L., *Time of the rupture process under creep conditions.* Isv. Akad. Nauk. SSR. Otd Tekh. Nauk, 1958. **8**: p. 26-31.

47. Matzenmiller, A., J. Lubliner, and R. Taylor, *A constitutive model for anisotropic damage in fiber-composites.* Mechanics of materials, 1995. **20**(2): p. 125-152.

48. Maimí, P., et al., *A continuum damage model for composite laminates: Part I–Constitutive model.* Mechanics of Materials, 2007. **39**(10): p. 897-908.

49. Hochard, C., et al., *Behaviour up to rupture of woven ply laminate structures under static loading conditions.* Composites Part A: Applied Science and Manufacturing, 2009. **40**(8): p. 1017-1023.

50. Ribeiro, M.L., V. Tita, and D. Vandepitte, *A new damage model for composite laminates.* Composite Structures, 2012. **94**(2): p. 635-642.

51. Zhang, Y. and C. Yang, *Recent developments in finite element analysis for laminated composite plates.* Composite Structures, 2009. **88**(1): p. 147-157.

52. Matthews, F.L., et al., *Finite element modelling of composite materials and structures*. 2000: Elsevier.

53. Esrail, F. and C. Kassapoglou, *An efficient approach for damage quantification in quasi-isotropic composite laminates under low speed impact.* Composites Part B: Engineering, 2014. **61**: p. 116-126.

54. Song, K., C.G. Dávila, and C.A. Rose, *Guidelines and parameter selection for the simulation of progressive delamination.* 2008.

55. de Moura, M. and A.T. Marques, *Prediction of low velocity impact damage in carbon-epoxy laminates.* Composites Part a-Applied Science and Manufacturing, 2002. **33**(3): p. 361-368.

56. Hou, J.P., et al., *Prediction of impact damage in composite plates.* Composites Science and Technology, 2000. **60**(2): p. 273-281.

57. Benzeggagh, M. and M. Kenane, *Measurement of mixed-mode delamination fracture toughness of unidirectional glass/epoxy composites with mixed-mode bending apparatus.* Composites science and technology, 1996. **56**(4): p. 439-449.

58. Shindo, Y., et al., *Delamination growth mechanisms in woven glass fiber reinforced polymer composites under mode II fatigue loading at*

cryogenic temperatures. Composites science and technology, 2009. **69**(11): p. 1904-1911.

59. Orifici, A.C., I. Herszberg, and R.S. Thomson, *Review of methodologies for composite material modelling incorporating failure.* Composite Structures, 2008. **86**(1-3): p. 194-210.

60. Cui, W., M. Wisnom, and M. Jones, *A comparison of failure criteria to predict delamination of unidirectional glass/epoxy specimens waisted through the thickness.* Composites, 1992. **23**(3): p. 158-166.

61. Camanho, P.P. and C.G. Dávila, *Mixed-mode decohesion finite elements for the simulation of delamination in composite materials.* 2002.

62. Reeder, J., *An evaluation of mixed-mode delamination failure criteria.* 1992.

63. Wimmer, G., C. Schuecker, and H. Pettermann, *Numerical simulation of delamination in laminated composite components–A combination of a strength criterion and fracture mechanics.* Composites Part B: Engineering, 2009. **40**(2): p. 158-165.

64. Dugdale, D.S., *Yielding of steel sheets containing slits.* Journal of the Mechanics and Physics of Solids, 1960. **8**(2): p. 100-104.

65. Barenblatt, G.I., *The mathematical theory of equilibrium cracks in brittle fracture.* Advances in applied mechanics, 1962. **7**: p. 55-129.

66. Needleman, A., *A continuum model for void nucleation by inclusion debonding.* Journal of applied mechanics, 1987. **54**(3): p. 525-531.

67. Tvergaard, V. and J.W. Hutchinson, *The relation between crack growth resistance and fracture process parameters in elastic-plastic solids.* Journal of the Mechanics and Physics of Solids, 1992. **40**(6): p. 1377-1397.

68. Cui, W. and M. Wisnom, *A combined stress-based and fracture-mechanics-based model for predicting delamination in composites.* Composites, 1993. **24**(6): p. 467-474.

69. Turon, A., et al., *A damage model for the simulation of delamination in advanced composites under variable-mode loading.* Mechanics of Materials, 2006. **38**(11): p. 1072-1089.

70. Chen, J.-F., E.V. Morozov, and K. Shankar, *Simulating progressive failure of composite laminates including in-ply and delamination damage effects.* Composites Part A: Applied Science and Manufacturing, 2014. **61**: p. 185-200.

71. Zhao, L., et al., *Simulation of delamination growth in multidirectional laminates under mode I and mixed mode I/II loadings using cohesive elements.* Composite Structures, 2014. **116**: p. 509-522.

72. Qiu, Y., M.A. Crisfield, and G. Alfano, *An interface element formulation for the simulation of delamination with buckling.* Engineering Fracture Mechanics, 2001. **68**(16): p. 1755-1776.

73. Alfano, G., *On the influence of the shape of the interface law on the application of cohesive-zone models.* Composites Science and Technology, 2006. **66**(6): p. 723-730.

74. Jiang, W.-G., et al., *A concise interface constitutive law for analysis of delamination and splitting in composite materials and its application to scaled notched tensile specimens.* International journal for numerical methods in engineering, 2007. **69**(9): p. 1982-1995.

75. Dávila, C.G., P.P. Camanho, and A. Turon, *Effective simulation of delamination in aeronautical structures using shells and cohesive elements.* Journal of Aircraft, 2008. **45**(2): p. 663-672.

76. Harper, P.W. and S.R. Hallett, *Cohesive zone length in numerical simulations of composite delamination.* Engineering Fracture Mechanics, 2008. **75**(16): p. 4774-4792.

77. Hamitouche, L., M. Tarfaoui, and A. Vautrin, *An interface debonding law subject to viscous regularization for avoiding instability: application to the delamination problems.* Engineering Fracture Mechanics, 2008. **75**(10): p. 3084-3100.

78. Borg, R., L. Nilsson, and K. Simonsson, *Simulating DCB, ENF and MMB experiments using shell elements and a cohesive zone model.* Composites Science and Technology, 2004. **64**(2): p. 269-278.

79. Borg, R., L. Nilsson, and K. Simonsson, *Modeling of delamination using a discretized cohesive zone and damage formulation.* Composites Science and Technology, 2002. **62**(10): p. 1299-1314.

80. Borg, R., L. Nilsson, and K. Simonsson, *Simulation of low velocity impact on fiber laminates using a cohesive zone based delamination model.* Composites Science and Technology, 2004. **64**(2): p. 279-288.

81. Alfano, G. and M. Crisfield, *Finite element interface models for the delamination analysis of laminated composites: mechanical and computational issues.* International journal for numerical methods in engineering, 2001. **50**(7): p. 1701-1736.

82. Zhao, L., et al., *Failure prediction of out-of-plane woven composite joints using cohesive element.* Composite Structures, 2013. **106**: p. 407-416.

83. Ranatunga, V. *Finite element modeling of delamination crack propagation in laminated composites*. in *Proceedings of the World Congress on Engineering 2011 Vol III WCE 2011*. 2011.

84. Wisnom, M.R. and F.-K. Chang, *Modelling of splitting and delamination in notched cross-ply laminates.* Composites Science and Technology, 2000. **60**(15): p. 2849-2856.

85. Zou, Z., et al., *Modelling interlaminar and intralaminar damage in filament-wound pipes under quasi-static indentation.* Journal of composite materials, 2002. **36**(4): p. 477-499.

86. Turon, A., et al., *An engineering solution for mesh size effects in the simulation of delamination using cohesive zone models.* Engineering fracture mechanics, 2007. **74**(10): p. 1665-1682.

87. Guo, C. and C. Sun, *Dynamic mode-I crack-propagation in a carbon/epoxy composite.* Composites Science and Technology, 1998. **58**(9): p. 1405-1410.

88. Wang, H. and T. Vu-Khanh, *Impact-Induced delamination in [05, 905, 05] carbon fiber/polyetheretherketone composite laminates.* Polymer Engineering & Science, 1991. **31**(18): p. 1301-1309.

89. Wang, H. and T. Vu-Khanh, *Fracture mechanics and mechanisms of impact-induced delamination in laminated composites.* Journal of composite materials, 1995. **29**(2): p. 156-178.

90. Sridharan, S., *Delamination behaviour of composites*. 2008: Elsevier.

91. Kumar, P. and N. Kishore, *Initiation and propagation toughness of delamination crack under an impact load.* Journal of the Mechanics and Physics of Solids, 1998. **46**(10): p. 1773-1787.

92. Perillo, G., N.P. Vedvik, and A.T. Echtermeyer. *Numerical analyses of low velocity impacts on composite. Advanced modelling techniques*. in *Proceedings of the Simulia customer conference–2012*. 2012.

93. Nezhad, H.Y., et al., *Numerical analysis of low-velocity rigid-body impact response of composite panels.* International Journal of Crashworthiness, 2014. **20**(1): p. 27-43.

94. Yang, Q. and B. Cox, *Cohesive models for damage evolution in laminated composites.* International Journal of Fracture, 2005. **133**(2): p. 107-137.

95. Caputo, F., A. De Luca, and R. Sepe, *Numerical study of the structural behaviour of impacted composite laminates subjected to compression load.* Composites Part B: Engineering, 2015. **79**: p. 456-465.

96. Caputo, F., et al., *Numerical study for the structural analysis of composite laminates subjected to low velocity impact.* Composites Part B: Engineering, 2014. **67**: p. 296-302.

97. Wang, W.Z., et al., *Damage and Failure of Laminated Carbon-Fiber-Reinforced Composite under Low-Velocity Impact.* Journal of Aerospace Engineering, 2014. **27**(2): p. 308-317.

98. Feng, D. and F. Aymerich, *Finite element modelling of damage induced by low-velocity impact on composite laminates.* Composite Structures, 2014. **108**: p. 161-171.

99. Shi, Y., C. Pinna, and C. Soutis, *Modelling impact damage in composite laminates: A simulation of intra- and inter-laminar cracking.* Composite Structures, 2014. **114**: p. 10-19.

100. Xin, S. and H. Wen, *A progressive damage model for fiber reinforced plastic composites subjected to impact loading.* International Journal of Impact Engineering, 2015. **75**: p. 40-52.

101. Choi, H.Y. and F.-K. Chang, *A model for predicting damage in graphite/epoxy laminated composites resulting from low-velocity point impact.* Journal of composite materials, 1992. **26**(14): p. 2134-2169.

102. Abrate, S., *Impact engineering of composite structures*. Vol. 526. 2011: Springer Science & Business Media.

103. Singh, H. and P. Mahajan, *Analytical modeling of low velocity large mass impact on composite plate including damage evolution.* Composite Structures, 2016. **149**: p. 79-92.

104. Batra, R., G. Gopinath, and J. Zheng, *Damage and failure in low energy impact of fiber-reinforced polymeric composite laminates.* Composite Structures, 2012. **94**(2): p. 540-547.